1987

Laser Spectroscopy of Transient Species in a Supersonic Free Jet Expansion.

Robert Sethfield Smith
Louisiana State University and Agricultural & Mechanical College

INFORMATION TO USERS

While the most advanced technology has been used to photograph and reproduce this manuscript, the quality of the reproduction is heavily dependent upon the quality of the material submitted. For example:

- Manuscript pages may have indistinct print. In such cases, the best available copy has been filmed.
- Manuscripts may not always be complete. In such cases, a note will indicate that it is not possible to obtain missing pages.
- Copyrighted material may have been removed from the manuscript. In such cases, a note will indicate the deletion.

Oversize materials (e.g., maps, drawings, and charts) are photographed by sectioning the original, beginning at the upper left-hand corner and continuing from left to right in equal sections with small overlaps. Each oversize page is also filmed as one exposure and is available, for an additional charge, as a standard 35mm slide or as a 17"x 23" black and white photographic print.

Most photographs reproduce acceptably on positive microfilm or microfiche but lack the clarity on xerographic copies made from the microfilm. For an additional charge, 35mm slides of 6"x 9" black and white photographic prints are available for any photographs or illustrations that cannot be reproduced satisfactorily by xerography.

Order Number 8728218

Laser spectroscopy of transient species in a supersonic free jet expansion

Smith, Robert Sethfield, Ph.D.

The Louisiana State University and Agricultural and Mechanical Col., 1987

U·M·I
300 N. Zeeb Rd.
Ann Arbor, MI 48106

Laser Spectroscopy of Transient Species in a Supersonic Free Jet Expansion

A Dissertation

Submitted to the Graduate Faculty of the
Louisiana State University and
Agricultural and Mechanical College
in partial fulfillment of the
requirements for the degree of
Doctor of Philosophy

in

Department of Physics and Astronomy

by

Robert Sethfield Smith

B.A., Francis Marion College, 1983

M.S., Louisiana State University, 1985

August, 1987

ACKNOWLEDGEMENTS

I wish to thank the Louisiana State University Alumni Association and the Department of Physics and Astronomy for providing financial support during the years of my graduate study. Their generosity has allowed me the time and freedom to complete this work. I am especially grateful to the members of the departmental machine shop, headed by Leo Jordan and including Allen Young and Ivan Shuff, and to Phillip Nurse for the machining skills they have patiently taught me and for the innumerable pieces of fuctional experimental equipment that they have molded, milled, and welded for me out of what were previously only large amounts of stock metal. Randy Gould of the departmental electronics shop has been indispensable for keeping our lab's electronic boxes alive and well, in spite of our seemingly constant efforts to damage them. The Physics and Astronomy Department office staff, particularly Karla Hathorne, Ophelia Dudley, Beverly Rodriguez, and Linda Frazier, have given me constant aid and guidance in my relations with the departmental word processor, as well as with the machinery of a large state university. In addition to their services, I thank all of these people for their warmth and friendship during my years of graduate study.

I am appreciative of the efforts of the faculty of the Department of Physics and Astronomy in instructing me in numerous courses. They have helped to maintain and deepen the curiosity and wonder which drew me to the study of physics in the first place.

The cooperation and encouragement of the members of our experimental atomic and molecular physics group has been invaluable. I appreciate the assistance of my fellow graduate students, Dal-woo Kim and Husney Naqvi, during our many trips to the Chemistry Department to obtain both wet and dry

ice as needed for my experiments. Our postdoc Michael Anselment has been a constant source of guidance and friendship. During our many conversations, his careful and searching methods of thought have helped me to avoid many hours of fruitless experimental work.

In addition, our collaboration with Trevor Sears of Brookhaven National Laboratory (BNL) has been invaluable to me. The mass spectrum reported in the work was obtained using the facilities in his laboratory. Further, his assistance in recording and analyzing rotational spectra for the furan cation was a great aid in completing this dissertation. Also, I would like to acknowledge the help of Mike White, also from BNL, who recorded the photoelectron spectrum for neutral furan that is reported in this work.

I wish to express special thanks to my advisor, Louis DiMauro, for providing ideas, advice, training, and friendship throughout my years at LSU. It is impossible to adequately describe in a few words what his assistance has meant to me. He personally instructed me in the experimental techniques necessary to run a laser laboratory. His open and accepting attitude has encouraged the discussion of any and all questions. His interest has extended beyond experiment to a true desire for friendship. And his expertise and physical intuition into the theoretical and experimental aspects of atomic and molecular physics have provided me with an understanding of many phenomena. He has been a true friend and advisor, and this thesis would not exist if it were not for his help.

Finally, I thank my wife Brenda and son Brian for their constant love and understanding. Their support and encouragement, along with that of my parents, brothers, sisters, and friends, have helped me to have the confidence, hope, and determination necessary to reach this point after all these years of study.

To My Wife Brenda

TABLE OF CONTENTS PAGE #

LIST OF TABLES PAGE #

LIST OF FIGURES PAGE #

Abstract of the Dissertation

The first experimental observation of laser induced fluorescence from the furan cation, $C_4H_4O^+$, is reported. The ion is formed in a supersonic free jet expansion via a two photon photoionization involving the 193 nm output of an ArF excimer laser. The $\tilde{B} \rightarrow \tilde{X}$ electronic transition is probed and vibrational assignments are presented for both states. Comparisons to the infrared, Raman, multiphoton ionization, and photoelectron spectrum of the parent molecule are made. The term value, T_{00}, for the $\tilde{B} \rightarrow \tilde{X}$ electronic transition is located at 24,675 cm^{-1}, which differs drastically from previously reported values from both experimental and theoretical investigations. These differences are discussed and probable explanations proposed. Our rotational analysis bears out the expectation that the furan cation is a near oblate top. Rotational constants and assignments are discussed. The lifetime of the vibrationless level of the $\tilde{B}$ state is measured to be 330 ns.

We also report the observation of C_2 Swan band emission ($d^3\pi_g \rightarrow a^3\pi_u$, 170 ns lifetime) in a supersonic free jet using a pulsed laser/vaporization source with a graphite target. In helium, Swan band emission is observed at distances of up to 15 nozzle diameters from the orifice and as long as 6 μs after the laser pulse, which immediately establishes the existence of some mechanism for the continuous localized formation of excited C_2 molecules at this point in the free jet. The emission data are reported as a function of laser intensity, backing pressure, downstream distance, and delay times. Evidence is presented supporting the continuous localized formation of excited C_2 molecules in the free jet via dissociative processes involving larger neutral and charged carbon clusters. The bearing of these results on the interpretation of cluster stability data is discussed.

1. INTRODUCTION

Laser spectroscopy is a powerful tool for investigating the structure of molecules and the dynamics of chemical processes. Molecular spectra of gas phase samples can provide a wealth of information, provided the spectra can be understood. However, this is not always possible. In all but the smallest molecules, a large number of vibrational and rotational quantum states are populated at room temperature by thermal collisions. Each of these states in turn contributes features to the observed spectrum, resulting in a complicated series of many individual lines. Often these molecular spectra become so congested that they cannot be resolved into their individual components and appear only as broad, structureless features. Even under favorable conditions where the spectral components are resolvable, there may be so many lines that the spectrum becomes exceedingly difficult, if not impossible, to interpret.

Recently, the use of supersonic free jets to prepare low temperature, gas phase samples has become an increasingly popular technique for eliminating such spectral congestion.[1-7] For some time, the dual objective of preparing an isolated gas phase sample which also has low internal temperatures, i.e., molecules residing in their lowest vibrational and rotational quantum states, has been desired by spectroscopists. However, the use of traditional methods has made these two goals mutually exclusive. Room temperature gas phase samples typically possess high internal temperatures, i.e., molecules having considerable population in their higher lying vibrational and rotational quantum states. Yet, if one lowers the internal temperature of a sample by cooling it with a proper refrigerant, one is limited on the low temperature side by the freezing point of the sample. If temperatures much below the

freezing point are desired, the reduced vapor pressure will require that the spectroscopy be done on a solid sample. While the spectroscopy of solids and the elucidation of the intermolecular interactions that occur in them is an interesting field in its own right, one is often interested in studying the intramolecular properties of an isolated molecule which is free from external perturbations. In such instances, standard cooling techniques cannot be used to achieve the extremely low internal temperatures desired by spectroscopists.

The use of a supersonic free jet expansion allows the preparation of isolated, gas phase molecules which have low internal temperatures as well. It thereby retains all the advantages of implanting a sample in a low temperature solid state matrix without the disadvantage of intermolecular perturbations. Such an expansion is achieved when one allows a gas at high pressure to expand through a small orifice or nozzle into a vacuum. The expansion cools the translational degrees of freedom of the gas mixture by narrowing the velocity distribution of the sample and hence reduces the relative collision energies of the molecules. In the postnozzle region of the expansion, this cold translational bath acts as a refrigerant for the other degrees of freedom of the molecule. The unique feature of a supersonic expansion that distinguishes it from an ordinary refrigerant is that the molecule of interest is only in contact with the cold bath for a finite amount of time. Therefore, the final state of the system is determined more by kinetics than thermodynamics. As the expansion proceeds, the density of the gas drops and eventually becomes too low to provide the collisions necessary to connect the internal degrees of freedom of the molecule with the translational bath. In the absence of such collisions, no energy can flow from the internal degrees of freedom, and the state that the system had when it entered the collision-free region is "frozen" from that point on.

Therefore, in the low density, collision-free portion of the supersonic expansion, the molecules of interest may be frozen in a very non-equilibrium state where extremely low internal temperatures do not necessarily preclude the simultaneous existence of an isolated, gas phase sample as well. Since condensation is a much slower process than rotational and vibrational relaxation, extensive internal cooling can be achieved before condensation takes place. Obviously, those degrees of freedom which equilibrate most rapidly with the translational bath will be the coldest at the point where the expansion runs out of collisions.[3]

In addition to providing isolated, internally cold, gas phase molecules, the supersonic free jet expansion provides an ideal environment in which to study a class of molecules commonly referred to as "chemical intermediates". This label applies to any molecular or atomic species that is produced during the detailed mechanism of an overall reaction but is not an isolable end product of that reaction. Generally, such intermediates are physically stable yet chemically unstable. That is, they are highly reactive, but the unperturbed species will not spontaneously decompose. Examples include reactive atoms such as H, O, and N; neutral free radicals such as CH, ClO, and C_5H_5 (cyclopentadienyl); charged molecular ions such as Cl_2^-, $C_6H_6^+$ (benzene cation), and $C_4H_4O^+$ (furan cation); and neutral and ionic clusters such as $C_4H_4O^+$-Ar, $C_6H_6^+$-He, and I_2-Ne.

Devising methods of detecting, characterizing, and monitoring the dynamics of these chemical intermediates is important for two general reasons. First, these chemical intermediates are simpler and much more reactive pieces of larger molecules. Their physical characterization can play a key role in the fundamental understanding of molecular bonding and reaction. Second, the capability to detect and monitor the transient

populations of these intermediates is important in the understanding of the detailed mechanisms, and hence the control, of many complicated chemical reactions of commercial and environmental importance.[1]

Neutral and ionic clusters are an interesting group of molecules in their own right and deserve further comment. Chemists are typically accustomed to studying molecules which are held together by chemical bonds with dissociation energies on the order of tens of thousands of wavenumbers. Since such bond energies are very much larger than the thermal collisional energies (kT) at room temperature, chemically bound molecules are usually stable with respect to binary collisions with inert partners. On the other hand, van der Waals forces are 10^2-10^3 times weaker than chemical forces, and at room temperature produce bonds with dissociation energies on the order of 100 cm^{-1} which is comparable to or weaker than kT. Therefore binary collisions with inert room temperature partners are likely to lead to the breaking of van der Waals bonds. Intermediate between these two extremes are the ionic clusters, which possess bonds with dissociation energies on the order of 1000 cm^{-1}. This increased bond strength is due to the fact that ionic clusters are not only held together by van der Waals forces but are subject to charge-induced dipole interactions as well. Therefore, they represent an interesting class of molecules since they possess bond strengths which are intermediate between those of a true chemical bond and those of a van der Waals bond.

The interest in this species of molecules is widespread. It arises in part from a desire to understand the van der Waals and ionic forces themselves and in part from the fact that knowledge of the structural and dynamic features of these molecules may shed some light on the analogous features in more complicated chemically bound molecules.[8] The study of such clusters is also important in the understanding of solvation effects. Observation of the

individual properties of clusters as they are formed in larger and larger sizes enables one to determine at what point a sample begins to take on the characteristics of a bulk solid or liquid. Additionally, the study of ionic clusters is helpful in understanding the chemical processes that occur in the atmosphere.

The study of molecules in a supersonic free jet expansion is a prolific field which has provided much valuable spectroscopic information. However, by far the large body of experimental work published to date has been performed on stable molecules. Therefore, the recent extension of this technique to the study of chemical intermediates represents the opening of a new realm of investigation to the experimental chemical physicist. Nonetheless, there are new problems associated with this advance as well. Due to the fact that chemical intermediates are highly reactive, they are not found naturally in the laboratory setting. In order to study such species, one must simultaneously create and isolate them in a collisionless environment where chemical reactions are not allowed to take place. In a supersonic free jet, one method of accomplishing this is by seeding a small concentration of a suitable precursor molecule into a large amount of an inert carrier gas, i.e., argon or helium, and allowing the mixture to undergo a supersonic expansion. As the mixture exits the nozzle orifice, the expansion is crossed with a tightly focussed beam from a photolysis laser. This laser either photofragments or photoionizes the precursor molecule to form the chemical intermediate of interest. This technique achieves both goals of creating and isolating the molecules simultaneously. However, it can also interfere with the cooling mechanism in the jet, since photofragmentation typically leaves the fragment molecules internally hot with substantial populations in their higher lying vibrational and rotational energy levels. Depending on where the

fragmentation takes place with respect to the nozzle, such heating limits the amount of internal cooling that can be achieved in a supersonic expansion. Additionally, since chemical intermediates must be formed in situ in the expansion, they are usually present in low concentrations, thereby accentuating the need for very sensitive detection systems.

In this thesis, three systems will be studied. First, a detailed spectroscopic investigation of the $\tilde{B} \rightarrow \tilde{X}$ transition in the furan cation, $C_4H_4O^+$, will be presented. This work represents the first laser induced fluoresence study of any state of the furan cation. Second, the ground state vibrational structure of the cyclopentadienyl radical, i.e., C_5H_5, will be discussed and compared to that of the furan cation. The cyclopentadienyl radical is isoelectronic with the furan cation and hence their stuctures will be correlated. Finally, the dynamics present in the early stages of a laser/vaporization supersonic jet cluster source will be investigated. Recently, such sources have been extensively used to study the clustering of neutral and ionic species.[9-12]

2. SUPERSONIC FREE JET EXPANSION THEORY

Since the early work of Kantrowitz and Grey[13], Kistiakowsky and Slichter[14], and Becker and Bier[15], supersonic expansions have been studied extensively with much attention paid to the details of the gas dynamics occurring within them. It is beyond the scope of this thesis to review the vast literature on this subject. Rather, the purpose of this section is to summarize the relevant properties of supersonic jets and to give some feeling for the operating conditions that have been used for laser spectroscopy. Several excellent reviews[1-3,8] have been written on this subject, and the following discussion is based in large part on material presented therein.

A supersonic expansion is formed when a high pressure gas initially contained in a reservoir is expanded through an orifice or nozzle into a vacuum or low pressure region. If the flow is collimated with apertures downstream of the nozzle, a supersonic molecular beam is produced. If no attempt is made to collimate the flow, one has a supersonic free jet.

By way of comparison to a supersonic expansion, a brief description of an effusive molecular beam[16] may prove useful. For such a source, the pressure in the gas reservoir is either low enough or the orifice small enough so that the mean free path, λ_0, of the gas molecules in the reservoir is much larger than the diameter, D, of the orifice. In this manner no collisions are allowed to take place as the molecules leave the orifice, and therefore no exchange of information can occur in the expansion process, i.e., no change in the properties of the gas as it leaves the reservoir. Consequently, an effusive source simply transfers molecules from a reservoir where they suffer collisions to a low pressure region where they do not, without affecting the properties of the gas.

Conversely, a supersonic expansion is essentially a device for converting random thermal energy into directed mass flow in the expanding jet. In a supersonic expansion, either the reservoir pressure or the orifice diameter is large enough so that $\lambda_0 < D$ thereby allowing collisions to occur both in and downstream from the orifice. This means that, unlike an effusive source where the flow is molecular, in a supersonic expansion the flow is hydrodynamic and can be described using thermodynamic principles. One can model such a flow by considering a small segment of gas that is large enough to contain enough molecules so that continuum thermodynamics can be applied, yet small enough so that the intensive thermodynamic variables are constant throughout the segment. The flow can then be described by calculating how the thermodynamic properties of the segment change as the gas expands and flows downstream.

In the absence of sources or sinks of entropy such as viscous forces, heat conductivity, shock waves, or chemical reaction, the expansion remains isentropic, i.e., reversible and adiabatic. From Maxwell's relations it is easy to see that

$$\frac{\partial T}{\partial V}_S = -\frac{\partial P}{\partial S}_V < 0 \qquad (1)$$

and that therefore the gas is cooled as it expands.

This cooling mechanism is physically resonable since as the expansion proceeds the flow velocity increases and the enthalpy associated with the directed flow must come from the random thermal enthalpy originally present in the static gas. Using the principle of conservation of enthalpy, it is possible to obtain a relationship between the downstream temperature and the flow velocity. If h is the enthalpy per unit mass at some point downstream from the nozzle, h_0 is the enthalpy per unit mass in the reservoir, and v is the flow velocity, then

$$h_0 = h + v^2/2 \qquad (2)$$

For an ideal gas

$$h_0-h = C_p(T_0-T) = [\gamma/(\gamma-1)r(T_0-T)] \qquad (3)$$

where $\gamma = C_p/C_v$, r = the gas constant per unit mass = (C_p-C_v), and C_p and C_v are the heat capacities per unit mass at constant pressure and constant volume, respectively. The quantity T is the downstream temperature and T_0 is the reservoir temperature. For an ideal gas the local speed of sound, a, is related to the local temperature, T, by

$$a = (\gamma rT)^{1/2} \qquad (4)$$

and therefore one can combine equations (2)-(4) to obtain

$$\frac{T}{T_0} = (1 + (\frac{\gamma-1}{2})M^2)^{-1} \qquad (5)$$

where M = Mach number $\equiv v/a$.

For an isentropic process in an ideal gas, the pressure is given by

$$P = K\rho^{\gamma} \qquad (6)$$

where K = constant and ρ is the density. This relationship in combination with the ideal gas law may be used to provide the relationships between pressure and density and the Mach number. These relationships are

$$\frac{P}{P_0} = (1 + (\frac{\gamma-1}{2})M^2)^{\frac{\gamma}{1-\gamma}} \qquad (7)$$

$$\frac{\rho}{\rho_0} = (1 + (\frac{\gamma-1}{2})M^2)^{\frac{1}{1-\gamma}} \qquad (8)$$

In order to calculate the temperature, pressure, or density as a function of position downstream from the nozzle it is necessary to know the Mach number as a function of position. The solution to this problem requires solving the hydrodynamic equations of flow and cannot be obtained from thermodynamics. Ashekas and Sherman[16] have shown that for a continuous gas and for distances greater than a few nozzle diameters from the orifice, the Mach number is given by

$$M = A(X/D)^{\gamma-1} \qquad (9)$$

where X is the distance downstream from the nozzle, D is the nozzle diameter and A is a constant that depends on γ and is 3.26 for a monatomic gas. Using the above relations, Lubman, Rettner, and Zare[17] have calculated the two-body collision rate in a free jet expansion to be

$$z_{jet} = (2)^{1/2} n\sigma\bar{v}_0 \left[1 + \left(\frac{\gamma-1}{2}\right)M^2 \right]^{-1/2} \qquad (10)$$

where n = molecular density, σ = collisional cross section, , and $\bar{v}_0$ = mean velocity in the reservoir. For a given orifice size, one can calculate the number of collisions that a molecule has suffered at various positions downstream from the orifice by integrating the product of the time of travel, based on the flow velocity of the carrier gas involved, with the collision rate over the range of distances that one is interested in.

An example of the use of these relationships is presented in Figure 1. The top half of the figure is a schematic diagram of a free jet expansion illustrating how random thermal motion is converted into directed mass flow. Shown below the expansion is a scale measuring distance downstream (X) in units of the nozzle diameter (D). Given at various positions downstream are the Mach number, the temperature, the density (in torr at standard temperature and pressure (S.T.P.), 1 S.T.P. torr = 3.54×10^{16} molecules per cubic centimeter), the pressure (in millitorr), and the number of two-body collisions between X/D = 5 and the indicated point. Although it is not possible to draw completely distinct boundaries, it is reasonable to assume that most of the n-body ($n \geq 3$) collisions occur below X/D = 5 for typical expansion conditions, whereas the region beyond X/D = 5 is dominated by two-body collisions. Since three-body (and higher) collisions are difficult to model theoretically, this example will be concerned only with the region beyond X/D = 5, where two-body collisions predominate, since these can be

modelled accurately. For the present calculation, a typical stagnation pressure behind the nozzle of 10 atmospheres (7600 torr) of helium at 300K is considered. Further, a nozzle diameter of D = 0.150 mm and a collision cross section of 50 square angstroms are assumed. The latter quantity is a typical cross-section for a ring-structured molecule, such as furan or benzene. The mean velocity of the molecules in the reservoir is calculated to be approximately 1.3×10^5 cm/sec for a static gas of helium at 300K, and the terminal flow velocity of helium in a supersonic expansion is taken from reference 1 as 2×10^5 cm/sec. Note that most of the collisions occur by 30 nozzle diameters in a supersonic free jet expansion. Whereas 120 collisions take place in the region from 0 to 30 nozzle diameters, only 7 occur in the region from 30 to 60 nozzle diameters. Hence, most of the cooling collisions take place early in the expansion, and by 30-50 nozzle diameters the "cold" molecules find themselves in an essentially collision-free environment where they can be studied in the gas phase.

From the above discussion, it is obvious that the supersonic free jet expansion is an ideal environment in which to prepare isolated, internally cold molecular samples. However, simply obtaining low temperatures is not the object of a supersonic free jet expansion. To be useful, these temperatures must be produced in the gas phase with little or no condensation. This is possible in a supersonic expansion because the molecule of interest is in contact with the cold bath for only a short time. As the expansion proceeds downstream, the translational temperature decreases but the molecular density decreases as well. For the example in Figure 1, the number density drops by a factor of 500 within the first 10 nozzle diameters, and then drops by a comparably small factor of less than 40 in the next 50 nozzle diameters. Hence, the majority of collisions have occurred by 30-40 nozzle diameters.

FIGURE 1. SUPERSONIC FREE JET EXPANSION

(Taken from reference 1)

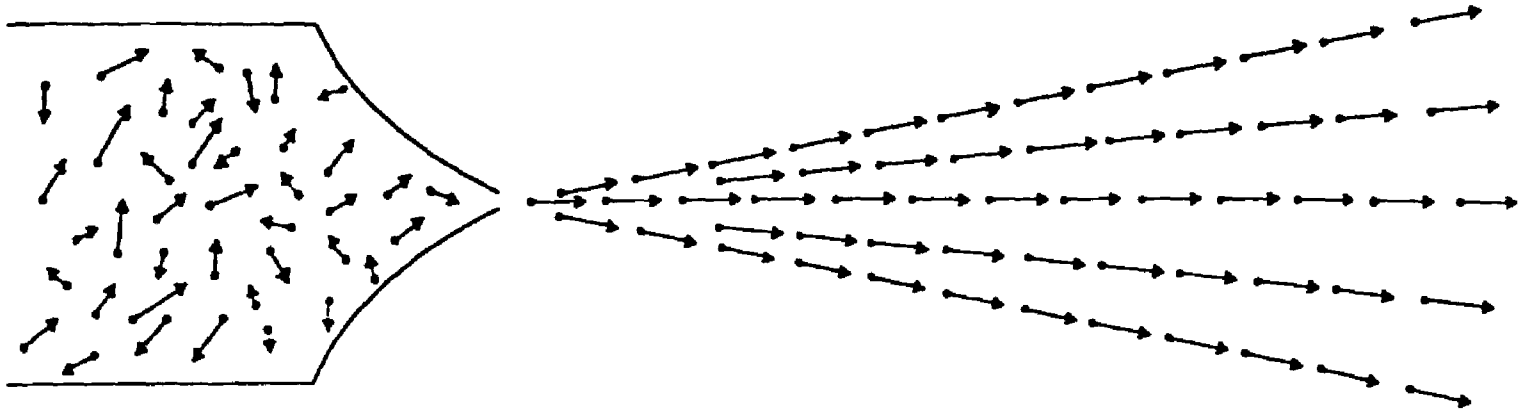

Distance (X/D)	10	20	30	40	50	60
Mach number	15	24	32	38	44	50
Temperature (K)	4.0	1.6	0.9	0.6	0.5	0.4
Density (S.T.P. torr)	15	3.7	1.6	0.9	0.6	0.4
Pressure (mtorr)	150	15	3.5	1.5	0.7	0.4
Collisions (5 → X)	80	106	112	115	117	119

Whereas cooling requires only two-body collisions, condensation requires three-body (or higher) collisions to form nuclei around which condensation can take place. Therefore it must occur primarily in the region below X/D = 5, which is dominated by such collisions. After that point, two-body collisions predominate and condensation essentially cannot take place. A common method for limiting molecular condensation is the use of a seeded mixed-gas expansion. If a small quantity of the molecule of interest is mixed with a large amount of a carrier gas, such as argon or helium, and the mixture is expanded to form a supersonic free jet, most of the collisions will be between inert gas atoms. Since the interatomic forces are much weaker between inert gas atoms than they are between reactive molecules, condensation is greatly reduced.

At first glance, one might think it a little surprising that such jets are referred to as "supersonic" expansions. After all, the limiting jet flow velocity is only slightly greater than the average velocity of the molecules in the static gas. However, the local speed of sound is proportional to the square root of the translational temperature. Thus, as the expansion proceeds and the translational temperature decreases, the Mach number (M), which is the ratio of the flow velocity to the local speed of sound, increases dramatically. For the portion of the expansion shown in Figure 1, M has already reached a value of 50 by 60 nozzle diameters. However, it would be incorrect to assume that any arbitrarily large Mach number or arbitrarily low temperature can be reached at some point sufficiently far downstream from the nozzle. This is not the case because at some point the gas density becomes low enough so that there are no binary collisions. In such a situation, the individual gas molecules can no longer exchange information and the temperature of the expanding gas cannot change. The molecule's internal

degrees of freedom are essentially "frozen" from that point on. This causes M to reach a limiting value known as the terminal Mach number, M_T. Anderson and Fenn[18] have predicted that the terminal Mach number should be a function of the product (P_0D), where P_0 is the backing pressure in the reservoir and D is the nozzle diameter, and they have deduced an expression

$$M_T = \varepsilon(D/\Lambda_0)^{(\gamma-1/\gamma)} \qquad (11)$$

where Λ_0 is the mean free path in the reservoir, γ is the heat capacity ratio, and ε is a constant characteristic of the particular gas in question. For argon, the experimental value of ε has led to

$$M_T = 133(P_0D)^{0.4} \qquad (12)$$

At a stagnation pressure of 10 atmospheres and a nozzle diameter of 0.150 mm, one obtains a terminal Mach number of 62.3 for argon.

The most significant exception to equation (11) is the case of helium at high Mach numbers. Miller et al.[19] have shown that because of quantum effects, the collisional cross section increases rapidly with decreasing energy of the gas. Therefore, at low temperatures, helium continues to collide at distances far beyond what would have been the low density limit for a classical gas. This allows one to obtain far higher terminal Mach numbers and far lower translational temperatures than would be predicted by equation (11). Mach numbers of up to 250 corresponding to a temperature of 0.015K (assuming a reservoir temperature of 300K) have been achieved in helium expansions[20], and Mach numbers of up to 770 corresponding to a temperature of 0.0015K have been predicted theoretically.[21] Even in comparison to today's sophisticated low temperature technology, a supersonic free jet expansion is not a bad refrigerant.

In a supersonic expansion two changes take place. First of all, the center of the velocity distribution shifts to a non-zero flow velocity, and

secondly the distribution narrows because of the translational cooling. These effects are illustrated in Figure 2 for a Mach 10 supersonic expansion, as compared to a static gas velocity distribution at 300K. From a spectroscopist's point of view, the most important physical property is not the most probable velocity but the width of the velocity distribution, since this determines the relative energies of collisions in the expanding gas. The gas may be moving with a high flow velocity, but if all the molecules are moving at about the same velocity, collisions between them will be of low energy.

If only the translational motion of a gas were cooled, a supersonic expansion would be of little use to a spectroscopist interested in cooling the internal molecular motions. Since the distribution of molecular velocities is narrow, the energies of the collisions that occur in the expansion wil be characteristic of these low temperatures. As a result of these collisions, the internal degrees of freedom of the molecules, i.e., the vibrational and rotational energy levels, will relax toward these same low temperatures. In effect, the vibrating and rotating molecule finds itself in a translationally cold bath and the internal degrees of freedom are cooled by collisions just as if they had been immersed in liquid helium.

As the expansion proceeds, the density of the gas and the probability of collisions decrease. Thus the ultimate distribution of internal excitation in the molecule may not reach precise equilibrium with the translational temperature of the molecule. As a rough rule, rotational-translational equilibrium is usually rapid, and rotational temperatures are rarely greatly different from translational ones in a simple expansion. However, vibrational-translational equilibrium is usually less efficient and often depends of the details of the vibrational structure. Nonetheless, substantial

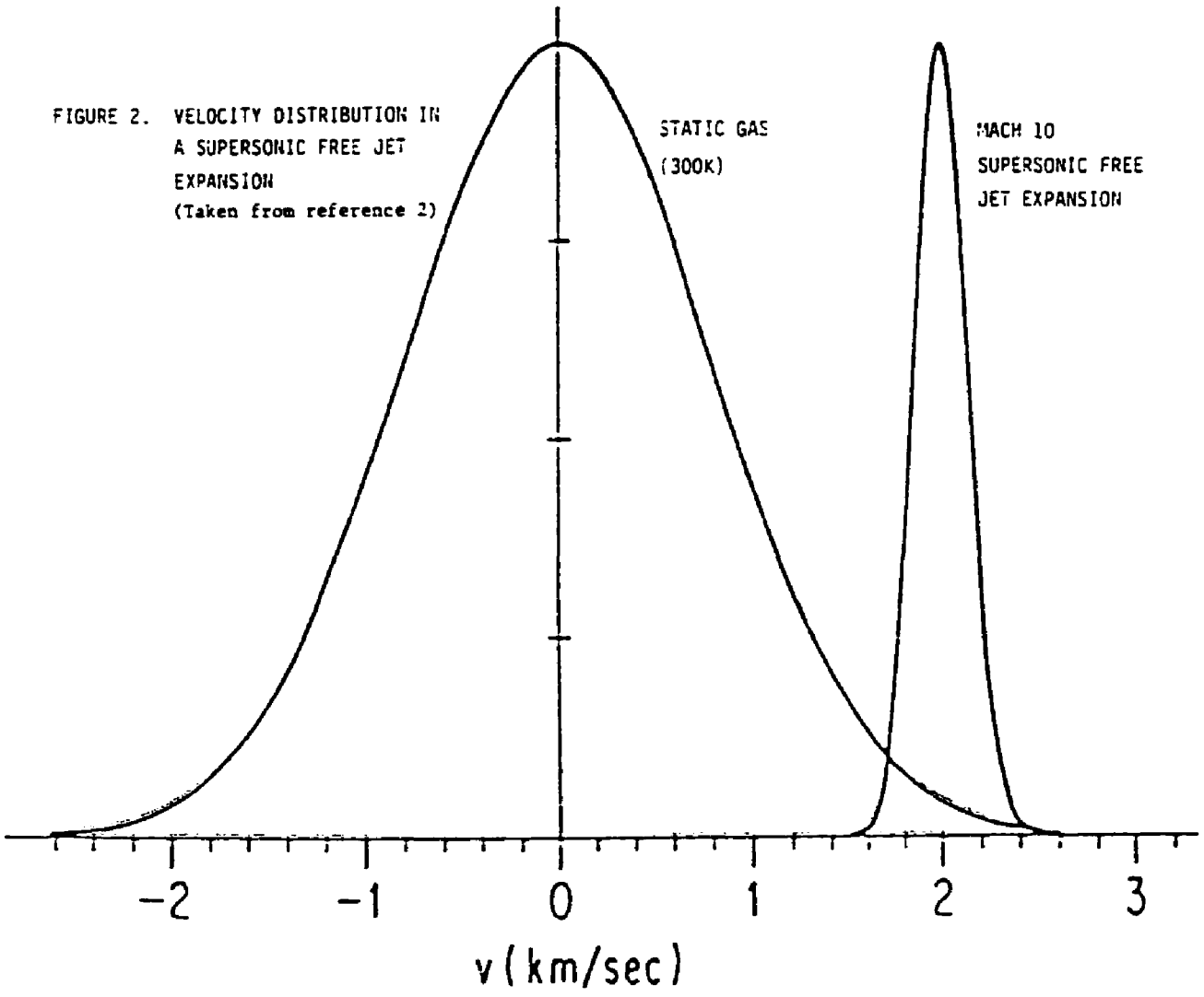

FIGURE 2. VELOCITY DISTRIBUTION IN A SUPERSONIC FREE JET EXPANSION (Taken from reference 2)

vibrational cooling is also typically observed.

An example of rotational and vibrational cooling in a supersonic free jet expansion is presented in Figure 3. A spectrum of the hexafluorobenzene cation ($C_6F_6^+$) produced by Penning ionization in a flow system which was maintained at room temperature is shown in Figure 3a. Notice the high level of spectral congestion which is present. The complexity of lines and unresolved structures makes this spectrum extrememly difficult, if not impossible, to interpret. Figure 3b illustrates a second Penning ionization spectrum of $C_6F_6^+$ in which the flow system was cooled by liquid N_2. The spectrum is somewhat simplified, but many features are still broad and unresolved. A final spectrum of $C_6F_6^+$ is presented in Figure 3c, in which the cations were produced by two-photon photoionization of the parent molecule (C_6F_6) via an ArF excimer laser. The C_6F_6 was dilutely seeded into an inert carrier gas in the supersonic free jet. The improved clarity is tremendous. What was once a congested, uninterpretable spectrum is now a distinct series of well-resolved lines that are much more easily assigned. The reduction, or absence, of hot band structures also aids in the interpretation of the spectrum.

In principle, any type of spectroscopy that has been used to study static gases may be used to study samples cooled in a supersonic expansion, but in practice the spectroscopic method must be tailored to the properties of the free jet. Supersonic jet spectroscopy is intimately connected with laser technology. If lasers were not available, such spectroscopy would be at best a curiosity which could be demonstrated in a few favorable cases but which lacked general utility. Due to the low density and short path length involved, the use of such jets entails a loss of sensitivity. In part this is offset by the fact that only a few quantum states are populated in the cold

FIGURE 3. LASER EXCITATION SPECTRA OF THE HEXAFLUOROBENZENE CATION
(Taken from reference 1)

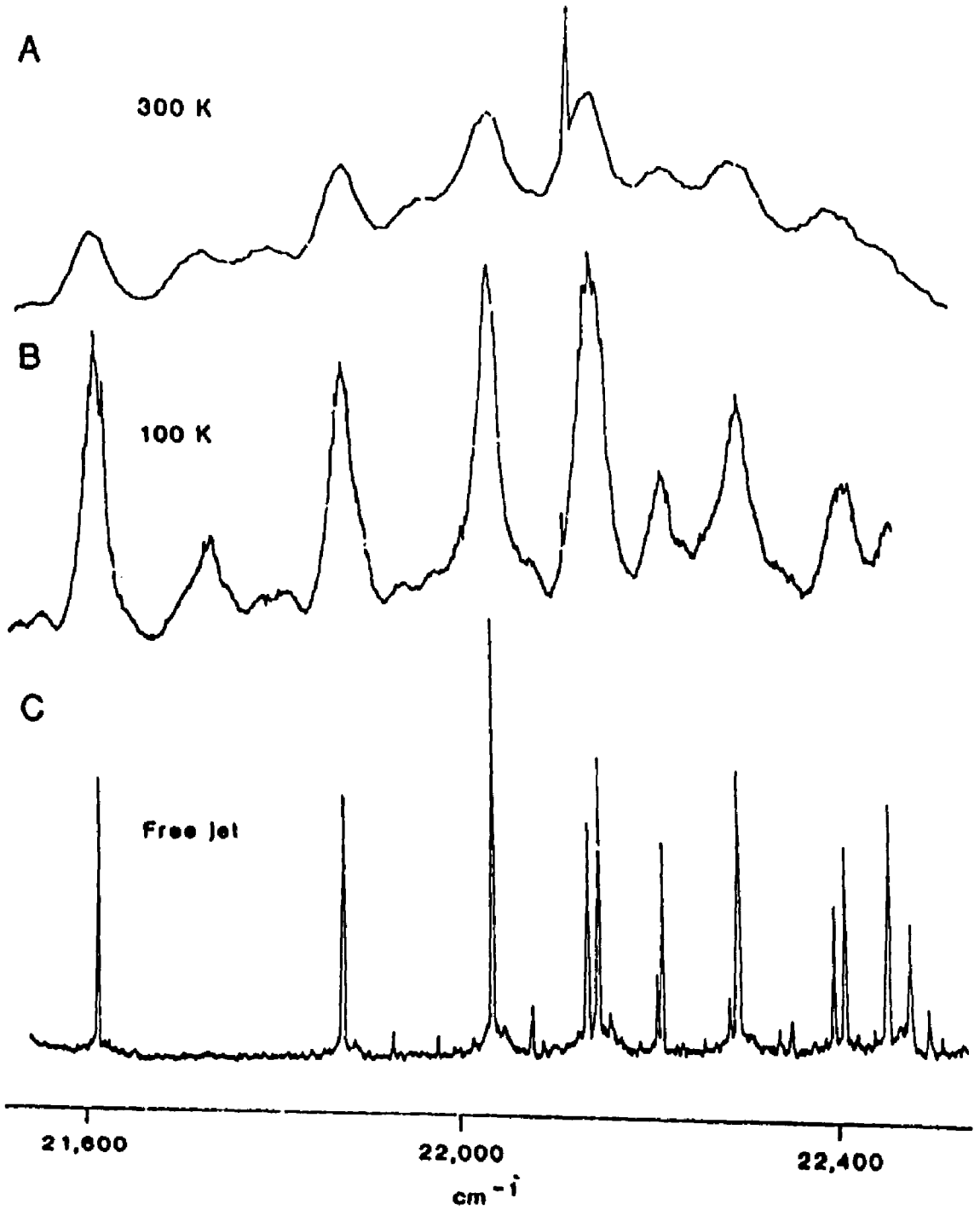

jet, and therefore the intensity that was distributed among a large number of spectral lines in the static gas is compressed into a few lines in the jet. However, even with this advantage the small number of molecules requires that a large number of photons be used if the experiment is to be successful for any but the most favorable cases.

The advantage of lasers is not just that they are powerful. The property of greatest importance is the brightness, the power per unit frequency per unit solid angle. Because it is possible to design lasers with very narrow frequency bandwidths, all of the laser photons can be used to pump a given spectral line. Moreover, the small divergence and cross-sectional area of a laser beam means that all the power can be delivered to the small volume occupied by the cold molecular jet.

Supersonic free jet expansions are now widely used by physical chemists and laser physicists, and as lasers become more reliable and easier to use, they should become increasingly attractive to scientists in other disciplines as well. The availability of reliable high-power pulsed lasers has already extended the useful spectral region into the ultraviolet and near infrared, and has made available various nonlinear spectroscopic techniques, such as multiphoton ionization. These advances will make the use of supersonic jets attractive in a growing number of areas.

3. MOLECULAR THEORY

The theoretical treatment of molecular systems is a rich and plentiful field. Many authors have writen volumes of texts in efforts to explain molecular structure and dynamics. It is far beyond the scope, or intention, of this thesis to attempt a complete description of this subject. Rather, this section is intended to be a summary of those aspects of molecular theory which are relevant to the molecular systems discussed in this work. Although there are many sources of information on molecular theory, the following material is primarily based on the introductory text of Guillory[22] and the detailed, three volume series of Herzberg[23-25].

In a first approximation, the energy of a molecule can be represented as a sum of three parts: the electronic, the vibrational, and the rotational energies

$$E = E_e + E_v + E_r$$

To give a general overview of the energy level structure of a molecule, the vibrational and rotational levels of two electronic states A and B are represented schematically in Figure 4. Energy level spacings are typically on the order of tens of thousands of cm^{-1} for electronic levels, a few hundred to a few thousand cm^{-1} for vibrational levels, and 10^{-3} to a few cm^{-1} for rotational levels.

3.1. DIATOMIC MOLECULES

Although the majority of this thesis is concerned with polyatomic systems, the final section on optical emission studies of graphite in a

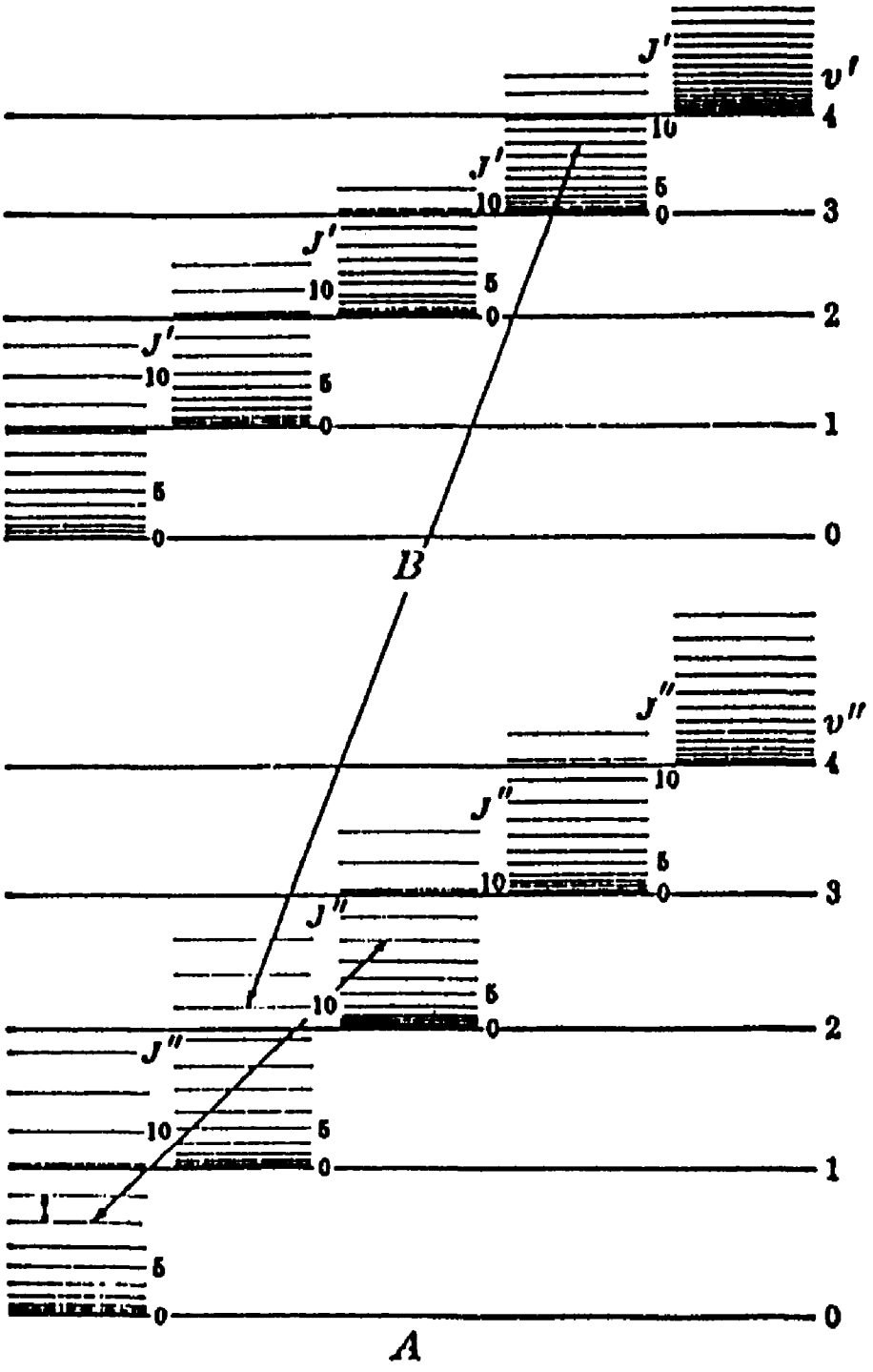

FIGURE 4. VIBRATIONAL AND ROTATIONAL ENERGY LEVELS OF TWO ELECTRONIC STATES, A AND B, OF A MOLECULE
(Taken from reference 23)

laser/vaporization cluster source involves a discussion of the well-known Swan band system in C_2. Therefore, a brief description of diatomic molecules is warranted. However, since this study was dynamical in nature, no detailed investigation into the rotational and vibrational structure of this band was undertaken, and hence an introductory explanation of the electronic state labelling in diatomic systems is all that is required to acquaint the reader with the notation that appears in that section.

In atomic systems the electronic term states are classified according to the value of the electronic orbital angular momentum, $\tilde{L}$. (Vectors will henceforth be denoted by the presence of the ~ symbol above them.) In diatomic molecules, the electronic cloud no longer has spherical symmetry, as in the atomic case, but rather has axial symmetry about the internuclear axis of the molecule. As a result, $\tilde{L}$ is no longer a constant of the motion but can take on certain quantized projections, relative to the internal electric field along the internuclear axis, from +L, L-1,..., -L+1, -L. The component of $\tilde{L}$ along the axis, which is a constant of the motion, is called $\tilde{\Lambda}$, and its magnitude is $\Lambda \frac{h}{2\pi}$. The vector diagram illustrating the coupling of L about the internuclear axis is shown in Figure 5. As far as the molecule is concerned, the coupling of L in the positive or negative direction producing $+\Lambda$ or $-\Lambda$ has the same energy. Thus each electronic state is doubly degenerate. There are symbols for the molecular electronic states similar to the atomic term symbols. States having

$$\Lambda = 0, 1, 2, 3, 4, \ldots.$$

are labelled, respectively,

$$\Sigma, \Pi, \Delta, \Phi, \Gamma, \ldots.$$

As in the atomic case, the individual electron spins add vectorially to produce integral or half-integral spin quantum numbers, $\tilde{S}$, depending on

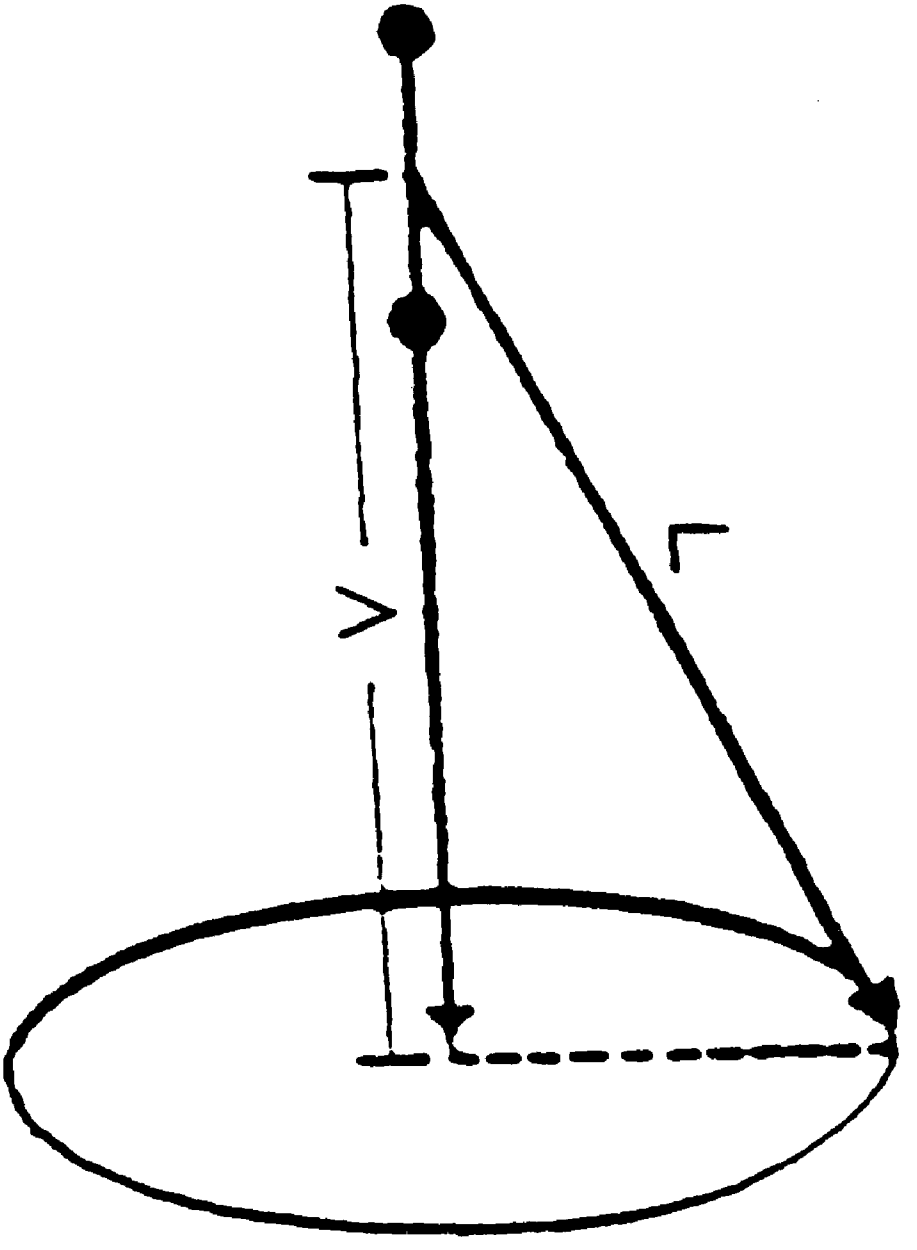

FIGURE 5. COUPLING OF ORBITAL ANGULAR MOMENTUM, L, ABOUT THE INTERNUCLEAR AXIS IN A DIATOMIC MOLECULE
(Taken from reference 23)

whether there is an even or an odd number of electrons. The spin of a given state is indicated by adding the multiplicity 2S+1 to the upper left-hand side of the term symbol. Further, if the two nuclei in the molecule are identical, as is the case for C_2, the field in which the electrons move has a center of symmetry. Consequently, the electronic eigenfunctions remain either unchanged or only change sign when reflected at the center, i.e., when the coordinates of the electrons x_i, y_i, z_i are replaced by their negatives $-x_i$, $-y_i$, $-z_i$. In the first case, the state to which the eigenfunction belongs is called an "even" state and in the second case an "odd" state. The symmetry property even or odd is indicated by adding a subscript g or u, respectively, to the term symbol. One further state label, which applies to the lowest multiplicity polyatomic molecules as well, indicates the ordering of the electronic levels. Beginning with the ground state and moving upward in energy, the electronic levels are labelled:

$\tilde{X}$, $\tilde{A}$, $\tilde{B}$, $\tilde{C}$, $\tilde{D}$,..., respectively, for spin singlets and doublets

and $\tilde{a}$, $\tilde{b}$, $\tilde{c}$, $\tilde{d}$,..., respectively, for spin triplets and quartets.

For the Swan band system in C_2, the electronic transition is given as

$$\tilde{d}\ ^3\Pi_g \rightarrow \tilde{a}\ ^3\Pi_u$$

The emission comes from the third excited triplet electronic state of C_2, which is a spin triplet (S=1) with Λ=1 and even symmetry with respect to inversion, and terminates in the lowest triplet state of C_2, which is also a spin triplet with Λ=1 but has odd symmetry with respect to inversion.

3.2. POLYATOMIC MOLECULES

Since structural analyses have been conducted on the polyatomic systems investigated in this work, a more detailed treatment of polyatomic systems is necessary. Electronic, vibrational, and rotational state labelling and allowed transitions in all pertinent cases are discussed.

3.2.1 ELECTRONIC SPECTROSCOPY

3.2.1.1 ELECTRONIC ENERGY

As in diatomic molecules, the nuclei in polyatomic molecules are held together by the electrons. The total energy of the molecule, neglecting spin and magnetic interactions, is the sum of the potential and kinetic energies of the electrons and the potential and kinetic energies of the nuclei.

The fact that the total energy of the molecule is a constant is represented by the Schrodinger equation

$$H\psi = E\psi \qquad (13)$$

where ψ is the wavefunction, $H=T+V$ is the Hamiltonian operator, V is the potential operator, and T is the kinetic energy, which is given by

$$T = \frac{1}{2m} \sum_i p_i^2 + \frac{1}{2} \sum_k \frac{1}{M_k} p_k^2 \qquad (14)$$

where the first term in (14) is the kinetic energy of the electrons and the second that of the nuclei. If the linear momenta are replaced by their corresponding operators, one obtains the Schrodinger equation in the more conventional form

$$\frac{1}{m}\sum_i\left(\frac{\partial^2\psi}{\partial x_i^2}+\frac{\partial^2\psi}{\partial y_i^2}+\frac{\partial^2\psi}{\partial z_i^2}\right)+\sum_k\frac{1}{M_k}\left(\frac{\partial^2\psi}{\partial x_k^2}+\frac{\partial^2\psi}{\partial y_k^2}+\frac{\partial^2\psi}{\partial z_k^2}\right)+\frac{8\pi^2}{h^2}(E-V)\psi=0 \qquad (15)$$

where x_i, y_i, z_i are the coordinates of the electrons and x_k, y_k, z_k are the coordinates of the nuclei.

The potential energy V can be separated into an electronic and a nuclear contribution

$$V = V_e + V_n \qquad (16)$$

where V_e includes the mutual potential energy of the electrons as well as the potential energy of the electrons with respect to the nuclei and V_n is the mutual potential energy of the nuclei. As a first approximation, if one neglects the interaction between the electronic and nuclear degrees of freedom of the molecule, a solution of equation (15) can be written as

$$\psi = \psi_e(\ldots, x_i, y_i, z_i, \ldots)\ \psi_{vr}(\ldots, x_k, y_k, z_k, \ldots) \qquad (17)$$

where ψ_e represents the motion of the electrons and ψ_{vr} represents the vibrations and rotations associated with the nuclei. Such a product wavefunction allows the Schrodinger equation to be separated into the following equations, of which ψ_e and ψ_{vr} are the solutions,

$$\sum_i\left(\frac{\partial^2\psi_e}{\partial x_i^2}+\frac{\partial^2\psi_e}{\partial y_i^2}+\frac{\partial^2\psi_e}{\partial z_i^2}\right)+\frac{8\pi^2 m}{h^2}(E^{el}-V_e)\psi_e=0 \qquad (18)$$

$$\sum_k\frac{1}{M_k}\left(\frac{\partial^2\psi_{vr}}{\partial x_k^2}+\frac{\partial^2\psi_{vr}}{\partial y_k^2}+\frac{\partial^2\psi_{vr}}{\partial z_k^2}\right)+\frac{8\pi^2}{h^2}(E-E^{el}-V_n)\psi_{vr}=0 \qquad (19)$$

respectively. It can be seen that (17) is only an approximate solution of (15) by substituting it into (15) and taking account of equations (18) and (19). One finds that (15) is satisfied only if

$$\sum_k\frac{2}{M_k}\left[\frac{\partial\psi_e}{\partial x_k}\frac{\partial\psi_{vr}}{\partial x_k}+\frac{\partial\psi_e}{\partial y_k}\frac{\partial\psi_{vr}}{\partial y_k}+\frac{\partial\psi_e}{\partial z_k}\frac{\partial\psi_{vr}}{\partial z_k}+\psi_{vr}\left(\frac{\partial^2\psi_e}{\partial x_k^2}+\frac{\partial^2\psi_e}{\partial y_k^2}+\frac{\partial^2\psi_e}{\partial z_k^2}\right)\right] \qquad (20)$$

can be neglected. That is, one must assume that the variation of ψ_e with the nuclear coordinates is sufficiently slow so that its first and second derivatives with respect to the nuclear coordinates can be neglected. This is physically reasonable since the mass of the electrons is much smaller than that of the nuclei. Therefore, they move much more rapidly and the nuclei appear to remain fixed in space during the time it takes them to change position. That this condition is usually fulfilled to a satisfactory approximation has been shown in detail by Born and Oppenheimer.[26]

The equation (18) for ψ_e is the Schrödinger equation for the electrons moving in the field of the fixed nuclei and having a potential energy V_e. For different nuclear positions, V_e is different, and therefore the eigenfunctions ψ_e and eigenvalues E^{el} of this equation depend on the nuclear coordinates as parameters.

The second equation (19) is the Schrödinger equation for the nuclei moving under the action of the potential $E^{el}+V_n$. Thus in this approximation the motion can be separated into an electronic motion in a more or less fixed nuclear frame characterized by a function ψ_e and a nuclear motion, i.e., vibration and rotation, in a potential field $E^{el}+V_n$, characterized by a function ψ_{vr}.

The minimum value of $E^{el}+V_n$, that is, the minimum of the potential surface of a given stable electronic state, is considered as the electronic energy of this state and is designated E_e. The total energy of the molecule may then be written in the above approximation as $E = E_e + E_{vr}$, where $E_{vr} = E - E^{el} - V_n$ is the vibrational-rotational energy derived from equation (19).

3.2.1.2 CLASSIFICATION OF ELECTRONIC STATES

In the Schrödinger equation for the electronic motion (18), V_e is the potential energy of the electrons in the field of the fixed nuclei. As before, the equilibrium positions of the nuclei are used in discussing the electronic motion. Therefore, V_e has the symmetry of the molecule in that particular configuration. If a symmetry operation is carried out, the Schrödinger equation for the electronic motion is unchanged. As a consequence, the electronic eigenfunction for the non-degenerate states can only be symmetric or antisymmetric, i.e., can only remain unchanged or merely change sign, for each of the symmetry operations permitted by the symmetry of the molecule in its equilibrium position. For degenerate states, the eigenfunction can only change into a linear combination of two or more degerate eigenfunctions such that the square of the eigenfunction, which represents the electron density, remains unchanged.

As a result of these properties, molecular species may be systematically classified according to the number and types of symmetry elements and operations they possess. The nuclear framework (like any geometrical figure) may have one or more of the following symmetry elements:

(1) a plane of symmetry usually designated by σ ;

(2) a center of symmetry usually designated by i;

(3) a p-fold axis of symmetry usually designated by C_p, where p = 1, 2,...;

(4) a p-fold rotation-reflection axis usually designated by S_p; a molecule having such an element of symmetry will be transformed into itself by a rotation through an angle $360^\circ/p$ followed by a reflection at a plane perpendicular to the axis;

(5) the identity element designated by I or E.

In general a molecule has several of these symmetry elements. By combining more and more symmetry elements, systems of higher and higher symmetry are obtained. However not all combinations of symmetry elements are possible, rather only certain ones are allowed. A complete set of nonredundant symmetry operations possessing all the properties of a mathematical group, i.e., closure, associativity, identity element, and inverses, is called a point group. A molecule in a given configuration must belong to one of the various point groups. The following two point groups are of importance to the study of the structure of the furan cation and the cyclopentadienyl radical, respectively:

(1) The point group C_{2v} has a two-fold rotational axis of symmetry C_2 and two vertical planes of symmetry σ_v through that axis.

(2) The point group D_{5h} has a five-fold rotational axis C_5, five vertical planes of symmetry σ_v through that axis, and a horizontal plane of symmetry σ_h perpendicular to C_5.

The ground state geometrical structures of the furan cation and the cyclopentadienyl radical are presented in Figure 6 for comparison.

The individual molecular eigenfunctions may behave differently with respect to the various symmetry operations of a given point group. However, since in general not all symmetry elements of a point group are independent of one another, only certain combinations of behavior of the eigenfunctions with regard to the symmetry operations are possible. Such combinations of symmetry properties are called "symmetry types" or "species". In group-theoretical language, they are the "irreducible representations" of the point group considered. Each electronic eigenfunction, and therefore each electronic state, belongs to one of the possible species of the point group of the

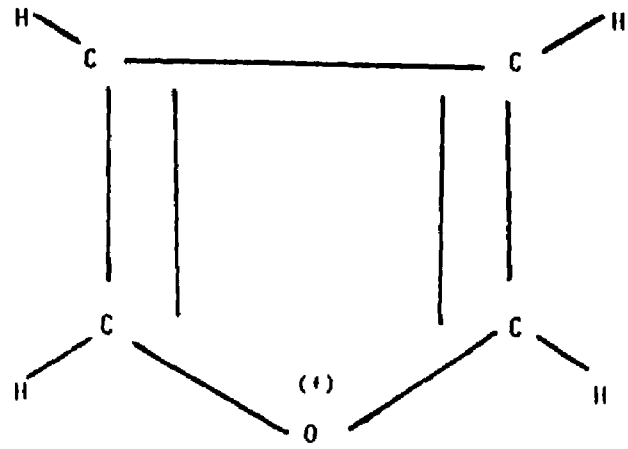

FURAN CATION

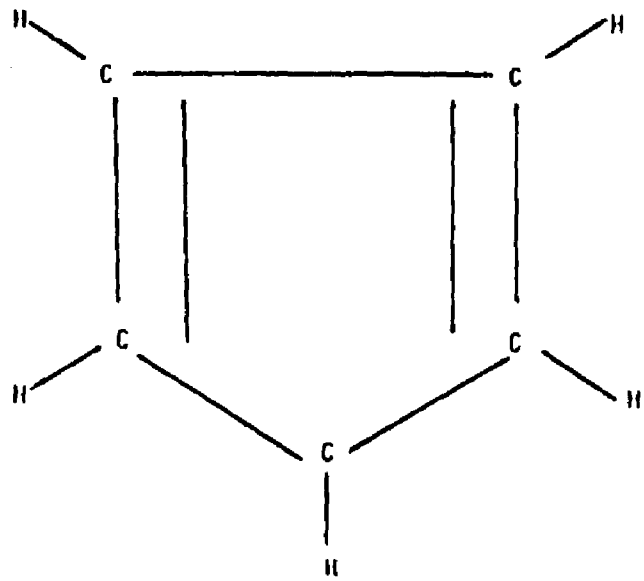

CYCLOPENTADIENYL RADICAL

FIGURE 6. GROUND STATE GEOMETRIES OF THE FURAN CATION AND THE CYCLOPENTADIENYL RADICAL

molecule in the equilibrium position.

Information concerning the manner in which the various molecular eigenfunctions are affected by the symmetry operations of the point group is presented in what is called a "character table". Such a table is presented in Table 1 for the C_{2v} point group, where +1 and -1 are the characters themselves and represent symmetric and antisymmetric behavior, respectively. For C_{2v} symmetry, the A designation is used for irreducible representations that are symmetric with respect to rotations about the principle C_2 axis, and B for those that are antisymmetric. The subscripts, 1 or 2, designate which representations are symmetric or antisymmetric, respectively, with respect to reflections through the x-z molecular plane.

The third column of the character table indicates how the rotational, translational, and general coordinates transform under the group operations. For example, for translation in the z direction, performing all four symmetry operations, i.e., E, $C_2(z)$, $\sigma(xz)$, and $\sigma(yz)$, will leave the z vector unchanged. In a like manner, translations and rotations about all three molecular axes can be classifed according to the species to which they belong.

Up to now, the effects of electron spin have been ignored in the classification of electronic states. The electronic eigenfunction ψ_e has been considered to be a function of the positional coordinates of the electrons only, and the symmetry types refer to the symmetry properties of these orbital wavefunctions. The full electronic eigenfunctions must take account of the fact that each electron has a spin s=1/2 which can orient itself parallel or antiparallel to any preferred direction. As long as the coupling of the individual spins with the orbital motion is small, the spins of the individual electrons form a resultant $\tilde{S}$ which is half-integral for an odd number of electrons and integral for an even number. The resultant spin $\tilde{S}$ is

C_{2v}	I	$C_2(z)$	$\sigma_v(xz)$	$\sigma_v(yz)$	Translations and Rotations
A_1	1	1	1	1	T_z
A_2	1	1	−1	−1	R_z
B_1	1	−1	1	−1	T_x and R_y
B_2	1	−1	−1	1	T_y and R_x

TABLE 1

C_{2v} CHARACTER TABLE
(Taken from reference 25)

characteric of each electronic state. Any of the species of a given point group may occur with any of the S values compatible with the number of electrons present. As for atoms and diatomic molecules, the coupling of the spin $\tilde{S}$ with the orbital motion may lead to a splitting of the molecular electronic state into 2S+1 components. This multiplicity is written as a superscript in front of the symbol representing the symmetry type. Thus for S=0 we have $^1A_1$, $^1B_2$, ... states, for S=1/2 we have $^2A_1$, $^2B_2$, ... states, for S=1 we have $^3A_1$, $^3B_2$, ... states, and so on.

3.2.1.3 SELECTION RULES FOR ELECTRONIC TRANSITIONS

An electronic transition is allowed if it can occur as an electric dipole transition according to the selection rules discussed below, without taking account of the interaction of vibration and rotation with the electronic motion. In other words, the electronic transition is allowed if it can occur for fixed nuclei.

Let ψ_e' and ψ_e'' be the electronic eigenfunctions of the upper and lower states, respectively, of an electronic transition of interest and let both states be non-degenerate. The transition will be allowed if and only if the matrix element

$$R_{e'e''} = \int \psi_e'^{*} \tilde{M} \psi_e'' \, d\tau_e \qquad (20)$$

is different from zero. Here $\tilde{M}$ is the electric dipole moment vector whose components are $\Sigma e_i x_i$, $\Sigma e_i y_i$, and $\Sigma e_i z_i$, where the e_i are the charges on the particles with coordinates x_i, y_i, z_i, and the integral $R_{e'e''}$ is to be taken over the whole configuration space of the 3N coordinates of the N-atom molecule. Therefore, an electronic transition between non-degenerate states

is allowed if the product

$$\psi_e'^{*}\,\tilde{M}\,\psi_e'' \qquad (21)$$

is totally symmetric for at least one orientation of $\tilde{M}$ or, in other words, if the product $\psi_e'\psi_e''$ belongs to the same species as one of the components of $\tilde{M}$. "Product" in this context refers to the direct product of group theory.

For example, consider an electronic transition from an A_2 state to a B_2 state in a molecule belonging to the C_{2v} point group. To determine whether this is an allowed electronic transition, one must determine the symmetry of the direct product of A_2 and B_2. From the tables of Appendix III of reference 24, where many direct products of this nature are listed, the product is found to be B_1. Upon consultation of the character table in Table 1, it is found that the x-component of the dipole moment has B_1 symmetry as well. Therefore, the transition is allowed.

Another selection rule concerns electron spin. The electronic eigenfunction including spin can be written as a product of an orbital and a spin function

$$\psi_{es} = \psi_e\psi_s \qquad (22)$$

Therefore the transition moment including spin is

$$\int \psi_{es}'^{*}\,\tilde{M}_e\,\psi_{es}''\,d\tau_e ds = \int \psi_e'^{*}\,\tilde{M}_e\,\psi_e''d\tau_e \int \psi_s'^{*}\,\psi_s''ds \qquad (23)$$

The second integral at the right vanishes for states of different spin since the spin functions corresponding to different S values are orthogonal to one another. Therefore, we have the selection rule

$$\Delta S = 0 \qquad (24)$$

that is, only states of the same multiplicity can combine with each other. In other words, intercombinations are forbidden.

3.2.2 VIBRATIONAL SPECTROSCOPY

3.2.2.1 VIBRATIONAL DEGREES OF FREEDOM

In describing the motion of the nuclei in a polyatomic molecule, one might choose the Cartesian coordinates x_k, y_k, z_k of each nucleus k referred to a fixed coordinate system. Hence, for N nuclei, one would need 3N coordinates to describe their motion, i.e., there are 3N degrees of freedom. However, in describing the vibrational motion of the system, it is not necessary to know information about the translational motion of the system as a whole, which is described completely by the three coordinates of the center of mass. Therefore 3N-3 coordinates are sufficient to fix the relative positions of all N nuclei with respect to the center of mass. Additionally, the motion relative to the center of mass includes a rotation of the system. That rotation may be described by three angular coordinates which specify the orientation of the system. Thus 3N-6 coordinates are left for describing the relative motion of the nuclei. In other words, there are 3N-6 vibrational degrees of freedom. For linear molecules, two angular coordinates are sufficient to fix the orientation and hence they have 3N-5 vibrational degrees of freedom. In the case of the furan cation, which is nonlinear and has nine atoms, the above considerations predict the existence of twenty-one normal modes of vibration.

3.2.2.2 VIBRATIONAL ENERGY LEVELS

The Schrödinger equation for a system of N particles with coordinates x_i, y_i, z_i and masses m_i is

$$\sum_i \frac{1}{m_i}\left(\frac{\partial^2\psi}{\partial x_i^2} + \frac{\partial^2\psi}{\partial y_i^2} + \frac{\partial^2\psi}{\partial z_i^2}\right) + \frac{8\pi^2}{h^2}(E-V) = 0 \qquad (25)$$

The simplest possible assumption about the form of the vibrations in a polyatomic molecule is that each atom moves toward and away from its neighbors in simple harmonic motion. By substituting the harmonic oscillator potential for V in (25) and transforming the equation to the normal coordinates (ξ_i) of the molecule, one obtains

$$\sum_i \frac{\partial^2\psi}{\partial\xi_i^2} + \frac{8\pi^2}{h^2}\left[E - \frac{1}{2}\sum \lambda_i\xi_i^2\right]\psi = 0 \qquad i = 1, \ldots, 3N \qquad (26)$$

By means of the substitution

$$\psi = \psi_1(\xi_1)\ \psi_2(\xi_2) \cdots \psi_{3N}(\xi_{3N}) \qquad (27)$$

it is possible to separate the variables in equation (26) and resolve it into 3N equations of the form

$$\frac{1}{\psi_i}\frac{\partial^2\psi_i}{\partial\xi_i^2} + \frac{8\pi^2}{h^2}\left(E_i - \frac{1}{2}\lambda_i\xi_i^2\right) = 0 \qquad (28)$$

The eigenvalues of equation (28) are given by

$$E_i = h\nu_i\left(v_i + \frac{1}{2}\right) \qquad v_i = 0, 1, 2, \ldots \qquad (29)$$

or, if transformed to wavenumber units, where they are known as a "term values",

$$G(\nu_1, \ldots, \nu_{3N}) = \frac{E(\nu_1, \ldots, \nu_{3N})}{hc} = \sum_i w_i(v_i + \frac{1}{2}) \quad i = 1, \ldots, 3N \qquad (30)$$

where the w_i are the vibrational frequencies in cm^{-1} units. In the above equations, the non-genuine vibrations, i.e., translations and rotations, have been included. However, since $\nu = 0$ for them, they do not contribute to the vibrational energy, so that the relevant parts of the summations are only over the 3N-6 or 3N-5 genuine normal vibrations. Since the simple harmonic potential is only a first approximation to the true molecular potential, the actual energy levels of the molecule may differ somewhat from those predicted by equation (30). The magnitude of those differences provide a measure of the degree of anharmonicity of the molecular potential and are described by the following equation

$$G(\nu_i, \ldots, 3N\text{-}6 \text{ or } 3N\text{-}5) = \sum_i w_i(v_i + \frac{d_i}{2}) + \sum_i \sum_{k \geq i} x_{ik}(v_i + \frac{d_i}{2})(v_k + \frac{d_k}{2}) +$$

$$+ \sum_i \sum_{k \geq i} g_{ik} l_i l_k \qquad (31)$$

where v_i and v_k are the vibrational quantum numbers, w_i are the vibrational frequencies, x_{ik} and g_{ik} are the anharmonicity constants, d_i and d_k are the degeneracies of the vibrations, and l_i and l_k are the angular momentum quantum numbers of the degenerate vibrations. For non-degenerate vibrations, $d_i = d_k = 1$ and $l_i = l_k = g_{ik} = 0$.

If vibrational term values in the upper and lower states of a particular transition are $G'(v_1', v_2', \ldots)$ and $G''(v_1'', v_2'', \ldots)$, respectively, and if the electronic term values are T_e' and T_e'', the wavenumbers of all possible vibrational transitions for a given electronic transition, i.e., band system, are represented by

$$\nu = \nu_e + G'(\nu'_1, \nu'_2, \ldots) - G''(\nu''_1, \nu''_2 \ldots) \qquad (32)$$

where $\nu_e = T'_e - T''_e$ is a constant for a given band system, called the "origin" of the band system and T'_e and T''_e represent the electronic state energies without including the zero point vibrational energy. For practical purposes it is often much more convenient to refer energies to the lowest vibrational level in each state. Therefore, one can measure a quantity ν_{00} which is the wavenumber of the 0-0 band, that is, the transition between the two lowest vibrational levels of the two electronic states. Although ν_{00} is somewhat different from ν_e, it is also commonly referred to as the "origin" or "vibrationless transition" of the band system.

3.2.2.3 SYMMETRY OF NORMAL VIBRATIONS

If a symmetry operation is carried out on a molecule and transforms that molecule into a configuration which is indistinguishable from the original one, the potential energy will be the same as before the operation. Therefore, the frequencies of the normal vibrations will be the same for the transformed as for the non-transformed system. However, in the vibrating molecule the transformed displacements are not necessarily the same as the non-transformed ones. For a non-degenerate vibration these displacement coordinates can only be symmetric or antisymmetric with respect to any given symmetry operation that is permitted by the point group of the molecule. For degenerate vibrations, they may additionally change into linear combinations of two or more of the coordinates associated with the degenerate vibrations. A detailed discussion of this topic can be found on page 82 of reference 24.

As a consequence of these behaviors, normal vibrations can be classified

according to the species of the point group of the molecule in the same manner as the electronic energy levels were. Therefore, for C_{2v} symmetry in particular, normal vibrations are labelled as having A_1, A_2, B_1, and B_2 symmetry.

In a given electronic state, a polyatomic molecule may be excited to any of its possible vibrational levels. Each of these levels may be called a vibrational-electronic state or, for short, a "vibronic" state. In a first approximation, the vibronic eigenfunction which describes the electronic and vibrational motions of the molecule can be written as a product $\psi_{ev} = \psi_e\psi_v$ of the electronic eigenfunction ψ_e and the vibrational eigenfunction ψ_v. Both ψ_e and ψ_v have symmetry properties in accordance with one of the species of the point group. Therefore, the vibronic eigenfunction must also belong to one of these species. The vibronic species is therefore simply obtained by taking a direct product of the species of the electronic and vibrational eigenfunctions. The results for most cases of interest can be found in Appendix III of reference 25.

If a non-degenerate vibration ν_i is symmetric with respect to a certain symmetry element, it follows that its contribution ψ_i to the vibrational eigenfunction is symmetric with respect to that symmetry operation for all values of v_i, where v_i is the vibrational quantum number. If a normal vibration ν_k is antisymmetric with respect to a symmetry element, it follows that ψ_k is antisymmetric for odd v_k but is symmetric for even v_k.

The total vibrational eigenfunction ψ can be approximated as a product of harmonic oscillator eigenfunctions ψ_1, ψ_2, ..., corresponding to the 3N-6 or 3N-5 normal coordinates. Therefore, if there are only non-degenerate vibrations, the total eigenfunction will be symmetric with respect to a given symmetry operation if there is an even number of component functions ψ_k that

are antisymmetric with respect to that same symmetry operation. Likewise, the total eigenfunction will be antisymmetric if there is an odd number of antisymmetric component functions. Its behavior with respect to a given symmetry operation is independent of the number of symmetric component functions. In other words, for an antisymmetric vibration v_k, ψ_k is antisymmetric for odd v_k, and the total vibrational eigenfunction is symmetric with respect to a certain symmetry operation if the sum $\Sigma\, v_k$, extended over all normal vibrations that are antisymmetric with respect to that symmetry operation, is even; and the total vibrational eigenfunction is antisymmetric with respect to the symmetry operation if that sum is odd.

3.2.2.4 SELECTION RULES FOR VIBRATIONAL TRANSITIONS

The selection rule of equation (20) applies strictly only for fixed nuclei. Actually the nuclei are not fixed and therefore we must consider the total eigenfunction which includes the nuclear coordinates as well. Neglecting rotational motion and the interaction of electronic and vibrational motion, the total eigenfuction can be written as

$$\psi_{ev} = \psi_e \psi_v \qquad (33)$$

where ψ_{ev} is the vibronic eigenfunction, ψ_e the electronic eigenfunction, and ψ_v the vibrational eigenfunction. If the electric dipole moment is divided into two parts

$$\tilde{M} = \tilde{M}_e + \tilde{M}_n \qquad (34)$$

where $\tilde{M}_e$ is the part due to the electrons and $\tilde{M}_n$ the part due to the nuclei, the transition moment is given by

$$R_{e'v'e''v''} = \int \psi'^{*}_{ev}\tilde{M}\psi''_{ev}d\tau_{ev}$$

$$= \int \psi'^{*}_{v}\psi''_{v}d\tau_{v} \int \psi'^{*}_{e}\tilde{M}_{e}\psi''_{e}d\tau_{e} + \int \psi'^{*}_{v}\tilde{M}_{n}\psi''_{v}d\tau_{v} \int \psi'^{*}_{e}\psi''_{e}d\tau_{e} \qquad (35)$$

However,

$$\int \psi'^{*}_{e}\psi''_{e}d\tau_{e} = 0 \qquad (36)$$

since the electronic eigenfunctions belonging to different electronic states are mutually orthogonal. Therefore, if one denotes

$$R_{e'e''} = \int \psi'^{*}_{e}\tilde{M}_{e}\psi''_{e}d\tau_{e} \qquad (37)$$

equation (35) becomes

$$R_{e'v'e''v''} = R_{e'e''} \int \psi'^{*}_{v}\psi''_{v}d\tau_{v} \qquad (38)$$

so that the transition probability can be resolved into a factor depending on the nuclear motion alone and a factor depending on the electronic motion alone.

In an allowed electronic transition, the transition moment $R_{e'e''}$ is different from zero. Whether or not a transition from a certain vibrational level in the upper state (v_i') to a certain vibrational level of the lower state (v_i'') occurs depends of the vibrational overlap integral in equation (38). In a symmetrical molecule, in order that this integral be different from zero, the product $\psi'^{*}_{v}\psi''_{v}$ must be totally symmetric with respect to all symmetry operations of the point group to which the molecule belongs. This conclusion is equivalent to the selection rule: only vibrational levels of the same species in the upper state as in the lower state can combine with each other. This is the general vibrational selection rule in allowed transitions.

For a symmetric vibration, all excited vibrational levels are symmetric and therefore transitions are allowed for

$$\Delta v_k = 0, \pm 1, \pm 2, \ldots . \qquad (39)$$

However, the strength of any given transition will be governed by the size of the vibrational overlap integral in equation (38). This conclusion is essentially a statement of the Frank-Condon principle.

For an antisymmetric vibration, i.e., a vibration that is antisymmetric with respect to at least one element of symmetry, higher vibrational levels will be symmetric for even v_k and antisymmetric for odd v_k. Therefore according to the general selection rule, v_k can only change by an even number

$$\Delta v_k = 0, \pm 2, \pm 4, \ldots . \qquad (40)$$

Therefore, if there is a transition between one totally symmetric vibration and one antisymmetric vibration, all transitions with

$$\Delta v_k = \pm 1, \pm 3, \pm 5, \ldots$$

will be missing.

If several antisymmetric vibrations are present, transitions with $\Delta v_k = \pm 1, \pm 3, \ldots$ may appear as long as for each symmetry element

$$\sum_a \Delta v_a = 0, \pm 2, \pm 4, \ldots . \qquad (41)$$

where v_a is the vibrational quantum number of a vibration that is antisymmetric with respect to that particular symmetry element for which the above sum is formed. This is because only then will the vibrational species be the same in both the upper and lower states.

3.2.2.5 FERMI RESONANCE INTERACTION

In a polyatomic molecule, it may happen that two vibrational levels belonging to different vibrations may have nearly the same energy, that is, may be accidentally degenerate. As was first recognized by Fermi[27], such a

resonance leads to a perturbation of the energy levels. The two vibrational levels repel one another and do not follow a formula of the type in equation (29). The strength of the repulsion is larger the nearer the degeneracy. At the same time, a mixing of the eigenfunctions of the two states also occurs. The matrix element of the perturbation W is given by

$$W_{ni} = \int \psi_n^* W \psi_i d\tau \qquad (42)$$

The perturbation W is essentially given by the anharmonic terms in the potential energy, while ψ_n and ψ_i are the zero approximation eigenfunctions of the two levels that perturb each other. Since W has the full symmetry of the molecule and is therefore totally symmetric, the two eigenfuctions must have the same symmetry type in order to give a nonzero value to W_{ni}. Hence, a Fermi resonance can only occur between vibrational levels of the same species.

3.2.2.6 JAHN-TELLER INTERACTION

The energy levels of excited, degenerate vibrations in a degenerate electronic state possess several sublevels, and these may be separated energetically via a vibronic interaction. For example, in a D_{3h} molecule in an E" electronic state, if the degenerate vibration $\nu_2(e')$ is singly excited, the following species arise: $A_1' + E'$. If vibronic interaction is taken into account, there will be as many component levels as there are vibronic species for each vibrational level. In order to evaluate the magnitude of the vibronic splittings one must consider the splitting of the potential function for non-totally symmetric displacements of the nuclei. According to Jahn and Teller[28], there is always at least one non-totally symmetric normal coordinate in a non-linear molecule for which the splitting of the potential function is

such that instead of two coinciding minima there are two separate minima at nonzero values of the particular coordinate. This situation is illustrated in Figure 7 where the potential function V is plotted along the non-totally symmetric normal coordinate Q. The splitting of the potential surface in a degenerate electronic state is called the "static Jahn-Teller effect". The actual splitting of the vibrational levels caused by this effect is called the "dynamic Jahn-Teller effect". In order to obtain these vibronic energy levels it is necessary to solve the Schrodinger equation for a potential function of the type illustrated in Figure 7. The result is that there are as many component levels as there are vibronic species in the excited vibrational state.

3.2.3 ROTATIONAL SPECTROSCOPY

In discussing the various types of nonlinear polyatomic molecules, it is convenient to separate them into three different classes according to the degree of symmetry they possess. More specifically, this can be done on the basis of the equivalency of the principle moments of inertia.

(1) Symmetric Top Molecules: $I_a < I_b = I_c$ Prolate

$I_a = I_b < I_c$ Oblate

(2) Spherical Top Molecules: $I_a = I_b = I_c$

(3) Asymmetric Top Molecules: $I_a \neq I_b \neq I_c$

A species having all three principal moments equal is defined as a spherical top, and any molecule having an n-fold axis, where, $n \geq 3$, with any two equivalent principal moments is defined as a symmetric top. A symmetric top molecule that has a "football-shaped" electronic charge distribution about the

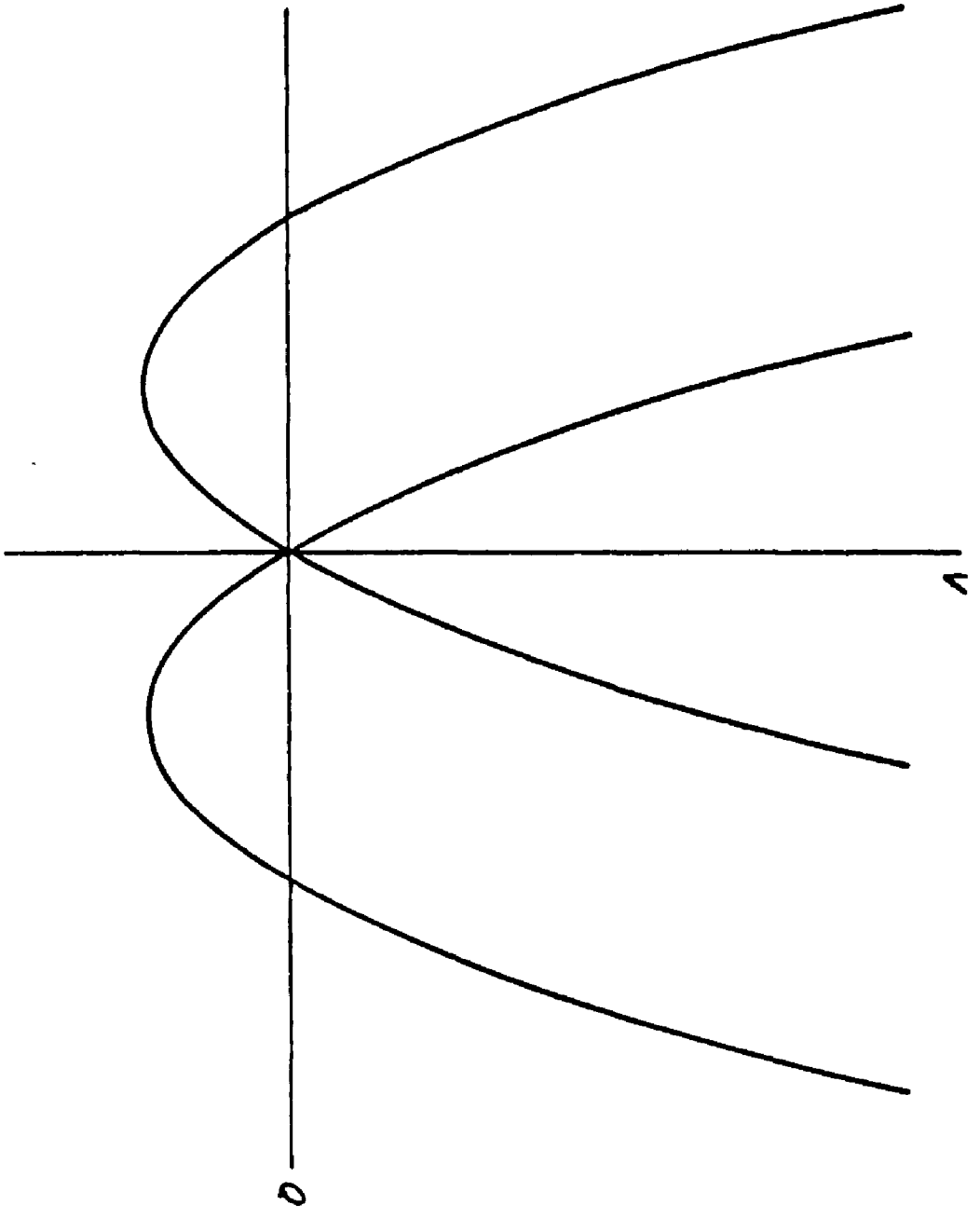

FIGURE 7. CROSS SECTION THROUGH THE POTENTIAL FUNCTION OF A NON-LINEAR MOLECULE IN A DEGENERATE ELECTRONIC STATE WHEN VIBRONIC INTERACTION IS LARGE

(taken from reference 25)

unique minor axis (I_a) is called a prolate top, and one having a "pancake-shaped" electronic charge distribution about the unique major axis (I_c) is called an oblate top. Those species having different inertial moments about all three main axes are defined as asymmetric tops. The general convention used in this case is $I_a < I_b < I_c$.

The ground state geometry of the furan cation, and hence the furan molecule as well, is illustrated in Figure 6. Although structure will be discussed in more detail in Section 5.5, it is obvious that furan is a near symmetric top molecule. Therefore a brief description of this type of rotator is warranted in this section.

3.2.3.1 SYMMETRIC TOP MOLECULES

The classical expression for the kinetic energy of a polyatomic rigid rotor is

$$E_k = \frac{p_a^2}{2I_a} + \frac{p_b^2}{2I_b} + \frac{p_c^2}{2I_c} \qquad (43)$$

For an oblate top, $I_a = I_b$ and I_c is the unique and major symmetry axis. The quantum mechanical expectation value of this operator yields the following term value, for an oblate symmetric top

$$F_e(J,K) = B_e J(J+1) + (C_e - B_e)K^2 \qquad (44)$$

$$\text{where } C_e = \frac{h}{8\pi^2 c I_c} \text{ and } B_e = \frac{h}{8\pi^2 c I_b}$$

J is the quantum number of the total angular momentum $\tilde{J}$, while K is the quantum number of the component of $\tilde{J}$ in the direction of the top axis. The corresponding vector diagram is shown in Figure 8. This is essentially the

same as for the case of a diatomic molecule. The only difference is that here $\tilde{J}_z$ is produced by the motion of heavy nuclei about the figure axis and is called $\tilde{K}$, while in diatomic molecules it is produced by the motion of electrons about the internuclear axis and is called $\tilde{\Lambda}$. $\tilde{N}$ is the total angular momentum apart from spin.

If corrections to the rigid rotor model are considered, one obtains a term value given by

$$F_v(J,K) = B_vJ(J+1) + (C_v-B_v)K^2 - D_JJ^2(J+1)^2 - D_{JK}J(J+1)K^2 - D_KK^4 \qquad (45)$$

where the last three terms are centrifugal stretching terms which account for the non-rigid nature of molecular systems. These are always small compared to the first two except at very high J and K values. Their variation with the vibrational quantum number v_i can almost always be neglected. However, the dependence of the rotational constants A_v and B_v on v_i is important. It is given by

$$C_v = C_e - \sum_i \alpha_i^C(v_i + \tfrac{1}{2}d_i) + \ldots$$

$$B_v = B_e - \sum_i \alpha_i^B(v_i + \tfrac{1}{2}d_i) + \ldots \qquad (46)$$

where C_e and B_e are the equilibrium rotational constants defined earlier, α_i^C and α_i^B are correction terms which are small compared to C_e and B_e, and d_i is the degeneracy of the vibrational level. The summation is over all normal vibrations of the molecule. (Note: The results obtained for an oblate symmetric top can be transformed into those of a prolate symmetric top by substituting A for C in equation (45).)

If the rotational term values in the upper and lower vibronic states are $F_v'(J',K')$ and $F_v''(J'',K'')$, respectively, and if the vibrational term values are $G'(v_1', v_2', \ldots)$ and $G''(v_1'', v_2'', \ldots)$ and the electronic term values

FIGURE 8. ANGULAR MOMENTUM VECTOR DIAGRAM FOR A SYMMETRIC TOP MOLECULE *

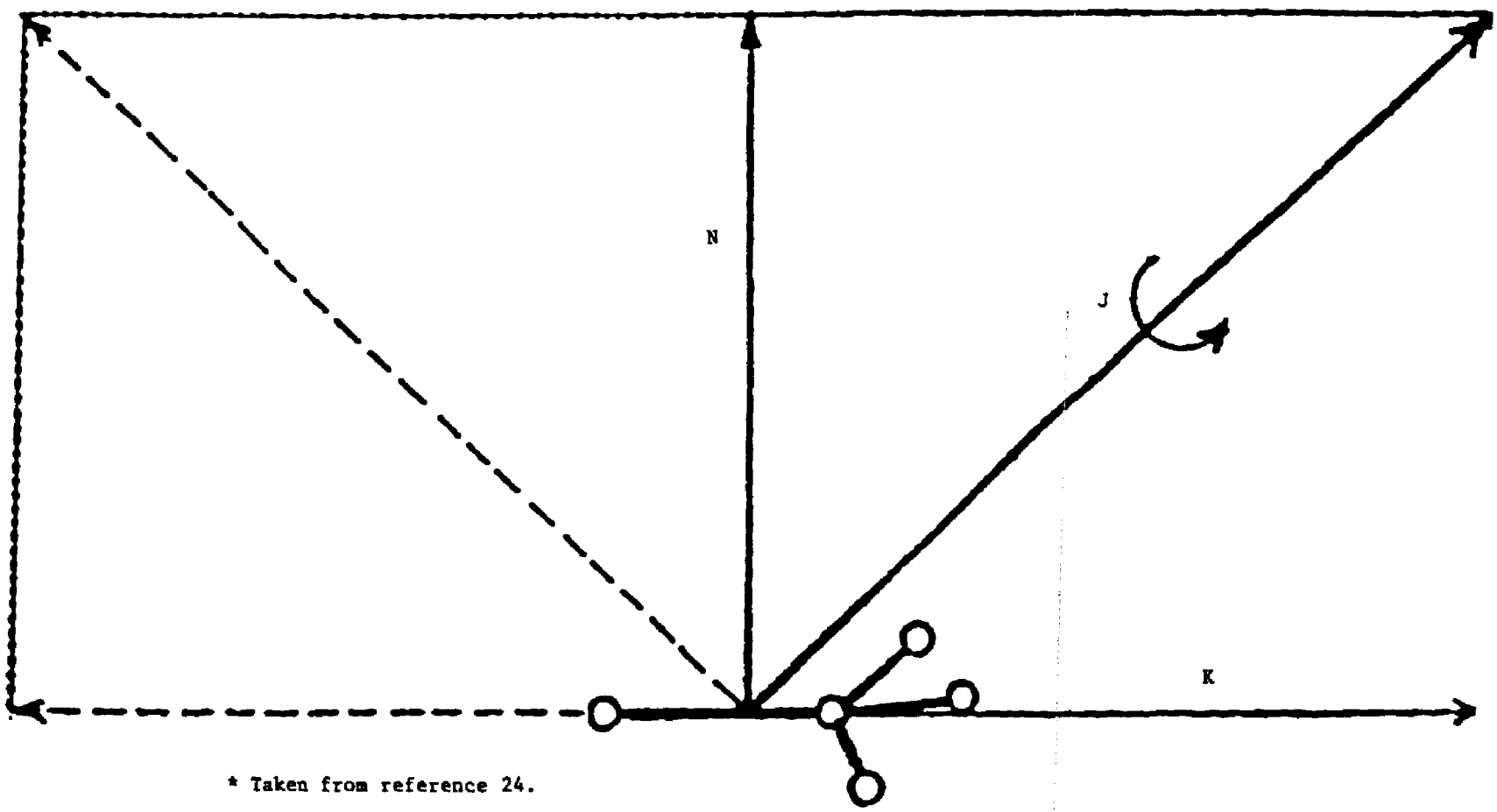

* Taken from reference 24.

are T_e' and T_e'', then the wavenumbers of all the possible rotational transitions for a given vibronic transition are represented by

$$\nu = (T_e' - T_e'') + [G'(v_i') - G''(v_i'')] + [F_v'(J',K') - F_v''(J'',K'')] \qquad (47)$$

Hence, according to equation (45), rotational spectra that are observed for a given vibronic transition represent differences in the rotational constants between the upper and lower vibronic states.

Since $\tilde{K} \equiv \tilde{J}_z$, the quantum number K cannot be greater then J. Therefore, for a given J,

$$K = J, J-1, J-2, \ldots, -J \qquad (48)$$

or, in other words, for every K value there is a series of rotational levels with

$$J = K, K+1, K+2, \ldots \qquad (49)$$

Since K is the component of J along the top axis, it can be either positive or negative, and states whose only difference is the sign of K have the same energy. They correspond to the two opposite directions of rotation about the figure axis. Thus all states with $K > 0$ are doubly degenerate.

In orbitally non-degenerate electronic states, the spin-orbit coupling is usually very small, but it does increase with increasing J and K. As for linear molecules, the quantum number N of the total angular momentum apart from spin is introduced and replaces J in all the previous symmetric top formulae. The spin $\tilde{S}$ is added to $\tilde{N}$ to give the total angular momentum $\tilde{J} = \tilde{N} + \tilde{S}$ and therefore the quantum number J takes on the values

$$J = N+S, N+S-1, \ldots, |N-S| \qquad (50)$$

so that each level of a given N is split into 2S+1 components.

3.2.3.2 SELECTION RULES FOR ROTATIONAL TRANSITIONS

For symmetric top molecules, when the transition moment of the electronic transition is parallel to the top axis, one has what are known as "parallel bands" in which the selection rules are

$$\Delta K = 0 \quad \Delta J = 0, \pm 1 \quad \text{if } K \neq 0$$

$$\Delta K = 0 \quad \Delta J = \pm 1 \quad \text{if } K = 0$$

On the other hand, when the transition moment is perpendicular to the top axis, one has what are known as "perpendicular bands" in which the selection rules are

$$\Delta K = \pm 1 \quad \Delta J = 0, \pm 1$$

Other selection rules based on the symmetry properties exist but are too numerous to warrant a full discussion in this brief summary.

3.2.3.3 TRANSITIONS BETWEEN NON-DEGENERATE ELECTRONIC STATES

An allowed electronic transition between non-degenerate electronic states of a molecule with a more-than three-fold axis of symmetry is necessarily a parallel transition ($\Delta K = 0$). This is so because the change of dipole moment for all allowed transitions in such a system is in the direction of the symmetry axis. Changes in any other direction would correspond to electronic transitions in which one or both of the states involved is degenerate.[25] For such a parallel band, only levels of the same K value can combine with one another. For a particular K value, since $\Delta J = 0, \pm 1$ (assuming $K \neq 0$), there exists a sub-band of three simple branches: P, Q, and R, corresponding to transitions with $\Delta J = +1, 0, -1$, respectively. The complete parallel band is

obtained by a superposition of a number of such sub-bands, corresponding to the various K values that occur at the temperature of observation. If the rotational constants A and B are not very different in the upper and lower electronic states, all the sub-bands will approximately coincide, since the spacing of the levels in the upper and lower states will be nearly the same. If one considers rotational constants that are different in the upper and lower electronic states, the sub-bands no longer coincide but are shifted slightly depending on the magnitudes of the differences between the ground and excited state rotational constants.

For less symmetric molecules, the change of dipole moment for a vibrational transition may also be perpendicular to the top axis and in that case $\Delta K = \pm 1$ can also occur. In fact, it may happen that the change of dipole moment makes an intermediate angle with the top axis. In this case, both $\Delta K = 0$ and $\Delta K = \pm 1$ may occur, and one has what is called a "hybrid" band. Such bands also consist of a number of sub-bands. However, even when the interaction of vibration and rotation is neglected, the sub-bands do not coincide. Rather, a series of lines formed by the Q branches of the different sub-bands becomes the most prominent feature in the spectrum while the lines of the P and R branches of the sub-bands form a less intense background.

4. EXPERIMENTAL APPARATUS

4.1 SUPERSONIC FREE JET CHAMBER

The practical limit to the performance of a supersonic expansion is the requirement of adequate pumping capacity to handle the gas discharge through the nozzle. This is true because one cannot produce cooling if the expanding gas is allowed to scatter from the background gas which is at ambient temperature since this scattering only reheats the molecules in the supersonic jet. To prevent this from occuring, our chamber is evacuated by a combination of a Leybold-Heraeus DK200 rotary piston pump and WS1000 roots blower. For a continuous flow (cw) nozzle with an orifice diameter of 200 μm and a typical backing pressure of 60 PSI behind the nozzle, this pumping system maintains the background gas pressure at 80-200 millitorr for argon and helium carrier gases. Although at these pressures the mean free path between background gas collisions is smaller than the dimensions of our experimental apparatus, the molecules in the jet do not experience heating. Campargue[29-31] was the first to understand the reason for this. He realized that if the background pressure was allowed to increase, shock waves would form around the cold, isentropic core of the expansion and shield the core from the warm background gas. This proved convenient experimentally since pumps of smaller volumetric pumping speed could be used to maintain the higher background pressure. Additionally, this approach was found to be particularly useful for spectroscopic experiments, since the shock waves surrounding the isentropic core do not affect the propagation of light.

Figure 9 illustrates the free jet chamber and light collection optics. L_1, L_2, L_3, and L_5 are 4 inch focal length biconvex lenses, L_4 is a 3 inch

focal length biconvex lens, S is a 200 μm slit, and F is a broadband filter. These optics serve to collect the laser induced fluorescence and discriminate against scattered laser light. The chamber is evacuated with the pumps mentioned above and is equipped with an MKS baratron (P_1) and a thermocouple gauge (P_2) for monitoring background gas pressures. Both are capable of measuring pressures down to $1x10^{-3}$ torr. Gases are expanded into the chamber through a 200 μm orifice. The carrier gases used in these experiments are argon and helium at backing pressures from 30 to 500 PSI. The counter-propagating photolysis/photoionizing and probe lasers enter the free jet chamber through Suprasil II UV quartz in the horizontal plane. These are located at the ends of 30 cm arms on each side of the chamber. The windows are mounted in rotatable flanges held at Brewster's angle in order to minimize reflective losses in passing both the photolysis/photoionizing and probe laser light into the chamber. Further, the chamber arms are equipped with light baffles to reduce the amount of background scattered radiation detected by the optical collection system. Both the lasers and the jet nozzle can be translated independently along the expansion axis, thereby allowing a variety of experiments to be attempted.

For the furan cation and the cyclopentadienyl radical experiments, the precursors used were furan (C_4H_4O) and cyclopentadiene (C_5H_6), respectively. The furan liquid (Aldrich Chemical Company, +99%) was used without further purification. The cyclopentadiene was formed by "cracking" a sample of dicyclopentadiene (Aldrich Chemical Company, 95%). This was accomplished by heating the dimer until it dissociated into two monomers. The resulting monomer vapor was passed through a water-cooled column where it condensed and subsequently dripped into a flask where it could be collected. This sample was maintained at -78° Celsius until needed for the experiment in order to

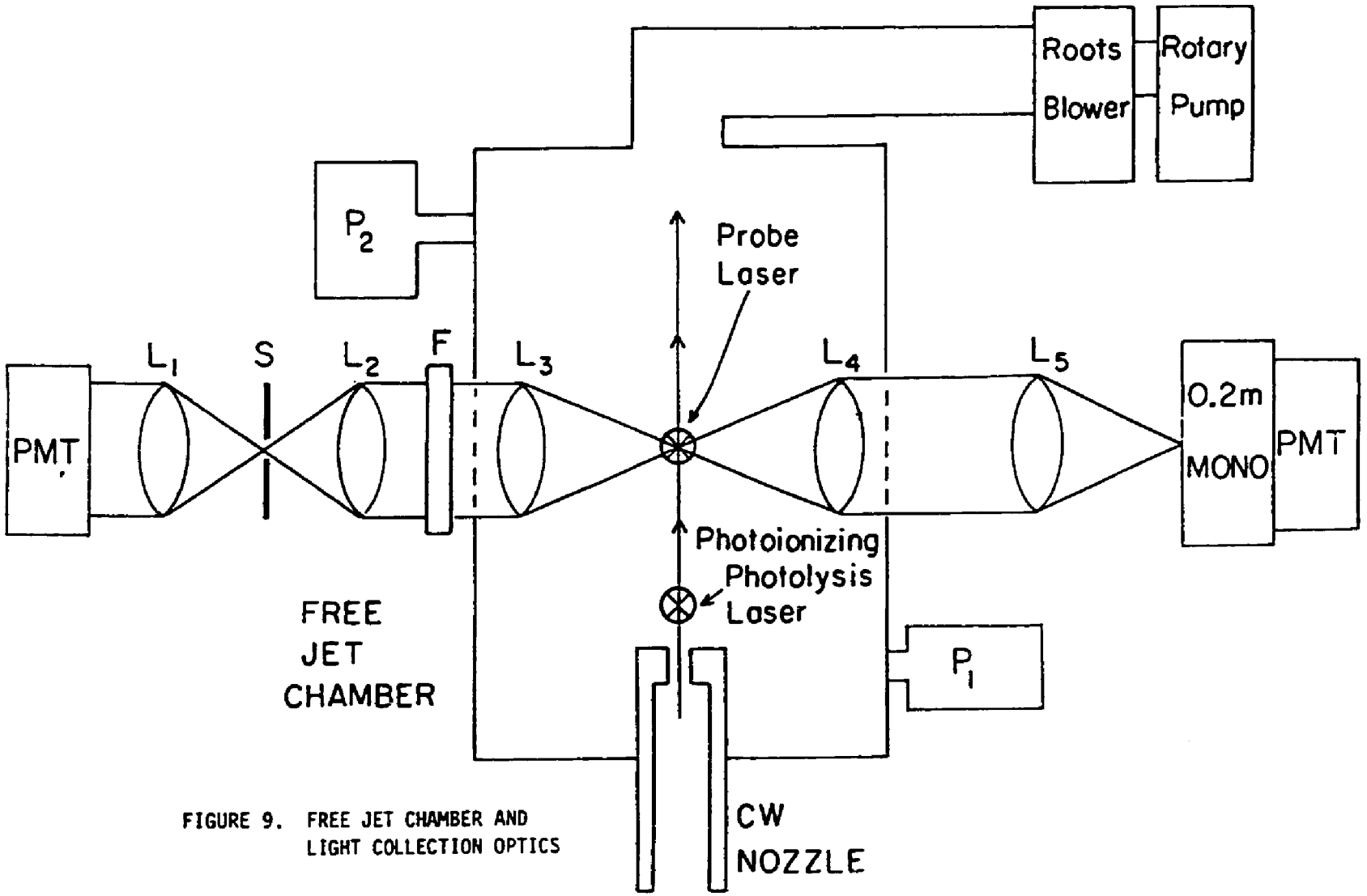

FIGURE 9. FREE JET CHAMBER AND LIGHT COLLECTION OPTICS

prevent dimerization from reoccuring. Each precursor was seeded into the carrier gas by placing it in a stainless steel sample cylinder which was cooled to -15° Celsius by a "slush bath" of crushed ice, NaCl, and water. The carrier gas was allowed to flow over the sample and entrain the resulting vapor pressure of the precursor into it. This mixture was subsequently expanded into the chamber through the 200 μm orifice. Based on observations of the density drop as a function of distance from the nozzle for both precursors, the free jet expansion behaved as one would expect for a monoatomic gas. This was so because the equations derived earlier for a supersonic free jet expansion assumed the use of a monoatomic ideal gas. Therefore, the presence of sizable amounts of polyatomic non-ideal gas molecules would cause significant departures from the behavior predicted by these equations. Since such departures are not observed, one may conclude that the gas mixture is predominantly composed of inert monoatomic carrier gas molecules. Hence, it is reasonable to estimate that the concentrations of both precursors were only ≤ 1% that of the carrier gases.

4.2 OVERALL EXPERIMENTAL SETUP

Figure 10 gives a view of the overall experimental setup. The photolysis/photoionizing laser is a Lambda Physik excimer laser (EMG101) operating on either ArF or KrF at a repetition rate of 10 Hz. The output pulses (193 nm or 248 nm, respectively; 200 mJ; 20 ns) are focussed by a one meter CaF lens onto the supersonic expansion at a point 1.5 mm downstream from the nozzle, corresponding to 7.5 nozzle diameters (nd) for the 200 μm orifice. The resulting species formed by the

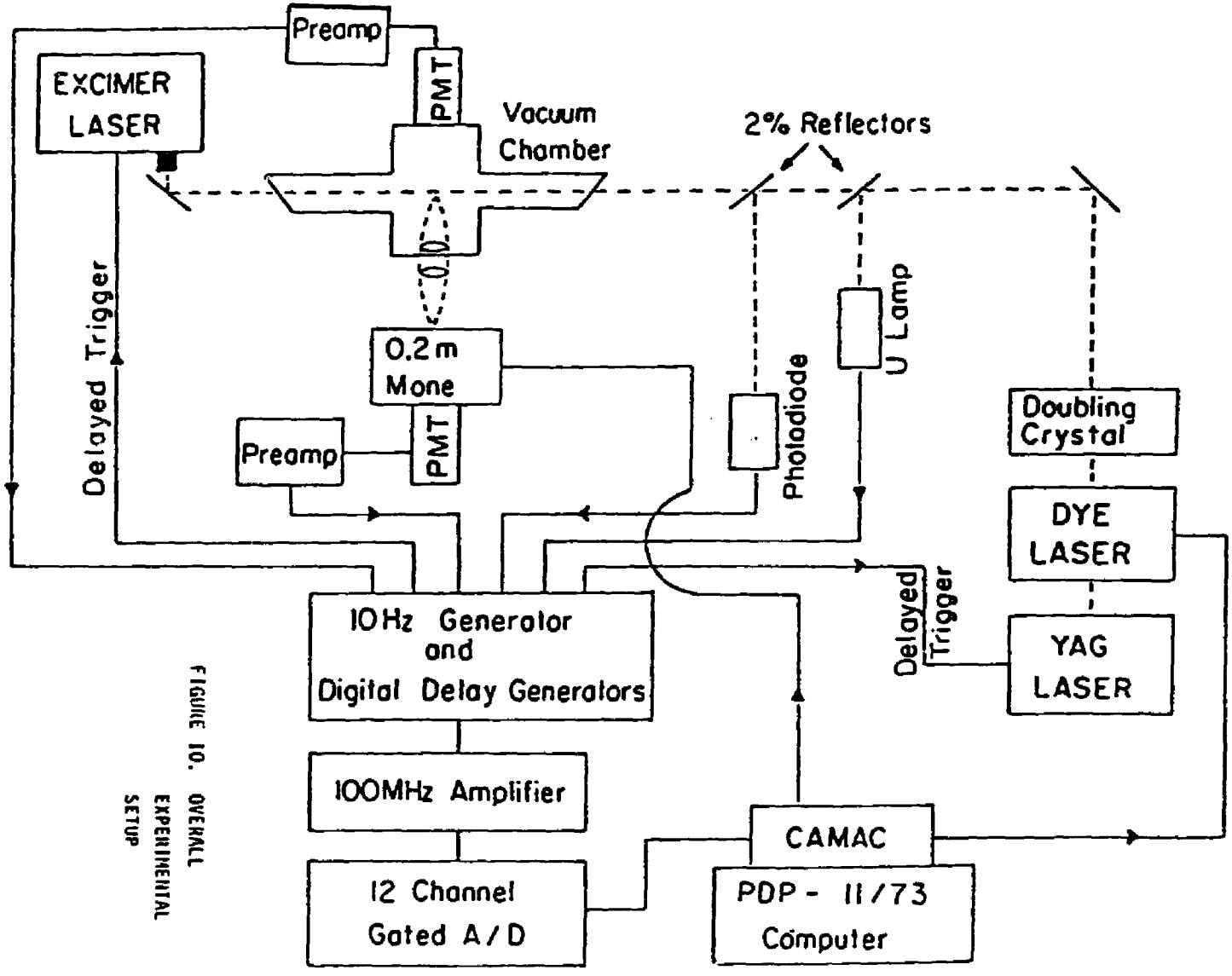

FIGURE 10. OVERALL EXPERIMENTAL SETUP

photolysis/photoionization are allowed to cool in the expansion until reaching 50 nd. At this point, laser induced fluorescence (LIF) and wavelength resolved emission (WRE) spectra are recorded using the temporarily delayed output of a grazing incidence dye laser, focussed onto the expansion by a one meter quartz lens. The dye lasers used are a Quantel TDL III and a homebuilt grazing incidence dye laser. The former operated at a linewidth of ~ 1 cm^{-1} and was used for obtaining vibrational resolution, while the latter was especially designed to have high efficiency at narrow linewidths for obtaining rotational resolution. The latter modifications will be discussed in detail in section 4.4. The dye laser is pumped by either the output of a Quantel Nd:YAG laser (Series 480) which is frequency doubled to 532 nm or the output of a Lambda Physik excimer laser (EMG101-MSC) operating on XeCl at 308 nm. A number of Exciton dyes were used in this study. Each was optimized for efficiency and linewidth at various concentrations in the appropriate solvents. When neccessary, the dye laser output was frequency doubled using 10 x 10 x 30 mm single crystals of potassium dihydrogen phosphate (KDP). Both KDP "C" and KDP "D" crystals (INRAD) were used in order to reach the desired transitions. The primary beam was condensed by a 250 mm focal length lens to achieve optimum intensity over the length of these crystals. The orientation of the crystal was tuned to match the refractive indices of the primary and secondary beams, and a number of filters (Esco 7-37, 7-51, 7-54, 7-59 and 7-60) were used in various wavelength ranges to isolate the second harmonic. A telescope, consisting of two quartz lenses, focussed the resultant beam into the fluorescence chamber. Uranium lamp optogalvanic spectra and I_2 laser induced fluorescence spectra obtained from homebuilt instruments were recorded simultaneously with all excitation spectra in order to provide an absolute frequency calibration. Etalon modes were also

recorded using either a 0.5 cm^{-1} free spectral range etalon coated for operation in the range 500-700 nm or a 1.0 cm^{-1} free spectral range etalon coated for operation in the range 370-440 nm (Virgo Optics). These provided frequency markers as well as providing a check on the linearity of the dye laser scans. Normalization of the data was achieved by monitoring the intensity of the dye laser output as a function of frequency with a PIN 40A photodiode (United Detector Technology, Inc.). For wavelength resolved emission data, reference lines from a mercury arc lamp were recorded through the monochromator in order to provide an absolute frequency calibration for these spectra as well.

4.3 LASER/VAPORIZATION CLUSTER SOURCE

During the course of conducting the optical emission studies on graphite, a different experimental setup was required from that given in section 4.1. The laser/vaporization nozzle design used was similar to that described by Dietz et al.[32] and others[9-12]. The modified experimental setup is given in Figure 11. A pulsed nozzle (Newport BV-100) was used in place of the cw nozzle and operated at a 10 Hz repetition rate. The second harmonic output of a Quantel Nd:YAG laser (532nm, 80mJ, 18ns) was used to vaporize materials from a high purity graphite rod. A 500 mm focal length lens focussed the laser normal to the rod's surface and transverse to the nozzle's 1mm diameter flow channel. The lens is held off focus and the spot size was measured at the surface to be 700 μm. The intensities achieved by such a configuration ranged from 0.1 to 2 GW/cm^2. The laser was timed to fire near the maximum of the carrier gas density and created a plasma which was entrained and cooled by

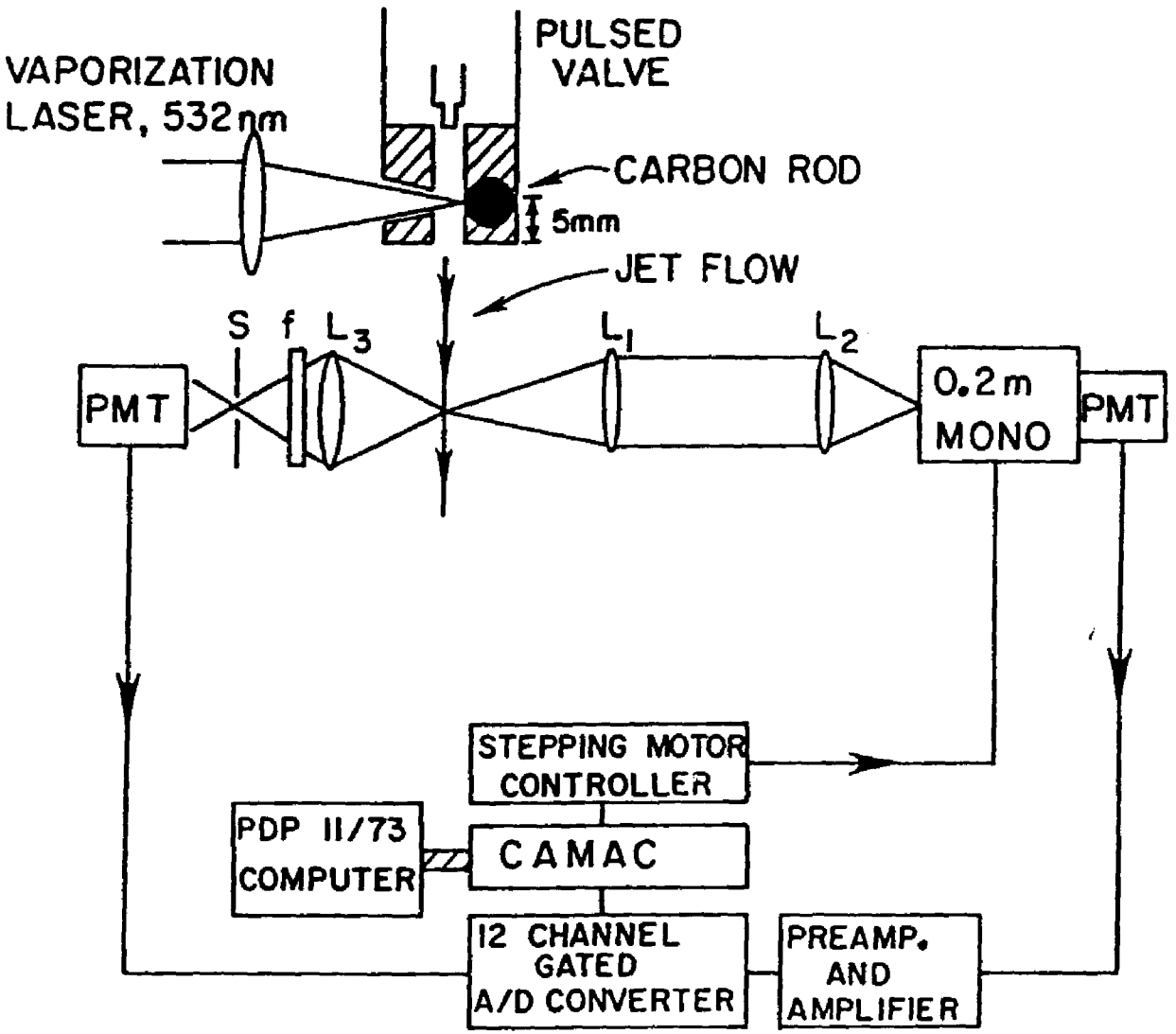

FIGURE 11. LASER/VAPORIZATION CLUSTER SOURCE

the gas. The carrier gases used were helium and argon at backing pressures from 15 to 150 PSI. The graphite target rod is continuously rotated and translated to expose a fresh surface to the vaporizing laser. The minimum distance from the interaction region to the orifice exit of the flow channel was 5 nd (1 nd = 1 mm). After exiting the channel the plasma/carrier gas flow was allowed to expand freely into a vacuum where the species were further cooled. At this point, the emission was monitored by a suitable optical collection system, the details of which will be discussed in section 4.5.

4.4 IMPROVED HOMEBUILT GRAZING INCIDENCE DYE LASER DESIGN

4.4.1 MOTIVATION

During the course of planning laser-induced fluorescence experiments aimed at obtaining rotational resolution on the vibrational bands in the $\tilde{B}$ electronic state of the furan cation, we designed and tested a modified version of the grazing incidence dye laser cavity in order to achieve higher efficiencies and narrower linewidths than those previously attainable with the conventional cavity design. Linewidth, efficiency, and relative power measurements for this modified design are discussed below and compared to the conventional grazing incidence dye laser cavity.

The grazing incidence cavity, as designed by Shoshan et al.[33] and Littman and Metcalf[34], is illustrated in Figure 12(a). W is a 4% reflecting wedged output window, DC is the dye cell, G is the diffraction grating, and M is the 100% reflecting tuning mirror. Narrow wavelength operation is achieved by allowing the broadband emission emerging from the dye cell to pass over the

surface of a diffraction grating at grazing incidence. In this configuration the grating exerts maximum angular dispersion on the spectral components of the incident light. A mirror is positioned to reflect a small frequency bandwidth from the first order of the grating back through the cavity, where it is further dispersed by the grating before passing through the amplifying medium in the dye cell and out of the 4% reflecting wedged output window. The frequency is tuned by rotating the feedback mirror.

The grazing incidence design is in wide use for a variety of reasons, including ease of alignment, narrow linewidth operation, low cost, and overall simplicity. However, the major drawback is the low conversion efficiencies that are attainable. Values from 1 to 3% are typical, and this can be a severe limitation if one wishes to probe transitions that are only weakly allowed. There are three major sources of this low conversion efficiency. First, diffraction gratings are inefficient at large angles of incidence. This is just a fact that laser spectroscopists must work with. Second, light is lost into unwanted diffraction orders. This loss may be minimized by the use of a holographic grating with a high number of lines per millimeter, since such a grating diffracts most of the light incident on its surface into its first order. Third, another loss is due to the divergence of the light in the cavity. This can be easily visualized by considering a light beam emerging from the dye cell with a beam waist w_1. This beam has a certain amount of divergence associated with it. As a result, after travelling to the mirror-grating pair, it returns to the dye cell with an expanded waist w_2 ($w_2 > w_1$). This larger beam waist (w_2) has a poor overlap with the active region of the dye (w_1), and consequently significant amounts of light are lost to absorption in the unpumped portions of the dye medium.

Lisboa et al.[35] and Yodh et al.[36] attempted to address this problem by

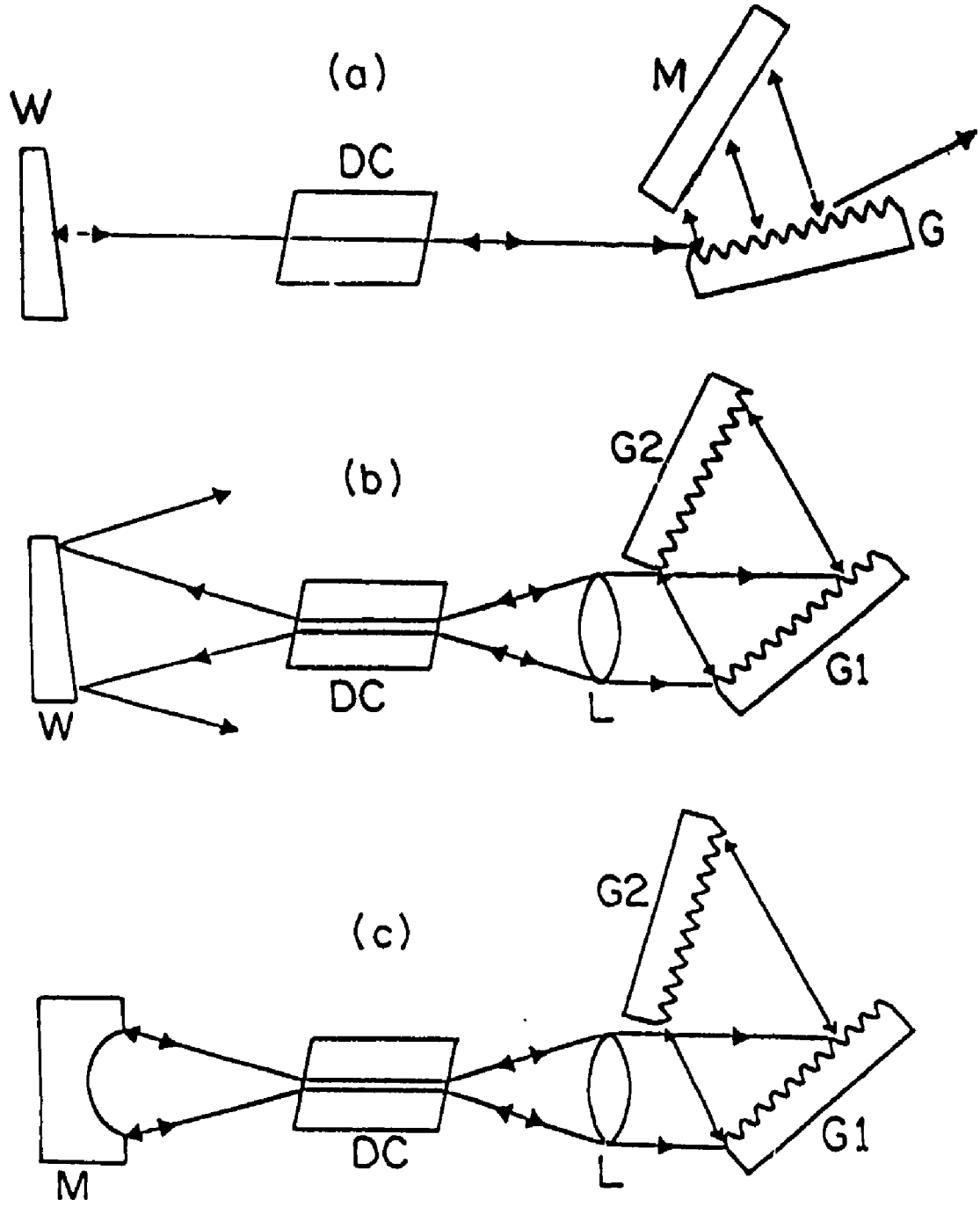

FIGURE 12. (a) CONVENTIONAL GRAZING INCIDENCE DYE LASER CAVITY
(b) LENS CAVITY
(c) MIRROR-LENS CAVITY

experimenting with the insertion of an intracavity lens between the dye cell and diffraction grating in a grazing incidence dye laser. The lens was positioned at a distance of approximately one focal length from the dye cell. This had the effect of increasing the overlap for a single pass between the returning light and the amplifying region of the dye cell by collimating the freely expanding light and then refocussing it through the same beam path ($w_1 = w_2$). However, during subsequent passes, the cavity becomes an unstable resonator. This is illustrated in Figure 12(b). L is the intracavity lens, and the other cavity elements are the same as in Figure 12(a). The light returning from the 4% reflecting window has the same poor coupling factor, or perhaps worse due to focussing effects, to the amplifying medium as without the lens.

To further improve the grazing incidence cavity, we studied a modified version of the lens design. A double-grating grazing incidence dye laser was operated with an intracavity lens, but the wedged output window was replaced with a 100% reflecting spherical mirror. The output was taken from the zeroth order of the diffraction grating. These changes resulted in both increased efficiency and reduced linewidth as compared to the conventional grazing incidence design. The foci of the lens and mirror were chosen so as to form an optically stable concentric resonator[37] ($R_1 = R_2 = d/2$, where R_1 and R_2 are the radii of curvature of the two optics and d is the separation between them). This design allowed the light to undergo many cavity passes, whereas the intracavity lens without the spherical mirror was only optically stable for a single pass. To convince oneself that the optically stable mirror-lens cavity is indeed multipass, one must only consider that the duration of the YAG or excimer laser excitation pulse is approximately 18 ns, whereas the time necessary for one round trip in a typical 28 cm long cavity is approximately 2

ns. This allows a total of nine round trips during the time of the excitation pulse, and therefore this is indeed a multipass cavity. The mirror-lens design also dramatically reduced the divergence losses in the cavity while simultaneously feeding back 100% of the light for further amplification. Additionally, the concentric design provided better definition of the active region within the dye medium, thereby preventing weak modes from achieving the gain necessary to oscillate. These changes incorporated all of the advantages of the intracavity lens while significantly improving the stability, linewidth, and efficiency of the output pulses as well.

4.4.2 MIRROR-LENS CAVITY

The mirror-lens cavity configuration is given in Figure 12(c). The homebuilt dye laser consisted of a 25 mm diameter 100% reflecting spherical mirror (M), a 12.5 mm wide flow-through dye cell (DC), two holographic gratings with 2400 lines/mm (G1 and G2), and a 25 mm diameter lens (L). The dye cell was held at Brewster's angle to minimize reflective losses in the cavity. For the particular experimental tests conducted on this laser, either a Lambda Physik XeCl excimer laser (5 mJ, 20 ns, 308 nm) or a Quantel Nd:YAG laser (5 mJ, 18 ns, 532 nm) was used to excite a 1.5×10^{-3} M solution of rhodamine 590 dye in methanol. The pump beam was focussed onto the dye cell with a 25 mm diameter, 75 mm focal length cylinder lens. The intracavity lens had a 100 mm focal length (R_1 = 100mm for the lens) and was positioned approximately one focal length away from the dye dell and as close as possible to the grating. The spherical mirror (Melles Griot 01LPK062, protected Al coating) had a 50 mm focal length (R_2 = 100mm for the mirror) and was

positioned 100 mm from the dye cell so that its radius of curvature overlapped that of the lens. The total cavity length was 28 cm. Both the lens and the mirror were mounted on translation stages for precise positioning.

4.4.3 LINEWIDTH ANALYSIS AND CAVITY STABILITY

In general, the linewidth of a grazing incidence dye laser is defined as

$$\Delta\lambda = \frac{\partial\lambda}{\partial\theta}\,\Delta\theta \qquad (56)$$

where $\partial\lambda/\partial\theta$ is the inverse of the angular dispersion of the grating and $\Delta\theta$ is the acceptance angle of the incident light onto the grating, i.e., the divergence. For the single-pass model[38], the angular dispersion in a double-grating cavity is given as

$$\frac{\partial\theta}{\partial\lambda} = \frac{1}{\cos\theta}2\alpha + \frac{\cos\phi}{\cos\theta'} + \beta \qquad (57)$$

where θ is the grazing angle, ϕ is the angle between the normal to the grating surface and its first order diffracted beam, θ' is the angle between the normal to the Littrow grating surface and its incoming beam, and α and β are the ratios of diffraction order to groove spacing for the grazing incidence and Littrow gratings, respectively. The important point to note is that as θ approaches 90 degrees the angular dispersion attains its maximum value, and hence the linewidth attains its minimum value. This is the principle of operation underlying the grazing incidence design. As is obvious from equation (56), the divergence affects the linewidth. If the incident light beam fills up the grating so that the grating becomes the limiting aperture in the cavity, diffaction affects will arise, and the divergence will increase with θ so that

$$\Delta\theta \propto \frac{\lambda}{l\cos\theta} \qquad (58)$$

where λ is the wavelength of the light and l is the length of the grazing incidence grating. Therefore, further improvements in linewidth beyond this grating-limited angle are difficult to realize due to the effects of the increased divergence. If the grating is not the limiting aperture in the cavity, the intracavity lens is able to reduce the divergence of the beam much more significantly and hence the linewidth as well. Physically, this is easy to visualize by considering the change in beam geometry induced by the lens. Prior to the insertion of the lens, many spectral components of the diverging light were allowed to oscillate in the cavity because the variety of incidence angles onto the grating made it possible for more of them to follow the same beam path and thereby simultaneously satisfy the cavity boundary conditions. By collimating the beam with the lens, many of these paths are eliminated so that the modes corresponding to them can no longer contribute to the linewidth.

For a two-element resonator, optical stability is determined by the following relation

$$0 < g_1 g_2 < 1 \qquad (59)$$

where $g_1 = 1 - d/R_1$ and $g_2 = 1 - d/R_2$. R_1 and R_2 are the radii of curvature of the two optics and d is the separation between them. This relation defines a region of optical stability bounded by hyperbolas in the first and third quadrants of the g_1-g_2 Cartesian plane. For the conventional grazing incidence dye laser, $g_1 g_2 = 1$ ($g_1 = 1$ and $g_2 = 1$), and the cavity lies directly on one of these hyperbolas at the boundary for optical stability. For the mirror-lens cavity, $g_1 g_2 = 1$ ($g_1 = -1$ and $g_2 = -1$), and this cavity lies on the hyperbola at the opposite edge of optical stability. However, the intracavity lens design with a wedged output window has $g_1 g_2 < 0$ ($g_1 = 1$ and $g_2 < 0$ since $d > R_2$), and this cavity lies outside the region of optical

stabilty. Therefore, it is an unstable optical resonator. Hence, the use of a spherical end mirror in place of the wedged output window represents a significant improvement in the stability of the dye laser cavity.

4.4.4 LINEWIDTH AND EFFICIENCY RESULTS

The results of our linewidth studies are presented in Figure 13 as a function of grazing angle. The mirror-lens cavity achieved linewidth improvements of 25-40% over the conventional cavity. Linewidths as small as 0.05 cm^{-1} were achieved. It should be possible to obtain further linewidth reductions with the mirror-lens design by using optics of smaller foci so that a decreased cavity length can be used. This would have the effect of further separating the longitudinal cavity modes, since this spacing is inversely proportional to the cavity length. Therefore, some modes would no longer have enough gain to oscillate in the cavity and could not contribute to the spectral linewidth. Another method to reduce the number of modes in the cavity is to use a thinner dye cell so that the active medium path length is decreased and a better defined source is present. This would have the effect of decreasing the number of high gain pathways through the active medium.

Our relative power measurements are presented in Figure 14. We reproduced the results of Yodh et al. for the lens cavity with a wedged output window and also obtained significantly larger improvements with the mirror-lens design. For the mirror-lens configuration the output was taken from the zeroth order of the grating, while the front window output was used for the conventional cavity. This was done to compare our results to those of Yodh et al. where factors of ~ 2 improvement were observed for the front window output

FIGURE 13. LINEWIDTH VS. GRAZING ANGLE FOR THE CONVENTIONAL AND MIRROR-LENS CAVITIES

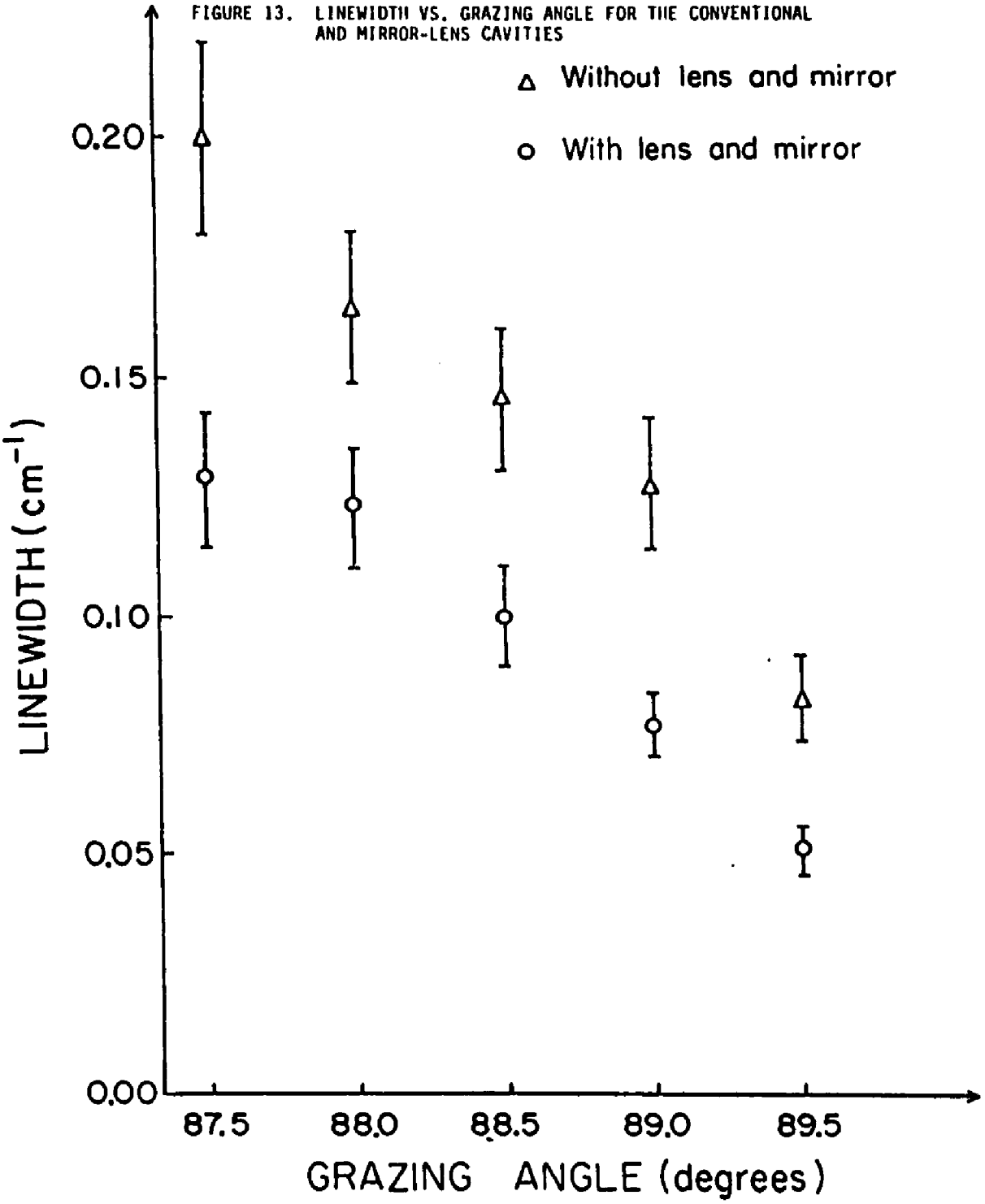

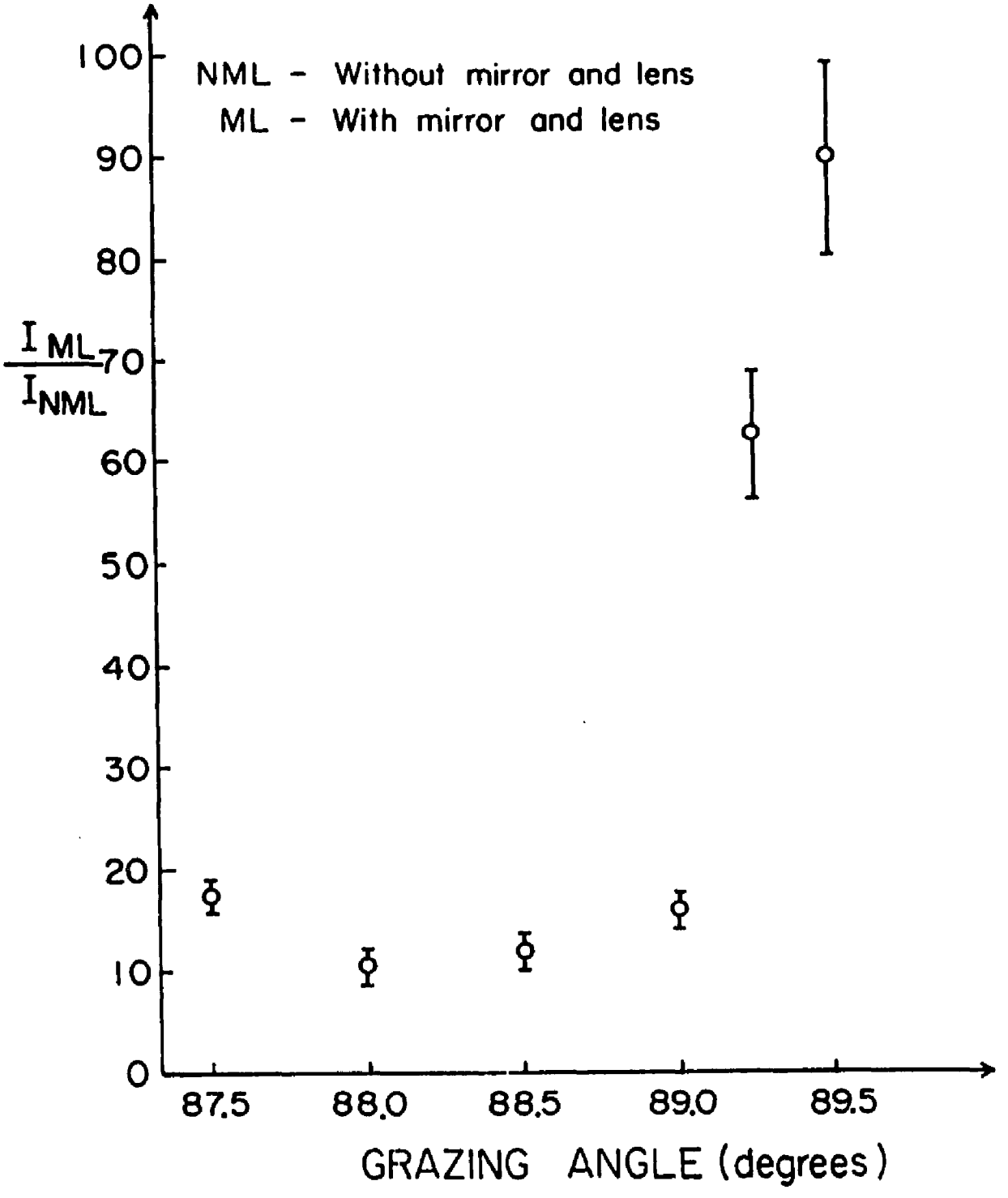

FIGURE 14. RELATIVE POWER VS. GRAZING ANGLE FOR THE CONVENTIONAL AND MIRROR-LENS CAVITIES

of the lens cavity as compared to the conventional one. For the mirror-lens design, factors of 10-20 improvement over the front window output of the conventional cavity were typically obtained. These factors were reduced to 4-8 when compared to the zeroth order output of the same cavity. In addition, the mirror-lens cavity allowed us to operate at grazing angles where the conventional cavity would either lase weakly or not at all.

Efficiencies are compared in Table 2. B represents the conventional or basic cavity, ML is the mirror-lens cavity, FW is the front window output, and DG is the zeroth order output of the diffration grating. The term stimulated efficiency is meant to indicate that the above results are due to stimulated radiation only. The spontaneous contribution was measured and subtracted before these efficiencies were calculated. Stimulated light efficiencies of 15% for the mirror-lens cavity were obtained. The ratio of stimulated to spontaneous emission was determined by aperturing the laser light and allowing a representative sample to strike the surface of a diffraction grating where the spectral components were dispersed and separated for measurement. The mirror-lens design consistently improved the percentage of stimulated light coming off the zeroth order of the grating as compared to the conventional cavity.

Although the improvements reported here were obtained with a double-grating grazing incidence dye laser, the mirror-lens design yielded stable efficient narrowband operation for a single-grating-tuning mirror dye laser as well. In addition, the beam quality in both the grating-grating and grating-tuning mirror configurations was improved by the addition of the spherical end mirror and intracavity lens. The divergence of the dye laser beam was greatly reduced in comparison to the conventional cavity as a result of the collimating effects of the mirror-lens combination. One benefit of this is to

CAVITY	OUTPUT	STIMULATED LIGHT (%)	STIMULATED LIGHT EFFICIENCY (%)
B	FW	99	1.5
B	DG	50	2.5
ML	DG	63	15.0

TABLE 2

STIMULATED LIGHT EFFICIENCIES IN AN IMPROVED HOMEBUILT GRAZING INCIDENCE DYE LASER

increase conversion efficiencies during subsequent stages of amplification, since a well-collimated seed beam can more efficiently fill an amplifying medium than a strongly diverging one.

Additionally, although the amount of spontaneous emission present in the dye laser output depends on many factors, including dye concentration and pump power, it is well known that the output from the zeroth order of the diffraction grating contains a large percentage of spontaneous light. Typically we measured values of ~ 50% for the double-grating cavity without additions. The mirror-lens cavity reduced this quantity to 30-35% while operating at a linewidth of 0.1 cm^{-1}. Further improvements in the ratio of spontaneous to stimulated emission can be achieved by various methods. In particular, the bent cavity design, in which the cavity optics are positioned so that the dye laser beam undergoes total internal reflection from the inside surface of the dye cell, could help improve this ratio, since the majority of spontaneous light exits the cavity at a different angle from that of the stimulated light and is therefore not included in the output beam. Another alternative cavity[39] can be constructed by returning to the 4% reflecting window and positioning two lenses of the same focal length on either side of the dye cell. While this cavity will not be as efficient as the mirror-lens design, it is also a concentric resonator and should achieve stable and more efficient output pulses than the conventional cavity. In addition, it would allow one the option of using the front window output which typically contains much lower amounts of spontaneous emission (< 1%).

4.5 OPTICAL COLLECTION SYSTEM

The optical collection system consisted of a photomultiplier (PMT) system and a monochromator-PMT system. The PMT (Hamamatsu R446) system was used in combination with a broadband filter to record laser induced fluorescence (LIF) excitation spectra, i.e., the total fluorescence yielded as a function of probe laser frequency. Suitable collection optics, filtering, and aperturing limited the viewing region to a well defined solid angle. This is critical so that the detector views only a very limited set of molecular temperatures and discriminates against background emission caused by the photolysis/photoionizing laser. The monochromator-PMT system was used to disperse the LIF produced by the probe laser held at a fixed frequency. The emission was collected normal to the expansion axis with an f/4 optical system and was imaged onto the 150 μm slit of a Jarrel-Ash 0.2 m monochromator, which is equipped with two interchangeable gratings. The resolution of the monochromator with 150 μm slits is three angstroms for the low blaze grating and six angstroms for the high blaze one. These gratings are blazed such that they have peak efficiencies at 300 and 600 nm, respectively. The output is monitored by a Hamamatsu R282 PMT. This optical system provides not only frequency selectivity but spatial resolution as well.

The Hamamatsu R282 is a side-on type photomultiplier tube having a spectral response in the range 185-700 nm with a peak sensitivity at 450 nm. It is equipped with a nine stage dynode chain and has a UV quartz window. The rise time of this detector is 2.2 ns and a typical dark current is 2 nanoamps. The Hamamatsu R446 PMT is identical in most respects to the R282 except for the fact that its spectral response lies in the range 185-870 nm with a peak sensitivity at 330 nm. These detectors were typically operated

with 1000 volts DC applied to the dynode chain.

4.6 DATA COLLECTION

The PMT outputs for both the excitation and dispersed fluorescence spectra were amplified at the free jet chamber by homebuilt 275 MHz preamplifiers (x10) and subsequently fed into a Lecroy 6102 100 MHz amplifier along with all calibrations. The amplifier had an input range which is variable from 50 mV peak-to-peak to 250 mV peak-to-peak with an accuracy of ± 3% of the full scale. A front panel potentiometer allowed the output to be DC offset up to 100 mV positive or negative with a drift of less than ± 200 μV/°C. After amplification the signals were collected by a Lecroy 2249SG 12-channel, gated analog-to-digital converter. Each channel had a 10-bit conversion to provide a total dynamic range of 1024 counts per laser shot. The performance of the A/D converter was linear for gate sizes up to 200 ns but could be operated with gate sizes up to 2 μs with reduced accuracy. Control of the dye laser and monochromator frequency was accomplished via model 3361 and 3362 CAMAC stepping motor controllers. These devices were capable of handling up to 32,767 steps with one command and were velocity programmable up to 5000 steps per second. In practice, the actual data was collected by stepping the dye laser or monochromator to a particular frequency, averaging the signal over many laser shots, storing the value obtained, then stepping by a desired frequency increment, averaging again, storing, and repeating this procedure until the scan was finished. We wrote a variety of fortran programs to communicate with the CAMAC modules and the A/D converter. These controlled the data acquisition and storage and allowed the

experimenter the freedom to pre-select a particular dye laser, dye laser drive, monochromator, low or high blaze grating, frequency range, incremental step size, number of laser shots to average over, and number of channels of the A/D converter to simultaneously utilize. Further, we wrote additional programs to aid in data analysis. These were capable of manipulating the data in a variety of ways, including x- and y-axis expansions, wavelength-to-frequency conversions, data set divisions for normalization, relabelling of x- and y- axes for calibration purposes, and overlaying of various data sets for comparisons. Both the A/D converter and stepping motor controller were interfaced via a CAMAC maxima-885 crate and LSI-11 crate controller to a PDP 11/73 computer system. The PDP 11/73 consisted of a 11/73 central processing unit, 1 Mb of memory, 20 Mb of hard disk, 1 Mb of floppy disk, graphics terminal, and printer. This system provided automation of the experiment and allowed immediate storage, calibration, and normalization of the data. Four digital delay generators provided all the necessary triggers and timing sequences for the lasers and electronics.

5. LASER INDUCED FLUORESCENCE STUDY OF THE $\tilde{B}\ ^2B_2 \rightarrow \tilde{X}\ ^2A_2$ TRANSITION OF THE FURAN CATION IN A SUPERSONIC FREE JET EXPANSION

5.1 MOTIVATION

Furan (C_4H_4O) is a five-membered aromatic ring which forms the base for a series of heterocyclic compounds of importance in biochemistry and synthetic chemistry. Such aromatic substances are generally defined as homocyclic or heterocyclic hydrocarbon compounds with structures and chemical properties similar to those of benzene[40]. Applications extend to a wide variety of areas, including synthetic fuel products, pharmaceuticals, dye solvents, insecticides, and coal conversion technology.[41,42]

While spectroscopic information on the furan molecule is abundant[43-49], the corresponding experimental data on the furan cation is essentially non-existent. In fact, the only experimental observations of the furan cation reported thus far are in electron spin resonance studies[50,51] and photoelectron spectra[52-55]. The first were performed on matrix-isolated furan exposed to γ-irradiation at 77K, where the ions are subject to intermolecular perturbations due to implantation in the solid low temperature matrix. The second were performed on gaseous furan at room temperature, but the resolution of the experiment was too poor to assign more than the electronic energy levels and a few higher frequency vibrations. To date, no one has obtained a complete, well-resolved vibrational spectrum on any electronic state of the furan cation, and rotational spectra have not even been attempted. This is largely due to the fact that no one has been able to isolate this species in the gas phase in a low temperature environment.

From a theoretical point of view, the furan cation is a most interesting

species. It is not only intimately related to the furan molecule but is also isoelectronic with the cyclopentadienyl radical (C_5H_5) and, as such, may be useful in gaining a better understanding of this complicated system. Due to its symmetrical D_{5h} geometry, the ground state of the cyclopentadienyl radical is electronically degenerate and therefore, in accordance with the Jahn-Teller Theorem[28], it distorts to a lower symmetry in order to lift this degeneracy. The vibrations corresponding to the Jahn-Teller active modes become allowed in the spectrum of C_5H_5 and the resulting energy levels are highly anharmonic leading to a very complicated spectrum. In the furan cation, this electronic degeneracy is lifted due to the presence of an oxygen atom in the five-membered ring. The resulting C_{2v} geometry leads to a non-degenerate spin doublet ground state and a low lying first excited ($\tilde{A}$) electronic state at approximately 11,450 cm^{-1} above it[51]. An understanding of the ground state vibrational structure in $C_4H_4O^+$, which will naturally be perturbed to some extent by the presence of this low lying excited electronic state, may yield some insight into the Jahn-Teller effect in its isoelectronic partner C_5H_5.

5.2 FORMATION AND IDENTIFICATION

5.2.1 FORMATION MECHANISM

The furan cation was formed via a two-photon ionization of the furan molecule with 193 nm radiation from an ArF excimer laser.

$$C_4H_4O + 2h\nu \rightarrow C_4H_4O^+ + e$$

The photolysis/photoionization was performed 1.5mm, or 7.5 nd, downstream from the 200 μm orifice in the free jet chamber, and pulse energies of 100-200 mJ were used. The prompt fluorescence given off by the photolysis process itself was extremely bright and could easily be observed visually in our apparatus. The furan cation laser induced fluorescence signal did saturate at high laser intensities. However, no signal loss due to fragmentation caused by excessive laser pulse energies was observed. Further, the LIF signal showed a two-photon dependence on laser intensity. After formation, subsequent collisions with the supersonic jet's inert carrier gas molecules cooled the ion rotationally, translationally, and, to a lesser extent, vibrationally. This led to well-resolved excitation spectra which were limited chiefly by probe laser linewidth. Downstream from the jet nozzle, this "cold" ion was probed in the gas phase in a collisionless environment which was free from intermolecular perturbations, which might have otherwise affected the molecular structure.

5.2.2 IDENTIFICATION OF THE ELECTRONIC ORIGIN

In Figure 15, we show the $\tilde{B} \rightarrow \tilde{X}$ excitation spectrum of the furan cation taken at low resolution in the free jet expansion. To establish 24,675 cm^{-1} as the origin of the electronic transition, three experiments were performed. First, a wavelength resolved emission spectrum was recorded for excitation at 24,537 cm^{-1}, since this is the position of the only substantial structure located to the low frequency side of our proposed origin. This spectrum clearly revealed the presence of emission at a higher frequency than that of the pumping laser, indicating that this structure is a hot band. In

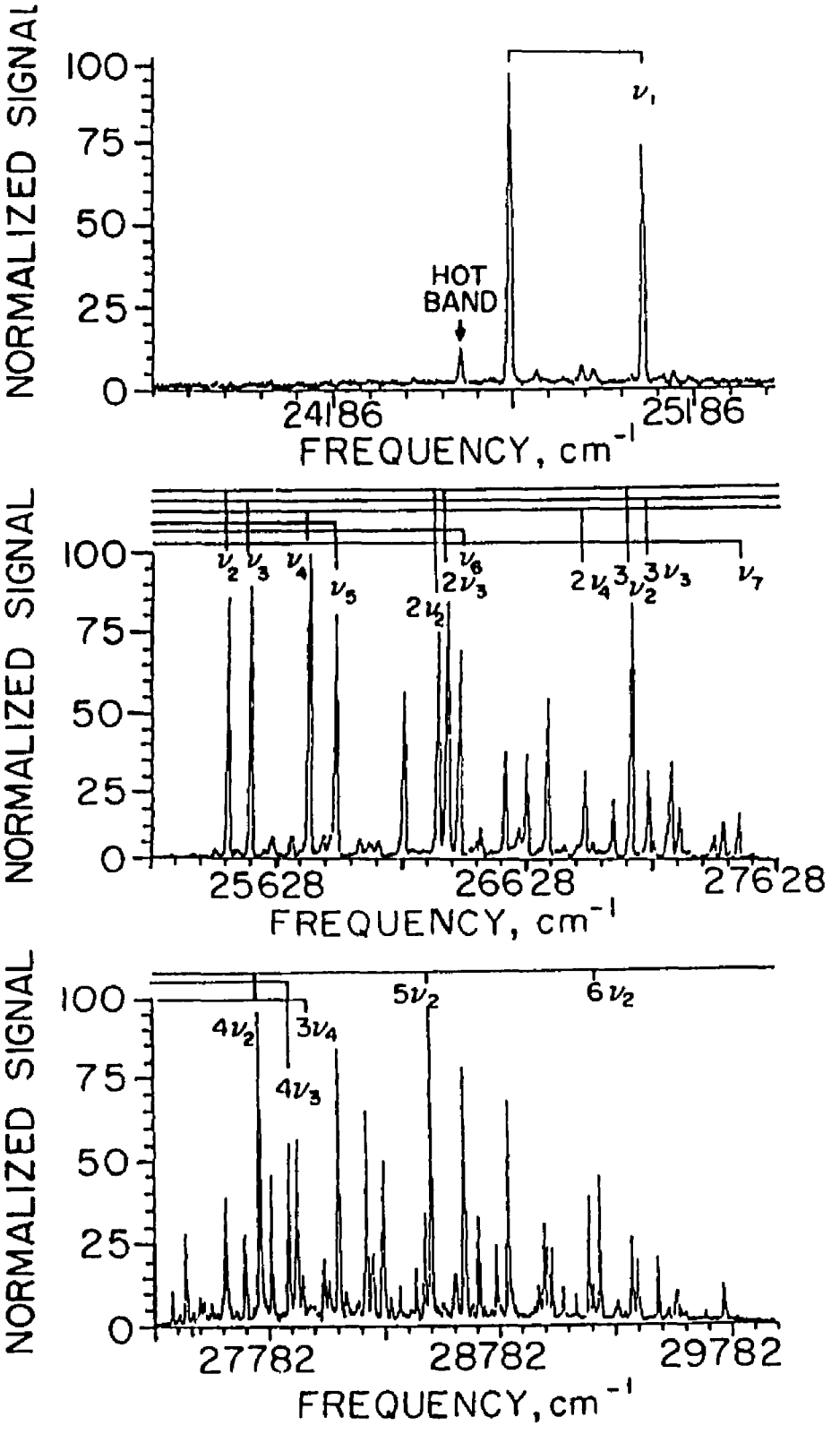

FIGURE 15. LIF EXCITATION SPECTRUM OF THE FURAN CATION

addition, this peak is displaced from the proposed origin by 138 cm^{-1}, which agrees well with a ground state frequency. This further indicates that 24,537 cm^{-1} is a hot band. Secondly, LIF spectra were recorded in both helium and argon carrier gases under experimental conditions that were otherwise identical. Cooling of the species was typically more complete in argon than in helium. Therefore comparison of scans taken in the two different gases facilitated the identification of hot bands. In changing from argon to helium, the band at 24,537 cm^{-1} increased in intensity by a factor of three, illustrating its hot band nature. However, the intensity of our proposed origin at 24,675 cm^{-1} decreased by 20%, which is expected if there is a loss of population in the vibrationless level of the ground electronic state due to incomplete cooling of the species by the carrier gas. This indicates that our proposed origin is not a hot band. Thirdly, our LIF spectra were extended to a point 1000 cm^{-1} lower than the proposed origin without observing any further signals. Since a number of fundamental frequencies in the excited state are smaller than this, absence of their harmonics within this region is evidence that 24,675 cm^{-1} is in fact the origin of the electronic transition.

5.2.3 IDENTIFICATION OF THE FURAN CATION AS THE CARRIER OF THE SPECTRUM

5.2.3.1 ELECTRIC FIELD PLATE AND JET HEATING STUDIES

Identification of the species under investigation as the furan cation is conclusive for a number of reasons. Electric field plate studies conducted at the photolysis region in the free jet chamber indicate the presence of a large number of positively charged species in our source. These experiments were

performed with a pair of 1.5 x 3.0 x 0.3 mm field plates, machined from stock aluminum. These were electrically isolated by mounting them on plexiglass holders. The plates were separated by approximately 2 cm and positioned about the nozzle such that the ArF photolysis occurred between them. To detect positive charges (i.e., positive ions), we used a Hewlett-Packard DC power supply (model 6209B) to generate a DC voltage of -40 V on one of the field plates. The other plate was grounded. This corresponded to an electric field of -20 V/cm. The change in current induced by the creation of positive charges during the photolysis was monitored by observing the change in voltage drop that occured across the field plates with a Tektronix 2235 100 MHz oscilloscope. This was accomplished by capacitively coupling the signal and terminating it into a 1 MΩ resistance. After exposing the vacuum chamber to furan and evacuating, a residual background signal of 10 mV was observed with a temporal full-width-at-half-maximum (FWHM) of 30 μs. However, when the furan gas mixture was actually being photolized in the free jet expansion, our signal increased to 200 mV with a FWHM of 100 μs. These studies indicate that a large number of positively charged species are created as a result of the ArF laser photolysis of furan in a supersonic free jet expansion.

Additionally, subsequent closer inspection of the LIF peak at 27,759 cm^{-1} indicates that the species under investigation is in fact the parent ion. This was evidenced during an experiment in which the dye laser position was held fixed while the excimer laser position was translated farther from the nozzle, thereby increasing the separation between the photolysis region and the exit orifice of the free jet expansion. Typically, the excimer laser position was translated from 7.5 nd to a distance of 32.5 nd from the jet nozzle. This had the effect of dropping the density of carrier gas molecules in the photolysis region and drastically reducing the number of two-body

collisions that could subsequently take place. For a fragment, photolysis of the precursor molecule typically leaves it internally excited with significant population in higher lying rotational and vibrational levels. Subsequent collisions with carrier gas molecules in the free jet expansion cool it by quenching these states and the resulting "cold" species are probed by the dye laser downstream from the formation region. By increasing the nozzle-excimer laser distance, the amount of time that the species can be in contact with the carrier gas "bath" before being probed by the dye laser is limited and therefore the number of cooling collisions that can take place substantially reduced. If the species under investigation were in fact a fragment of the furan molecule, it should have exhibited rotational, and probably vibrational, heating as a result of decreasing the number of such cooling collisions. Observation of the resulting signal indicated that no appreciable internal heating of the band was occurring. On the other hand, a parent ion formed by a dipole allowed, one or more photon ionization from the ground state of a "cold" molecule is not expected to be affected by such a change in collisional frequency, rather it would remain internally cold throughout, i.e., cold molecules give rise to cold parent ions because the rotational quantum number J is preserved in the transition[56]. This is the behavior that we observe. The band at 27,759 cm^{-1} was not significantly affected by decreasing the excimer-dye laser distance, and this is good evidence that the carrier of the spectrum is not a fragment molecule or ion but is indeed formed by ionization of furan.

5.2.3.2 COMPARISON TO THE ABSORPTION SPECTRUM OF FURAN

The absorption spectrum of furan vapor recorded by Watanabe and Nakayama[43] exhibits a sharp band at 191.5 nm. In addition, there is a weak diffuse band with a broad maxima at 195.3 nm. These results were confirmed by Pickett[44] and Price and Walsh[46]. The sharp structure at 191.5 nm is the most prominent band in the spectrum, and Herzberg[25] lists it as the 0-0 band of the $\tilde{B}$ electronic state of furan. This evidence indicates that the spectrally broad 193 nm output of our ArF excimer laser is near-coincident with an energy level of furan, and therefore photoionization of furan may likely be a near resonant two-photon process in this instance. The multiphoton ionization of furan reported by Cooper et al.[42] supports this conclusion. These workers recorded time-of-flight mass spectra for multiphoton ionization of furan at 376 nm (2 photons ~ 188 nm) and 550.5 nm (3 photons ~ 183.5 nm). For the former the dominant product is by far the parent ion, but for the latter the parent ion is either not observed or only very weakly evident. Ionization at 376 nm corresponds to a three-photon process, involving a two-photon resonance (at 188 nm) to the $\tilde{B}$ state of furan followed by a one-photon absorption leading to ionization.

5.2.3.3 TIME-OF-FLIGHT MASS SPECTROSCOPIC ANALYSIS

To confirm that the 193 nm radiation does give rise to significant amounts of the furan parent cation, we recorded a mass spectrum of the ion products resulting from the photoionization/photolysis of furan exposed to 193 nm radiation in a supersonic free jet expansion. This experiment was carried

out with the facilities of Dr. Trevor Sears at Brookhaven National Laboratory. The experimental apparatus consisted of a double-field time-of-flight mass spectrometer of the type described by Wiley and McLaren[57]. The repeller plate voltage was +50 V and served to push the positively charged species into the flight tube. At this point, a flight tube field plate, biased at -600 V, accelerated the various masses at different rates so that their arrival times at the detector could be distinguished, and hence their masses resolved. Additionally, the mass spectrometer was equipped with an "einzel" lens[58], which served to "focus" the different mass bunches by reducing their spatial extent and thereby increasing the resolving power of the instrument. The results of our mass spectroscopic analysis are illustrated in Figure 16 for a nozzle-excimer laser distance of 1.3 mm, or 6.5 *nd*. As suspected, the most prominent mass peak corresponds to that of the furan cation. Contributions due to smaller fragment ions are also present but in much smaller quantities. This demonstrates conclusively that there are large amounts of furan cation in our source. Further, the same spectrum recorded with KrF laser (248 nm) photolysis showed a lesser yield of $C_4H_4O^+$, indicating that the 193 nm photoionization is an enhanced process.

5.2.3.4 PHOTOELECTRON SPECTRUM OF FURAN

The term value T_{00} obtained for the $\tilde{B} \rightarrow \tilde{X}$ electronic transition in the furan cation corresponds to an excited $\tilde{B}$ electronic state lying 3.07 eV above the ground state. This differs dramatically from earlier values reported by Derrick et al.[53] and Eland[52] from photoelectron spectra of the furan molecule. Eland's value of 13.06 eV for the vertical ionization potential of

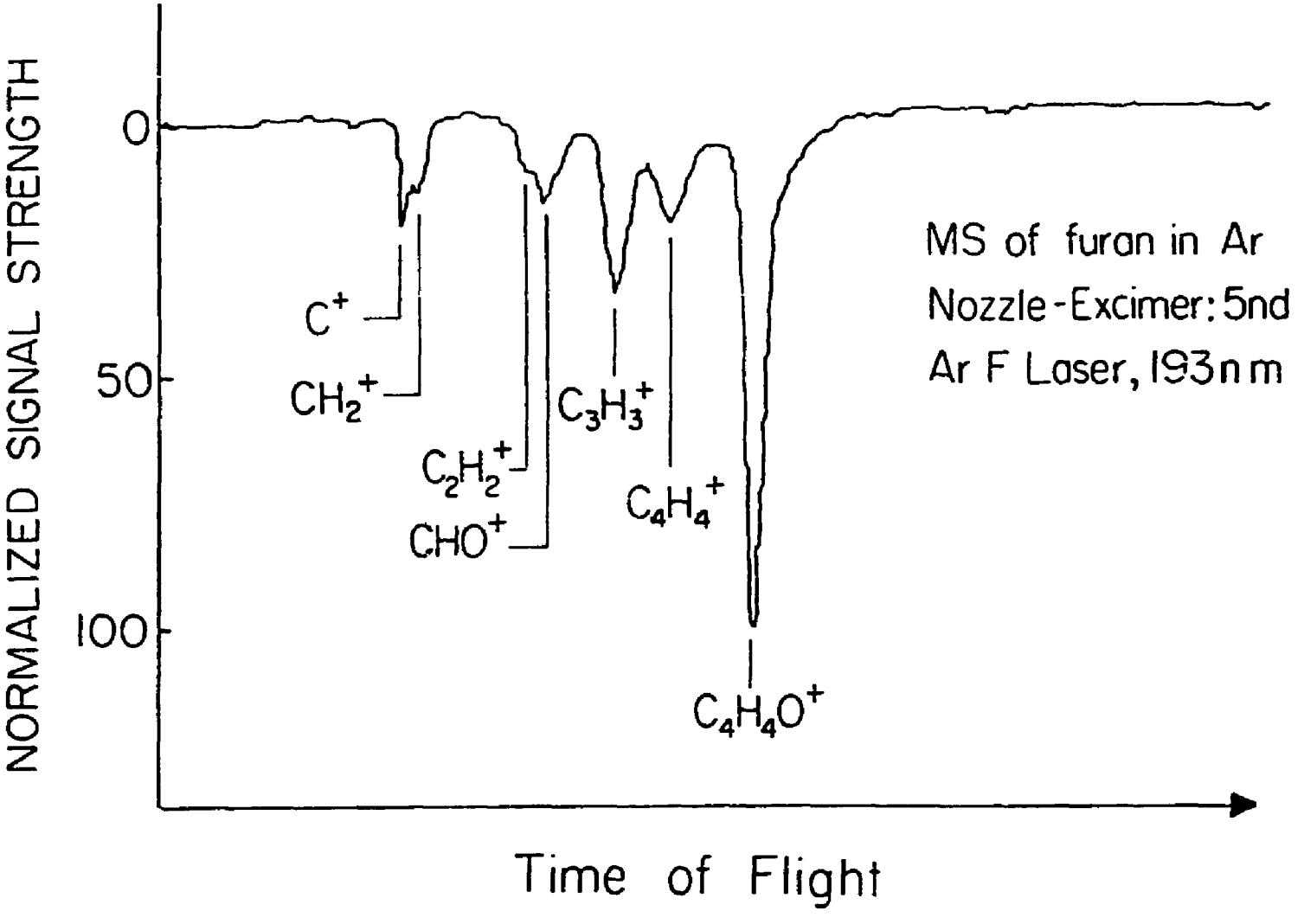

FIGURE 16. TIME-OF-FLIGHT MASS SPECTRUM OF THE ION PRODUCTS RESULTING FROM THE PHOTOLYSIS OF FURAN

furan to the $\tilde{B}$ state of the ion is 4.16 eV above the ionic ground state which lies at 8.90 eV. This disagrees from our origin by 1.09 eV and obviously indicates that the vertical and adiabatic ionization potentials are not the same in this instance. However, in the same paper, Eland reports a value of 12.66 eV for the $\tilde{B}$ state adiabatic ionization potential as well. This is 3.76 eV above the ground state of the cation and is also in disagreement with our findings and by a surprisingly large amount. In fact, it lies 0.69 eV (i.e., 5565 cm^{-1}!) higher than our origin. Derrick et al.[53] report 13.0, 12.6, and 8.87 eV for the ionization potentials discussed above, which are very similar to Eland's results. In addition, theoretical calculations on the photoelectron spectrum of furan disagree even more widely with the term value that we have obtained. Two MS-SCF-$X\alpha$ calculations of Alti et al.[59] predicted values of 13.73 and 15.37 eV for the third ionization potential of furan (i.e., the $\tilde{B}$ state of the cation). Further, ab initio Koopman's theorem calculations reported in the same paper predict a similar result of 14.74 eV. Using the values of 8.22, 9.10, and 9.06 eV, calculated for the first ionization potential of furan, these theoretical results are found to be in error by 2.44, 3.20, and 2.61 eV, respectively. These huge discrepancies indicate the need for further theoretical investigation into the nature of this important ion.

Due to the large differences between our results and those previously reported, we felt it necessary to perform a separate photoelectron spectroscopic study of furan to confirm our assignment. Subsequent spectra obtained on an effusive source at the National Synchnotron Light Source (NSLS) at Brookhaven National Laboratory[60] indicate the presence of a small pedestal on the low frequency side of the previously reported large structures beginning near 13 eV. This is illustrated in Figure 17. Closer inspection

FIGURE 17. PHOTOELECTRON SPECTRUM OF FURAN

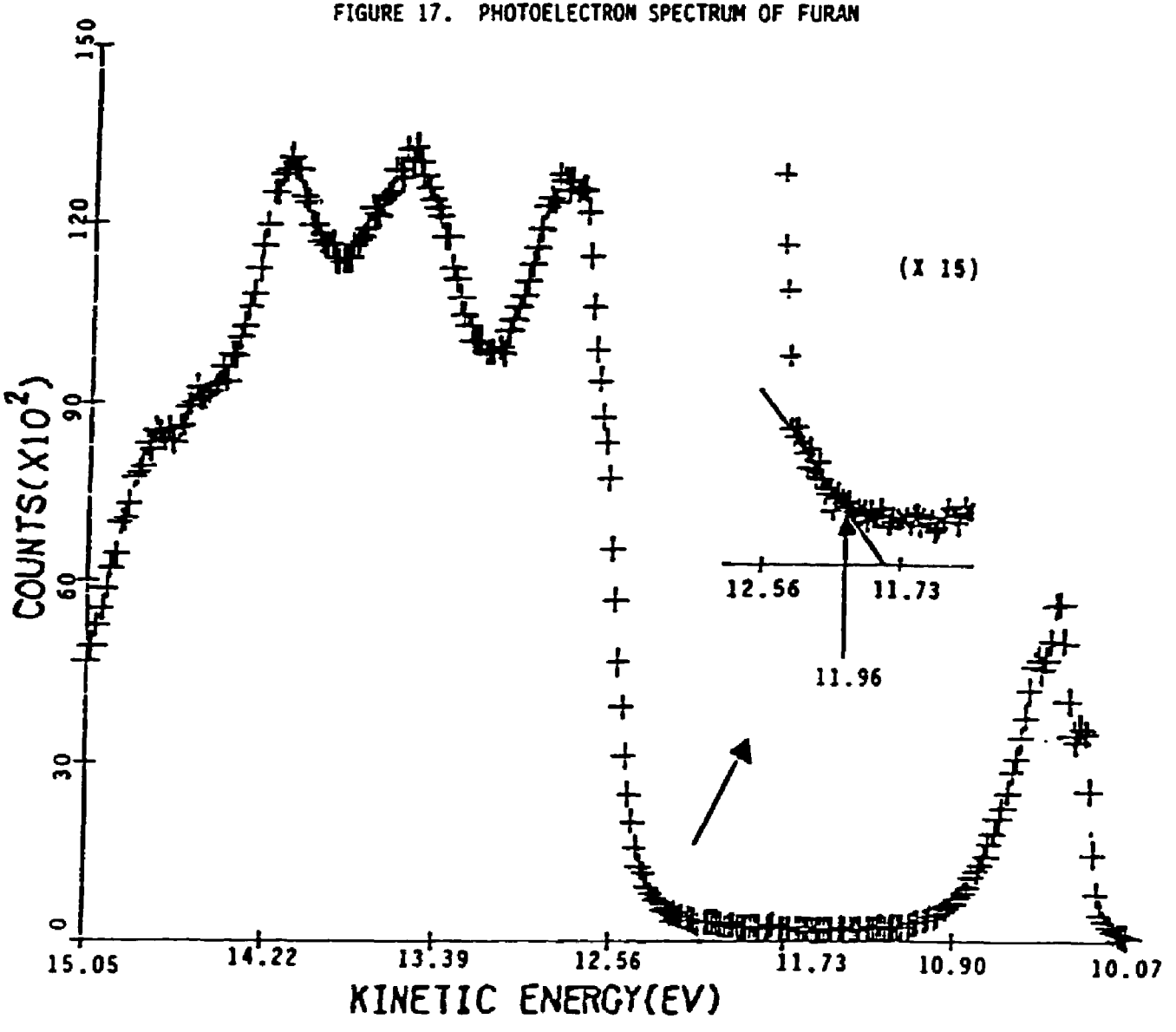

reveals that this pedestal begins at ~ 3.07 eV above the ground state of the ion. This corresponds exactly with our result. Therefore we are confident in our assignment of the electronic origin. The $\tilde{B}$ and higher electronic states of the furan cation appear as a very broad peak in the photoelectron spectrum of furan. In comparison to the $\tilde{X}$ and $\tilde{A}$ states, this peak is relatively structureless, lacking any well-resolved vibrational structure. These factors would lead one to believe that the potential curves for the $\tilde{X}$ and $\tilde{B}$ states are quite dissimilar and that the Franc-Condon overlap between their vibrationless levels might not be large. Therefore, as seems to be evident in this instance, the results of photoelectron spectra could be misleading in determining an accurate value for the origin of this electronic transition, since the adiabatic and vertical ionization potentials would not be the same. In this case, the photoelectron spectrum would show much stronger signals for vertical transitions to higher vibrational levels and the peaks would be slewed toward the high frequency side of the true origin, making ν_{00} difficult to identify. In addition, our studies of the wavelength resolved emission of the prompt fluorescence, i.e., the emission resulting from the photolysis/photoionization process, do in fact indicate that the Franc-Condon overlap for the ν_{00} transition is small. Peaks are observed for frequencies up to 31,450 cm^{-1}, corresponding to the upper limit of the amount of excitation energy that the absorption of two 193 nm photons (2 x 6.4 eV = 12.8 eV) can provide to the furan cation in excess of the first ionization limit of its parent molecule (8.9 eV). Inspection of the spectra clearly reveals that the signal strengths recorded near the origin are markedly weaker than those observed for higher vibrational levels. Further, the intensities present in the LIF excitation spectra are spread over a large frequency region and also illustrate the same general intensity pattern as discussed above.

This is in complete agreement with our expectations and is consistent with the intensity distributions reported in the photoelectron spectrum of furan for the $\tilde{B}$ state of the cation. The fact that we observe the ν_{00} transition, while early photoelectron spectroscopists did not, illustrates the increased sensitivity of our apparatus and the effects of probing "cold" ions.

5.3 VIBRATIONAL STRUCTURE

5.3.1 INTRODUCTION

In determining the nature of the observed vibrations of the furan cation, a number of resources have been found to be useful. First of all, it is beneficial to consider the vibrational frequencies of the parent molecule, since for some states they may be quite similar to those of the cation. This has been established for molecules possessing aromatic character[61], such as furan, and is possibly due to the fact that the ionized electron is strongly delocalized. Therefore knowledge of a vibrational frequency in the neutral molecule can be of assistance in identifying that vibration in the cation. Secondly, analysis of vibrational data on Rydberg states of furan obtained from multiphoton ionization is directly applicable. This is true because the vibrational frequencies present in excited Rydberg states of furan, lying close to the first ionization threshold, are converging onto those of the ground state of the furan cation. And thirdly, vibrational data obtained from photoelectron spectroscopy should be approximately correct although the resolution is quite low.

5.3.2 GROUND STATE VIBRATIONAL FREQUENCIES OF THE FURAN MOLECULE

The frequencies observed in the ground state of the furan molecule show great similarities to those identified in the laser excited wavelength resolved emission (WRE) spectra of the furan cation. Thompson and Temple[48], Bak et al.[49], Pickett[44,45], and Rico et al.[47] have obtained infrared and Raman spectra of furan and their assignments are presented in Table 3. The furan molecule and cation both have C_{2v} symmetry and possess 21 normal modes of vibration. These can be classified according to their symmetry properties, as is also presented in Table 3.

5.3.3 GROUND STATE VIBRATIONAL FREQUENCIES OF THE FURAN CATION

5.3.3.1 WRE SPECTRA OF THE FURAN CATION AND COMPARISON TO THE FURAN MOLECULE

Wavelength resolved emission (WRE) spectra for excitation at 24675, 25038, 25440, 25525, 25759, 25861, 26340, and 27441 cm^{-1} are presented in Figures 18, 19 and 20. The excitation frequencies correspond to all the fundamentals that we have assigned in the excited electronic state. A summary of the results, including frequencies (ν), displacements from the excitation frequency ($\Delta\nu$), and relative intensities, is presented in Tables 4 and 5. The ground state frequencies occurring in different spectra are quite similar. Average values are computed for the eight spectra and presented in Table 6 along with probable assignments. (Note: All standard deviations are well within the experimental resolution of the monochromator.) The peak at 1285

TABLE 3. IR AND RAMAN SPECTROSCOPY OF THE GROUND STATE OF THE FURAN MOLECULE

Class	Thompson and Temple[22]	Bak et al.[23]	Pickett[6]	Rico et al.[9]
A_1	724	720	725	871
	994	995		995
	1067	1067	1073	1066
	1137	1140	1189	1140
	1381	1384	1387	1384
	1486	1490	1490	1491
	(3090)	3124		3140
	(3120)	3124		3167
			1264	
A_2		550		613
		660		728
		1030		863
B_1	872	874	624	603
		1181	999?	1180
	1270	1268		1267
		1460		1040
	1579	1586	1580	1556
	(3090)	3163		3129
	(3120)	3163		3161
B_2	605	601		603
	744	744	763	745
	837	838	872	838

Symmetry Elements				# of Vibrations Expected					
	E	C_{2z}	σ_y	σ_x	Ring	C-H Bend	C-H Stretch	Total	IR	Raman
A_1	+	+	+	+	4	2	2	8	active	active
A_2	+	+	-	-	1	2		3	inactive	active
B_1	+	-	+	-	3	2	2	7	active	active
B_2	+	-	-	+	1	2		3	active	active

FIGURE 18. WRE SPECTRA FOR EXCITATION AT 24675, 25038, and 25440 CM-1

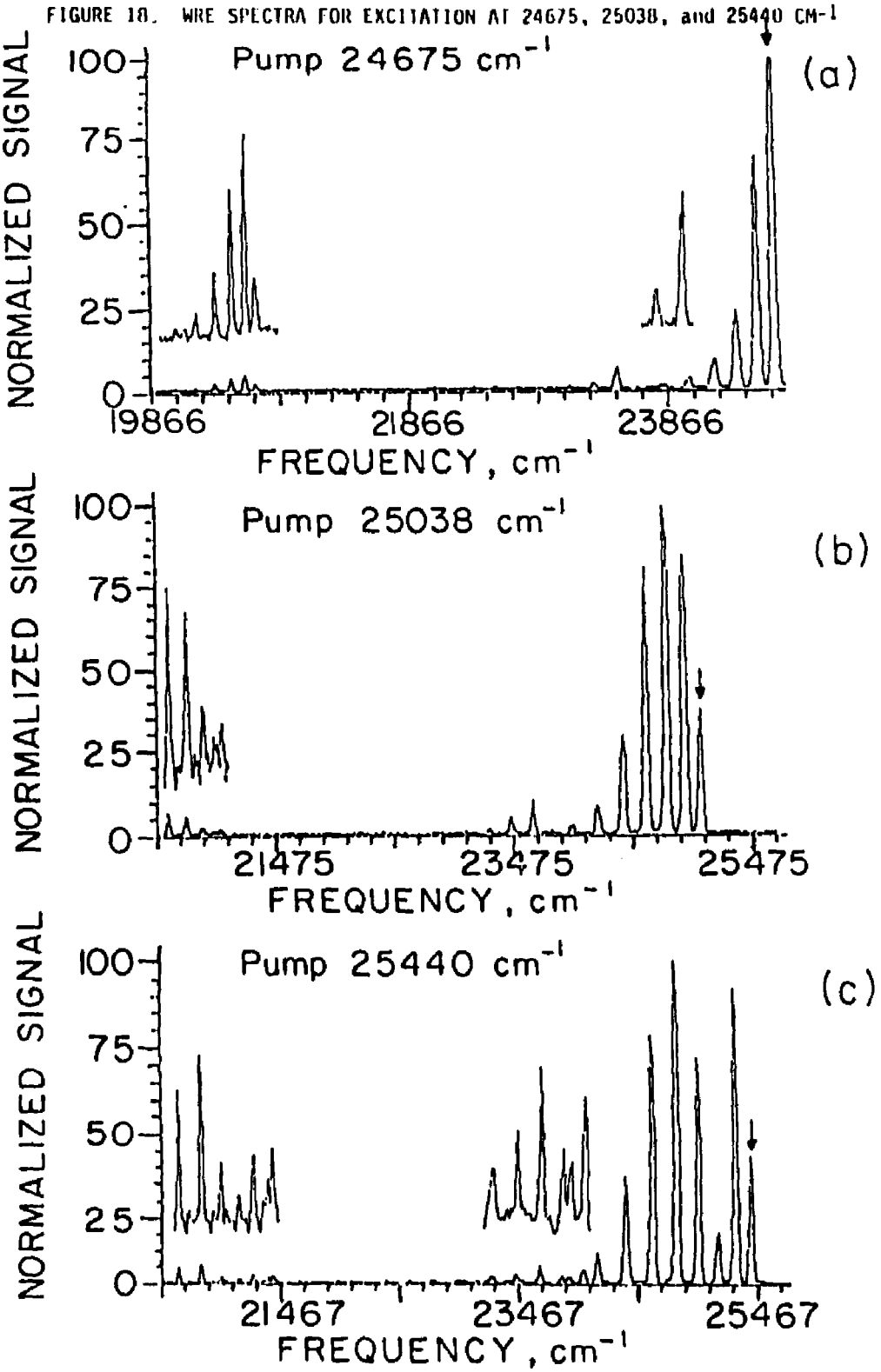

FIGURE 19. WRE SPECTRA FOR EXCITATION AT 25525, 25759, AND 25861 CM-1

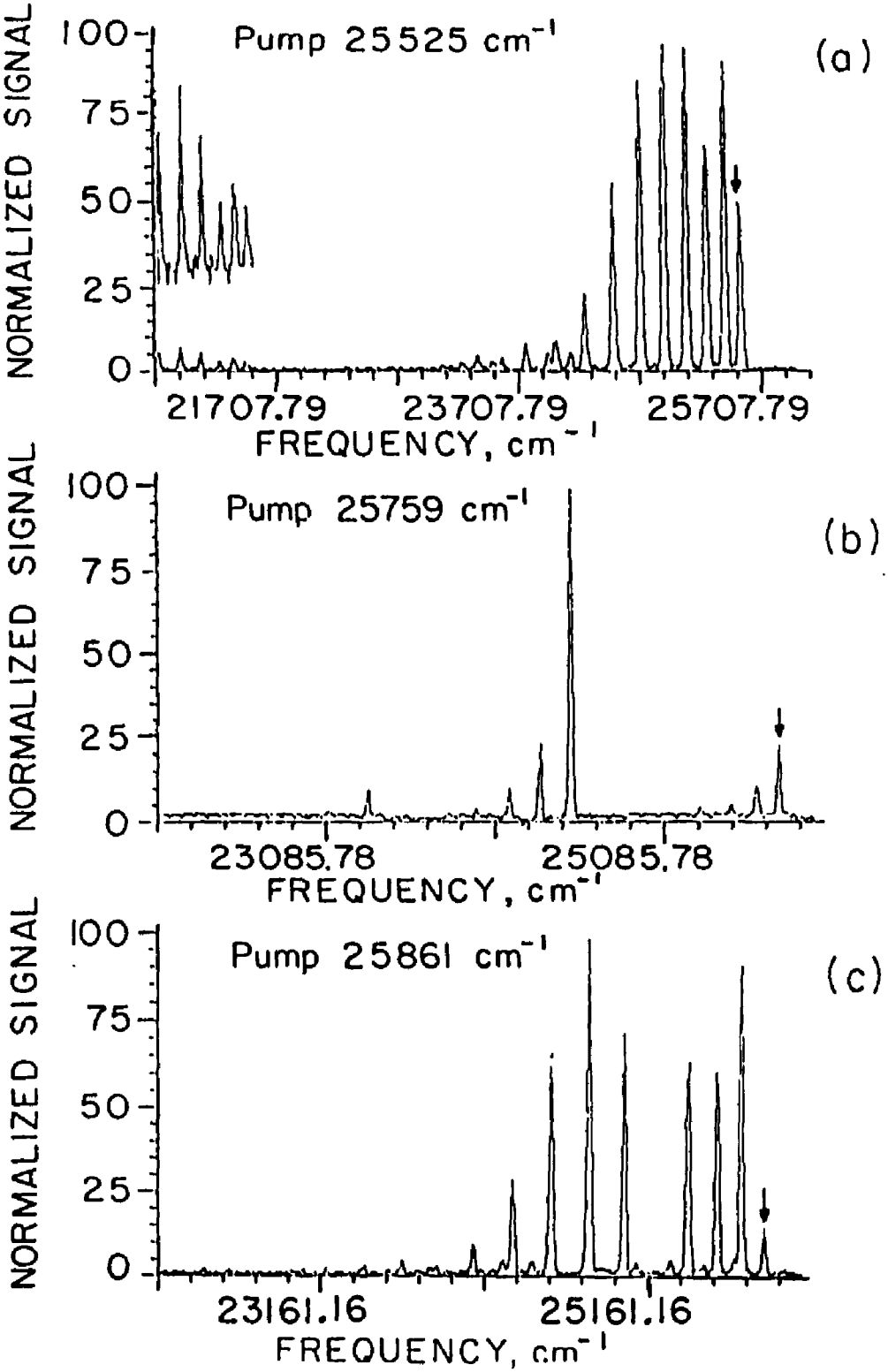

FIGURE 20. WRE SPECTRA FOR EXCITATION AT 26340, 26340, AND 27441 CM^{-1}

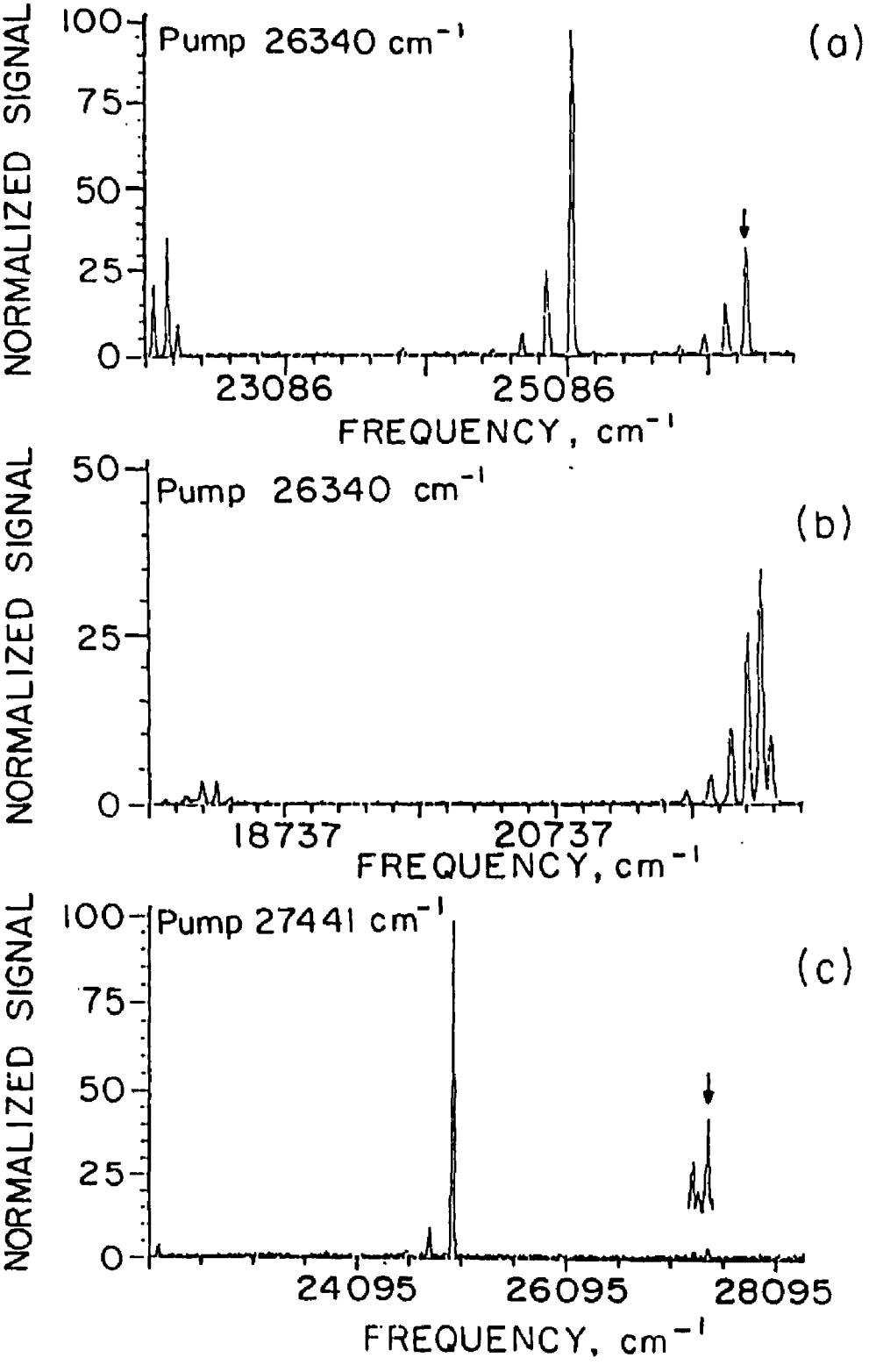

TABLE 4. WRE DATA FOR EXCITATION AT 24675, 25038, 25440, AND 25525 CM^{-1}

ν (cm^{-1})	$\Delta\nu$ (cm^{-1})	Relative Intensity	ν (cm^{-1})	$\Delta\nu$ (cm^{-1})	Relative Intensity
(1) 24 675 cm^{-1} excitation			(2) 25 038 cm^{-1} excitation		
24 675	0	100	25 038	0	36
24 542	133	61	24 907	131	95
24 380	295	23	24 753	285	100
24 203	472	9	24 589	449	77
24 011	664	3	24 391	647	28
23 823	852	2	24 184	854	9
23 614	1061	1	23 958	1080	3
23 454	1221	6	23 636	1402	10
23 247	1428	1	23 458	1580	3
23 091	1584	1	23 273	1765	3
21 107	3568	1	21 022	4016	3
20 654	4021	2	20 965	4073	2
20 577	4098	4	20 864	4174	3
20 476	4199	3	20 717	4321	6
20 347	4328	2	20 564	4474	7
20 191	4484	1	20 392	4646	3
20 106	4569	0.2	20 218	4820	2
20 041	4634	0.4			
(3) 25 440 cm^{-1} excitation			(4) 25 525 cm^{-1} excitation		
25 440	0	38	25 525	0	48
25 305	135	87	25 395	130	89
25 159	281	15	25 248	277	64
24 990	450	67	25 077	448	94
24 804	636	100	24 896	629	100
24 603	837	73	24 699	826	83
24 393	1047	33	24 475	1050	54
24 152	1288	9	24 244	1281	22
24 031	1409	4	24 121	1404	5
23 916	1524	2	23 999	1526	8
23 848	1592	3	23 942	1583	5
23 667	1773	5	23 760	1765	8
23 473	1967	3	23 547	1978	3
23 256	2184	2	23 486	2039	2
21 431	4009	3	23 354	2171	4
21 367	4073	2	23 164	2361	2
21 267	4173	1	21 441	4084	2
21 137	4303	1	21 340	4185	3
20 991	4449	2	21 218	4307	2
20 825	4615	6	21 066	4459	5
20 632	4808	5	20 903	4622	6
			20 717	4808	5

TABLE 5. WRE DATA FOR EXCITATION AT 25759, 25861, 26340, AND 27441 CM^{-1}

ν (cm^{-1})	$\Delta\nu$ (cm^{-1})	Relative Intensity	ν (cm^{-1})	$\Delta\nu$ (cm^{-1})	Relative Intensity
(5) 25 759 cm^{-1} excitation			(6) 25 861 cm^{-1} excitation		
25 759	0	19	25 861	0	12
25 634	125	8	25 728	133	83
25 477	282	3	25 577	284	55
25 296	463	3	25 396	465	57
24 533	1226	100	25 008	853	65
24 348	1411	20	24 797	1064	100
24 171	1588	8	24 565	1296	60
23 980	1779	2	24 457	1404	3
23 331	2428	7	24 332	1529	26
23 094	2665	2	24 273	1588	4
22 128	3631	1	24 092	1769	8
21 738	4021	1	23 868	1993	2
21 658	4101	2	23 828	2033	2
21 546	4213	2	23 648	2213	4
21 421	4338	1	23 415	2446	2
20 495	5264	11	23 193	2668	1
20 390	5369	5	23 048	2813	1
20 266	5493	3	22 433	3428	1
20 123	5636	1			
(7) 26 340 cm^{-1} excitation			(8) 27 441 cm^{-1} excitation		
26 340	0	30	27 441	0	2
26 202	138	14	27 306	135	1
26 045	295	6	25 005	2436	100
25 870	470	2	24 780	2661	8
25 690	650	1	24 557	2884	1
25 111	1229	100	22 172	5269	3
24 940	1400	24			
24 755	1585	6			
24 542	1798	1			
23 902	2438	2			
22 308	4032	9			
22 233	4107	34			
22 135	4205	20			
22 008	4332	10			
21 859	4481	4			
21 688	4652	2			
21 500	4840	1			
18 321	8019	1			
18 224	8116	3			
18 115	8225	3			
18 004	8336	1			

TABLE 6. VIBRATIONAL ASSIGNMENTS FOR THE GROUND STATE OF THE FURAN CATION

$\bar{\nu}$ (cm^{-1})	Assignment	$\bar{\nu}$ (cm^{-1})	Assignment
133	ν_1	2433	$2\nu_7$ or ν_{14}
287	ν_2	2667	$\nu_{12}+\nu_4$ or ν_{13}
459	ν_3	4022	$2\nu_{12}$ or $2\nu_7+\nu_{10}$
644	ν_4	4088	$\nu_{14}+\nu_9$
846	ν_5	4191	$\nu_{14}+\nu_7+\nu_2$
1068	ν_6	4323	$\nu_{14}+\nu_7+\nu_2+\nu_1$
1225	ν_7	4473	$\nu_{14}+\nu_7+2\nu_2$
1285	$2\nu_4$	4635	$\nu_{14}+\nu_7+\nu_2+\nu_3$
1409	ν_9	4823	$\nu_{14}+\nu_7+\nu_2+\nu_4$
1525	$\nu_7+\nu_2$	5017	$\nu_{14}+\nu_7+\nu_2+\nu_1+\nu_5$
1585	ν_{10}	5247	$\nu_{14}+\nu_7+\nu_2+\nu_1+\nu_6$
1776	ν_{11}	5464	$\nu_{14}+2\nu_7+\nu_2+\nu_1$
1982	$\nu_7+\nu_2+\nu_3$	5662	$\nu_{14}+\nu_7+\nu_2+\nu_1+\nu_5+\nu_4$
2034	$\nu_{10}+\nu_3$ or ν_{12}	8019	$4\nu_{14}$ or $4\nu_7+2\nu_{10}$
2192	$\nu_{12}+\nu_1$ or ν_{13}		

cm^{-1} probably corresponds to the class B_1, C-H deformation previously reported at 1270 cm^{-1} in the furan molecule. Guthrie et al.[62] have suggested that this is the first overtone of an A_2 fundamental lying at ~ 640 cm^{-1}. Our data indicates that this peak is indeed a first overtone but rather of a totally symmetric A_1 fundamental lying at 644 cm^{-1}. There is little doubt that our peak at 1068 cm^{-1} corresponds to the class A_1, C-H deformation lying at 1067 cm^{-1} in the molecule. The mode we list at 1225 cm^{-1} probably corresponds to the class A_1, C-H deformation assigned as 1137 cm^{-1} in furan. This fundamental is located at 1237 cm^{-1} in pyrrole, which has a similar geometry to furan[48]. The class A_1, ring mode reported at 1381 cm^{-1} quite likely corresponds to the peak we report at 1409 cm^{-1}. However, it should be noted that this band can also be explained as a combination of other frequencies as well. There is excellent correspondence between our peak at 1585 cm^{-1} and the B_1, ring mode assigned to 1579 cm^{-1} in the molecule. However, this would imply that the previous assignment was in error as to the symmetry class of the mode since it would appear necessary that it be A_1. Again, it should be noted that this peak is also explainable in terms of a combination band. Our peak at 846 cm^{-1} agrees well with the B_2, C-H deformation lying at 846 cm^{-1} in the molecule, but may also be the totally symmetric ring mode reported at 994 cm^{-1}. In addition, the peak at 644 cm^{-1} may correspond to the class A_1, ring mode at 724 cm^{-1} in the parent molecule. Pickett[44] reports observing a weak band at 465 cm^{-1} but does not assign it. This agrees well with the peak that we observe at 459 cm^{-1}. In addition, either Thompson and Temple[48], Pickett[44,45], or both, report bands at 1995, 2040, 2200, 2445, 2680, 4060, 4185, 4360, 4486, and 5032 cm^{-1}. All of these agree quite well with the results listed in Tables 4 and 5 for the present study.

Our results agreed so well with the furan molecule, that we felt it

necessary to confirm that we were not in fact observing the triplet system of the molecule. Flicker, Mosher, and Kuppermann[63] report that the first triplet state of furan lies 3.99 eV above the singlet ground state. This agrees qualitatively with the calculations of Solony, Birss, and Greenshields[64] and Sallavanti and Fitts[65] which predict this state to lie at 4.17 and 4.33 eV, respectively. In addition, it does not differ appreciably from the location of the first triplet level in benzene, i.e., 3.95 eV[66]. In order to visualize how "bottlenecking" into the triplet system could occur, one would have to assume that the furan molecule absorbs only one 193 nm photon, which corresponds to 6.4 eV. This is true because the first ionization potential of the furan molecule lies at 8.89 eV, and consequently the absorption of more than one 6.4 eV photon would lead to ionization. The molecule would then have to be in an excited singlet state which either collisionally deactivates or internally couples to a nearby triplet level. Assuming that the molecule absorbs only one 6.4 eV photon, the excited triplet level should be located at approximately 6.4 eV above the ground singlet state. It would then also lie approximately 2.4 eV above the ground triplet state. If bottlenecking into the triplet system were occurring in this manner, it should be possible to observe the triplet fluorescence in the photolysis/photoionization region. Subsequent wavelength resolved emission spectra show no evidence for transitions lying near 19,356 cm^{-1}, i.e., 2.4 eV, other than C_2 fragment fluorescence. However, there is abundant evidence for transitions in the 24,000 - 28,000 cm^{-1} region with peaks corresponding precisely to the LIF frequencies reported in this paper. This indicates that we are in fact probing the same electronic transition that is being excited by the photolysis laser. Since it is energetically impossible for this spectrum to arise from triplet system emission following the absorption of one 193 nm photon, we

conclude that this evidence, coupled with the arguments presented earlier in this section, indicate that the carrier of our spectrum is the furan cation and not the furan molecule.

5.3.3.2 COMPARISON TO PHOTOELECTRON AND MULTIPHOTON IONIZATION SPECTRA OF FURAN

In Table 7, we present the results of Derrick et al.[53] for photoelectron spectroscopic investigations of furan, in which vibrational frequencies were reported for the ground state of the cation which lies at 8.9 eV, the low-lying first excited state of the cation at 10.3 eV, and a very high-lying excited state at 17.3 eV. In addition, we have included the results of Cooper et al.[42] for the multiphoton ionization of furan, in which vibrational frequencies are reported for a number of high-lying Rydberg series in the molecule. In cases where two similar frequencies are reported for the same level, averages were computed to yield the values presented in the table. Cooper et al.[42] are the only investigators we have found who report a peak corresponding to the 133 cm^{-1} mode that we consistently observe in the ground state of the furan cation. They report a peak at 140 cm^{-1}. In addition, there is good agreement between the vibrations that they observe at 457, 625, 854, 1089, and 1400 cm^{-1}, and the ones we report at 459, 644, 846, 1067, and 1409 cm^{-1}. In comparison to the photoelectron spectra, all three frequencies reported for the ground state of the furan cation, i.e., 839, 1073, and 1420 cm^{-1}, are quite similar to those we report at 846, 1067, and 1409 cm^{-1}. According to the assignments of Derrick[53], these are all class A_1 vibrations. The first and last are ring modes. The second is also

TABLE 7. PHOTOELECTRON AND MULTIPHOTON IONIZATION SPECTROSCOPY OF FURAN

Photoelectron Spectroscopy			Multiphoton Ionization				
8.9 eV (cm^{-1})	10.3 eV (cm^{-1})	17.3 eV (cm^{-1})	R(ns) (cm^{-1})	R(np) (cm^{-1})	R(nd) (cm^{-1})	R(nf) (cm^{-1})	54509 cm^{-1} (cm^{-1})
				140			
				432			457
				537			625
				784	798		
839	871		859		854	866	862
	952			960			
1073		1024	1093	1051	1088	1093	1104
	1355		1400		1392	1421	
1420				1452	1441	1440	
		~2900					

tentatively designated as a ring mode, but this disagrees with our earlier assignment of the vibration as a C-H deformation. The earlier result was based on excellent agreement with the ground state frequency of 1067 cm^{-1} in the furan molecule and is believed to be correct.

5.3.3.3 DISCUSSION OF LOW FREQUENCY VIBRATIONS

The large number of vibrational levels in the ground state of the ion with energies less than 1000 cm^{-1} above the vibrationless level is consistent with the observation of Cooper et al.[42] on the Rydberg state of the neutral. However, few if any of these vibrational levels were observed by Pickett[44] in the VUV absorption spectrum of furan. The neutral molecule does not possess any vibrational fundamental frequencies lower than 550 cm^{-1} and the observation of these apparently low frequency modes in the ion needs to be explained. One possible explanation is that we are observing transitions to levels correlating with vibrations of B_2 symmetry in the neutral molecule. These vibronically couple the ground $^2A_2$ and first excited $^2B_1$ electronic states via a pseudo Jahn-Teller interaction resulting in a lowering of the vibrational frequency in the ground state and a highly anharmonic series of vibrational spacings. The transitions to some of them would be allowed since the total (vibronic) symmetry would be correct. (Note: A band at 450 cm^{-1} is seen weakly in UV absorption by Pickett[44].)

Thus far, all bands unexplainable in terms of combination bands have been discussed except those lying at 287 and 1776 cm^{-1}. The first lies 154 cm^{-1} above the peak at 133 cm^{-1} and is therefore unlikely to be a second harmonic of this. Hence, it is probably a fundamental vibration as well and may be

explainable in terms of the mechanism discussed above. The latter peak may be a class A_1 fundamental itself or perhaps a second harmonic of an asymmetric mode lying near 888 cm^{-1}. Thompson and Temple[48] report such a vibration in the neutral molecule at 872 cm^{-1} as a class B_1, C-H deformation.

5.3.4 EXCITED $\tilde{B}$ STATE VIBRATIONS OF THE FURAN CATION

5.3.4.1 EXCITATION SPECTRUM

An excitation spectrum for the $\tilde{B} \rightarrow \tilde{X}$ of the furan cation is presented in Figure 15. A list of frequencies and assignments is given in Table 8. Fundamentals lying at 363, 766(792), 849(810), 1084, and 1186 cm^{-1} are identified. Further, modes at 1665 and 2765 cm^{-1} are tentatively proposed. Identification of these fundamentals was based on the observation of higher harmonics and combinations of these frequencies. In addition, comparison of wavelength resolved emission (WRE) spectra for different members of a progression show marked similarities in their relative intensities and vibrational frequencies. While progressions in the fundamental frequencies, 766 and 849 cm^{-1}, are clearly identifiable, they appear to be shifted due to a possible Fermi resonance interaction. Therefore, we have presented a second value in parentheses for each of these, which corresponds to averaging the first two harmonics of each vibration. No harmonics of the 363 cm^{-1} mode have been observed, but it is seen in combination with other frequencies. The peak at 25,861 cm^{-1} was first thought to be a combination of 363 cm^{-1} with the 25,525 cm^{-1} peak, since no higher harmonics could be found. However, it actually lies 336 cm^{-1} away from this line and, based on this discrepancy, we

TABLE 8. LIF EXCITATION DATA FOR THE $\tilde{B}$ ELECTRONIC STATE OF THE FURAN CATION

ν (cm^{-1})	$\Delta\nu$ (cm^{-1})	Assignment	ν (cm^{-1})	$\Delta\nu$ (cm^{-1})	Assignment
24 537	-138	Hot Band	27 340	2665	$2\nu_2+\nu_4$
24 675	0	Origin	27 379	2704	$2\nu_3+\nu_4$
25 038	363	ν_1	27 441	2766	ν_j or $2\nu_j'$
25 440	765	ν_2	27 617	2941	$2\nu_4+\nu_2$
25 525	849	ν_3	27 701	3026	$2\nu_2+\nu_4+\nu_1$
25 759	1084	ν_4	27 759	3084	$4\nu_2$
25 861	1186	ν_5	27 807	3132	$\nu_7+\nu_1$
26 123	1448	$\nu_4+\nu_1$	27 890	3214	$4\nu_3$
26 259	1584	$2\nu_2$ or ν_8	27 924	3249	$2\nu_6$ or $3\nu_4$
26 295	1619	$2\nu_3$	28 100	3425	$3\nu_2+\nu_4$
26 340	1665	ν_6	28 215	3540	$\nu_7+\nu_2$
26 529	1854	$\nu_2+\nu_4$	28 286	3611	$2\nu_6+\nu_1$
26 612	1936	$\nu_3+\nu_4$	28 490	3815	$5\nu_2$
26 694	2019	$\nu_6+\nu_1$	28 634	3959	$4\nu_3+\nu_2$
26 840	2165	$2\nu_4$	28 693	4018	$2\nu_6+\nu_2$
26 948	2273	$\nu_5+\nu_4$	28 786	4111	$2\nu_2+2\nu_4+\nu_1$
27 017	2342	$3\nu_2$	28 828	4153	$4\nu_2+\nu_4$
27 086	2411	$3\nu_3$	29 174	4499	$3\nu_2+2\nu_4$
27 169	2494	$\nu_6+\nu_3$	29 213	4538	$6\nu_2$
27 208	2533	$2\nu_4+\nu_1$			

have tentatively assigned it as a fundamental mode lying at 1186 cm^{-1}. This would correlate well with the ground state mode at 1225 cm^{-1}. The structure of the relative intensity pattern and the vibrational frequencies in the WRE spectra for excitation at 25,759 cm^{-1} are strikingly different from that of most others, and hence this "signature" made the identification of the 1084 cm^{-1} mode and its higher harmonics quite easy. This assignment accounts for all observed WRE spectra of this type except one. The peak at 26,340 cm^{-1} has this structure as well and is not a combination band involving the 1084 cm^{-1} mode. Therefore we have tentatively assigned it as a fundamental at 1665 cm^{-1}. Its second harmonic coincides with the third harmonic of the 1084 cm^{-1} mode at the 27,924 cm^{-1} peak. However, closer inspection of this peak shows clear evidence that it is composed of more than one peak. The absence of a Fermi resonance at this point is an indication that the two vibrations have different symmetry. This would fit nicely, since the 1665 cm^{-1} mode is also explainable in terms of a second harmonic of an asymmetric vibration lying at 833 cm^{-1}. Rico et al.[47] report a B_2 ground state fundamental in the furan molecule lying at 838 cm^{-1}. One further assignment is based on WRE spectra obtained for excitation at 27,441 cm^{-1}. As illustrated in Figure 20, it has the same structure as is characteristic of the 1084 cm^{-1} mode. Nonetheless, the first strong peak in the WRE spectrum occurs at 2436 cm^{-1} rather than 1225 cm^{-1}. In addition, combinations of 363 and 766 cm^{-1} with this line are clearly identifiable. These assignments were confirmed by the WRE spectra corresponding to excitation at these frequencies, which showed similar relative intensity patterns and vibrational frequencies to the WRE spectrum for excitation at 27,441 cm^{-1}. Therefore, we have tentatively assigned this peak as a fundamental lying at 2765 cm^{-1}. However, it may actually be the second harmonic of an asymmetric vibration lying at 1383 cm^{-1}. Thompson and

Temple[48], Bak et al.[49], Pickett[44], and Rico et al.[47] report a vibration in the ground state of furan that corresponds precisely with this. They have assigned it as a totally symmetric A_1 vibration. In comparison, it is interesting to note that Derrick et al.[53] observe peaks at 1355 and 1400 cm^{-1} for the 10.3 eV and 17.3 eV states of the cation, respectively, in the photoelectron spectrum of furan. Cooper et al.[42] observe a peak at 1392 cm^{-1} in the R(np) Rydberg series of furan as well, and we observe a ground state vibration at 1409 cm^{-1} in the furan cation.

5.3.4.2 ELECTRONIC STATE SYMMETRIES

We have reported the symmetry of the $\tilde{B}$ state of the furan cation to be $^2B_2$. This is consistent with the calculations of Clark[67] but disasgrees with the results of Derrick et al.[54] and Alti et al.[59], who claim it to be $^2A_1$. All three calculations agree that the $\tilde{X}$ state has $^2A_2$ symmetry. If the $\tilde{B}$ state had $^2A_1$ character, electric dipole transitions between it and the $^2A_2$ ground state would be electronically forbidden. If our assignment of the $\tilde{B} \rightarrow \tilde{X}$ transition of $C_4H_4O^+$ is correct, then we require the upper state to have $^2B_2$ character, since our results show that the electronic transition is allowed. Further, despite extensive efforts to observe signals from the $\tilde{B} \rightarrow \tilde{A}$ transition in the laser excited, wavelength resolved emission from the $\tilde{B}$ state, none were found, indicating that this transition is forbidden. This is consistent with the expected $^2B_1$ symmetry of the $\tilde{A}$ state of the ion.[54,59,67]

5.4 COMPARISON TO THE GROUND STATE VIBRATIONAL STRUCTURE OF C_5H_5

The cyclopentadienyl radical (C_5H_5) is isoelectronic with the furan cation ($C_4H_4O^+$), and consequently the structures of the two species are expected to be related. In this section, the vibrational information obtained for the furan cation in this work is compared to data previously published for the cyclopentadienyl radical. In addition, comparison is also made to a wavelength resolved emission spectrum for C_5H_5 that was recently recorded in our own laboratory.

Due to its symmetrical D_{5h} geometry, the ground state of the cyclopentadienyl radical is electronically degenerate and thus according to the Jahn-Teller theorem[28] it will distort to a lower symmetry in order to remove this degeneracy. The vibrations corresponding to the Jahn-Teller active modes then become allowed and the resulting energy levels are highly anharmonic. To date, approximately 200 vibrational bands have been observed for C_5H_5[68] and yet no extensive progressions have been found. Therefore a complete understanding of the electronic and vibrational spectrum appears to necessitate the inclusion of the Jahn-Teller splitting in the $^2E_1''$ ground state.

Recently, Nelson et al.[69] reported laser induced fluoresence and wavelength resolved emission spectra for the gas phase cyclopentadienyl radical. This was accomplished by using a flashlamp pumped dye laser to probe C_5H_5 molecules produced by UV photolysis of cyclopentadiene (C_5H_6) at room temperature (300K) in a four-way cross glass photolysis cell. A summary of the emission data recorded for laser excitation at 338.0, 337.3, 334.3, 329.1, 326.6, and 325.6 nm is presented in Table 9. 338.0 nm corresponds to the electronic origin of the $\tilde{A}\ ^2A_2'' \rightarrow \tilde{X}\ ^2E_1''$ transition in C_5H_5. The other

excitation wavelengths correspond to fundametal vibrational frequencies in the excited electronic state. Nelson et al.[69] could not obtain any satisfactory fit to the spectrum despite the application of various methods. This supported their expectation that multimode coupling between the various Jahn-Teller active vibrations is important in the cyclopentadienyl radical in a similar manner to that reported by Sears et al.[70] for $C_6H_3F_3^+$ and $C_6H_3Cl_3^+$. Hence, they concluded that a complete understanding of the observed spectra would require an in-depth calculation of the Jahn-Teller splittings including the effects of the above-mentioned interaction.

Recently we recorded a wavelength resolved emission spectrum for C_5H_5 in our own laboratory corresponding to excitation of the electronic origin at 338.0 nm (29585 cm^{-1}). This spectrum is presented in Figure 21. The data for this spectrum is presented in Table 9. A brief inspection reveals that our results essentially confirm those of Nelson et al.[69]. The intensities and vibrational frequencies that we observe are nearly identical to those reported previously. However, we do list a number of weak bands that Nelson does not report for excitation at 338.0 nm but does report for excitation at other wavelengths. This may indicate the effects of probing "cold" molecules in which there are large populations in the lowest vibrational levels of their ground electronic states. Hence, LIF excitation and WRE emission of the 0-0 vibrational transition is more easily detected in the free jet expansion as compared to the static gas environment.

A comparison of the ground state vibrational frequencies observed by our group and Nelson et al.[69] for C_5H_5 to those we have reported for the furan cation yields a picture of two very similar structures. The data we have obtained for C_5H_5 and $C_4H_4O^+$ is presented in Table 9 along with the results of Nelson. The vibrational frequencies for the furan cation are the same as

FIGURE 21. MRE SPECTRUM OF C_5H_5 FOR EXCITATION AT 29,586 CM^{-1}

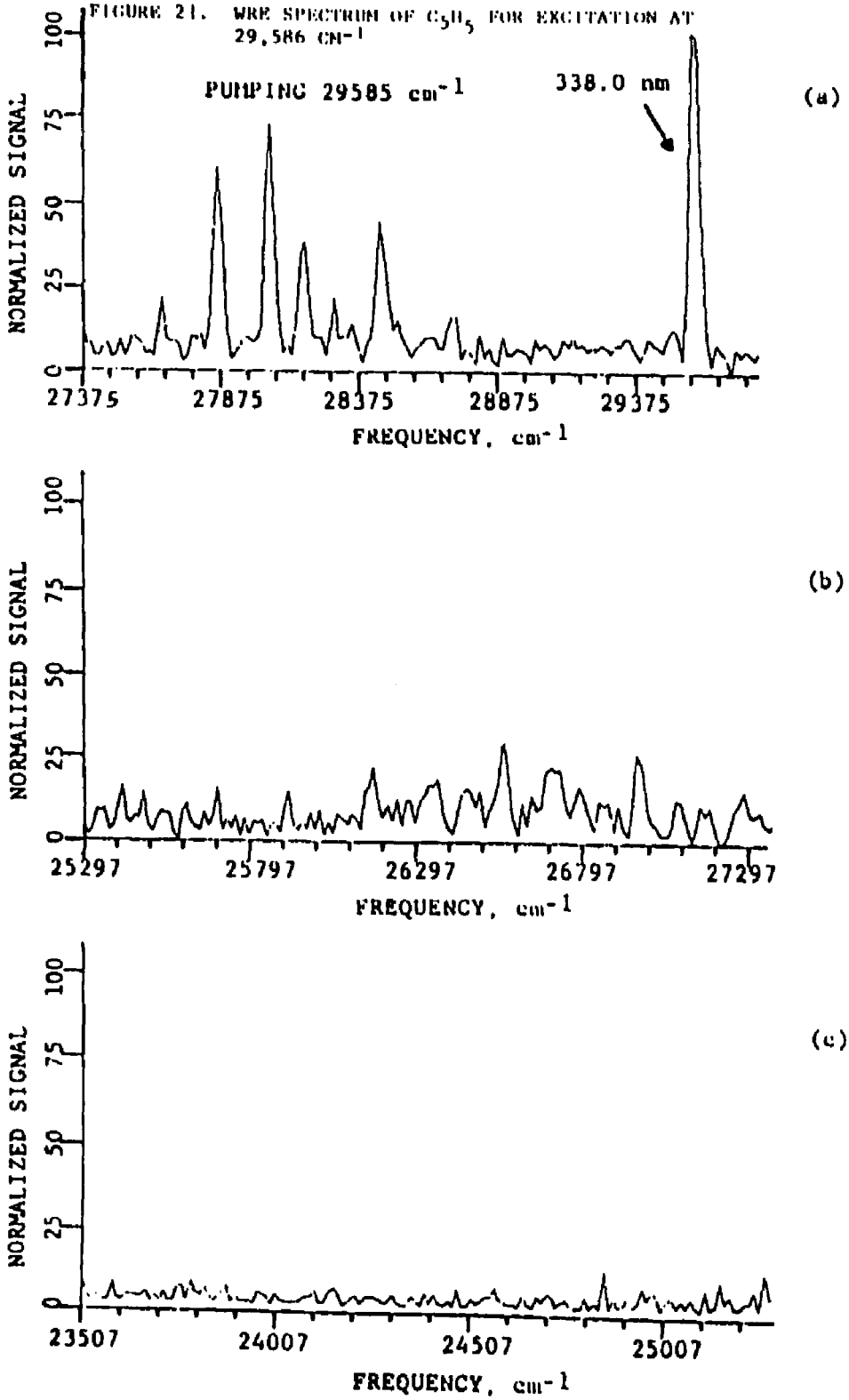

TABLE 9. COMPARISON OF WRE DATA FOR THE $C_4H_4O^+$ and C_5H_5

Nelson et al.						Our Group	
C_5H_5						C_5H_5	$C_4H_4O^+$
Excitation Wavelength (nm)							
338.0	337.3	334.3	329.1	326.6	325.6	338.0	Averages
----	166	----	----	----	----	----	133
----	287	----	----	----	----	----	287
----	382	----	----	----	----	----	----
----	----	432	477	475	----	----	459
----	----	----	----	----	----	----	644
883	----	877	874	----	----	880	846
----	----	----	----	953	995	970	----
----	----	----	1082	1085	----	1070	1068
1132	1149	1136	----	----	----	1141	----
----	----	----	----	1245	1257	1238	1225
1317	1326	1309	1311	1327	1352	1302	1285
1430	----	----	1429	1430	----	1414	1409
1527	1541	1520	1546	1552	1515	1540	1525
----	----	----	----	----	1608	1599	1585
1720	1721	1720	1753	1754	1726	1732	1776
----	1793	----	----	----	----	----	----
1945	1915	1987	1956	1973	----	1928	1982
2025	----	----	2020	2042	----	2028	2034
----	2106	2189	----	2156	2116	2130	2192
2228	----	2227	2204	2245	2262	2227	----
2318	2309	2311	2315	2333	----	2305	----
2434	2428	2417	2440	2480	2491	2425	2433
----	----	----	2549	2467	----	2516	----
2616	2685	2627	2627	2689	2675	2630	2667
2810	2858	2878	2795	2793	2876	2803	----
2882	2987	----	2909	2905	----	2874	----
3034	3072	3038	3051	3028	3078	3031	----
3129	3177	3124	----	----	----	3144	----
3258	3261	3260	3259	3246	3243	3248	----
----	----	3338	3340	3332	----	3320	----
3433	3406	3422	3456	3455	3441	3427	----
----	3625	3576	3572	----	3648	3681	----
----	3826	3755	3778	----	----	3894	----
----	----	3938	----	----	3995	3986	4022
----	----	4212	----	----	4154	4117	4191
----	----	4356	----	----	4361	4321	4323
----	----	4505	----	----	----	4435	4473
----	----	----	----	----	4605	4635	4635
----	----	----	----	----	4730	4735	4823
----	----	----	----	----	4958	----	5017

those listed in Table 6 and, again, represent average values obtained for excitation at a number of different wavelengths. It is interesting to note that practically all of the bands reported for the furan cation correspond well to some band in C_5H_5. The only exception to this is the band listed at 644 cm^{-1}. This correlation is surprisingly good and may prove to be of considerable importance in gaining further insight into the Jahn-Teller effect in C_5H_5. Hopefully, the pseudo Jahn-Teller effect that we suspect to be present in $C_4H_4O^+$ represents a more easily understood limiting case of the more severe Jahn-Teller distortion present in C_5H_5. Therefore a complete understanding of the interactions and the resulting vibrational structure present in the furan cation may render the corresponding effects and structures in the cyclopentadienyl radical more theoretically tractable.

5.5 ROTATIONAL STRUCTURE OF THE FURAN CATION

5.5.1 EXPECTATIONS

The ground state geometry of the furan cation, and hence the furan molecule as well, is presented in Figure 6. By inspection of the figure and consideration of the definition of the inertial moment (i.e., $I = \sum_i m_i r_i^2$, where the m_i are the atomic masses and the r_i are the perpendicular distances of the atoms from the rotational axis), one can infer that the inertial moment about the C_{2v} symmetry axis (I_A) would be approximately the same as that about an axis perpendicular to it and also in the molecular plane (I_B). Further, the inertial moment about an axis perpendicular to the molecular plane and through the center of the molecule

(I_C) would be larger than either I_A or I_B, since more of the atoms lie farther from that axis. Hence, for the furan cation, one has $I_A \approx I_B < I_C$. This is precisely the definition of a near oblate symmetric top rotor, which was given in section 3.2.3.1. With this in mind, we proceed to analyze the rotational-vibrational spectra of the furan cation in terms of a near oblate symmetric top model.

5.5.2 ROTATIONAL SPECTRA AND RESULTS

In Figure 22a, we present a high-resolution (0.1 cm^{-1}) laser induced fluorescence excitation spectrum of the origin of the $\tilde{B} \rightarrow \tilde{X}$ transition of the furan cation. Rotational assignments are listed above the figure. Figures 22b and 22c illustrate the same spectrum recorded at different argon carrier gas backing pressures. Since the spectrum in Figure 22a was recorded with the highest such pressure, it is rotationally the coldest. This is so because for higher backing pressures there are larger numbers of cooling collisions in the free jet expansion. Therefore the variation of the backing pressure is one method by which spectroscopists can exercise some control over the rotational temperature of the species formed in the free jet. This is quite useful for the rotational analysis, since it allows one to obtain very cold spectra in which only a few J values are present. These spectra can usually be understood fairly easily in terms of first-order rotational constants (i.e., A_e, B_e, C_e). Once these have been obtained, one can "heat up" the species rotationally by lowering the backing pressure and decreasing the number of cooling collisions and record more complicated spectra which can be used to understand higher order rotational interactions. A computer simulation of

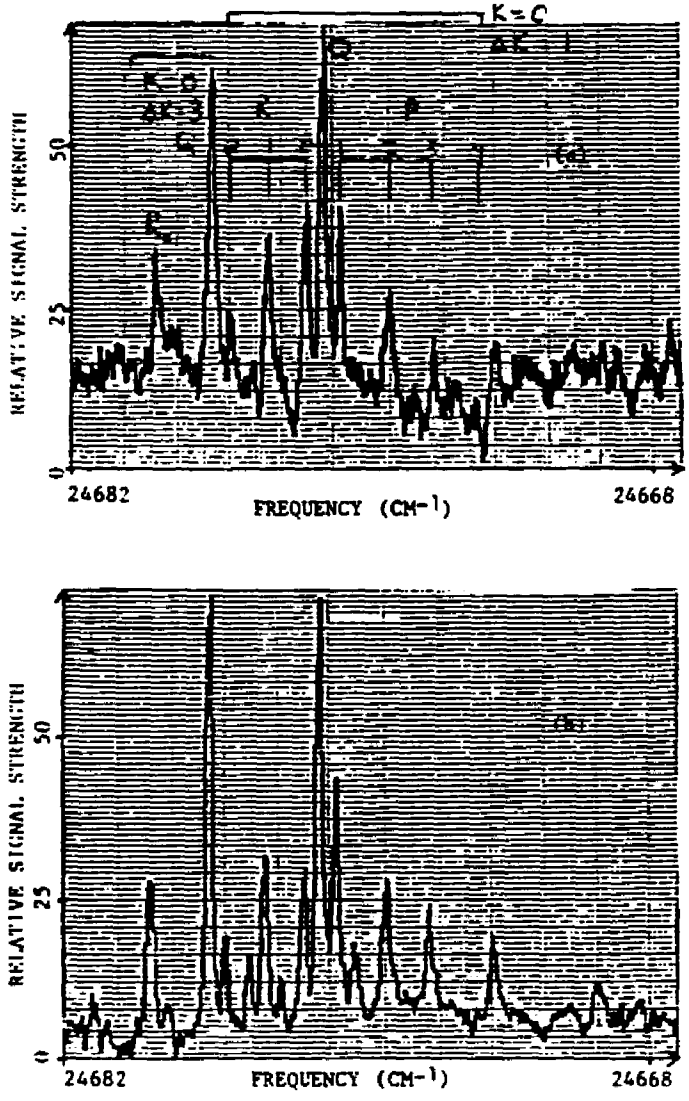

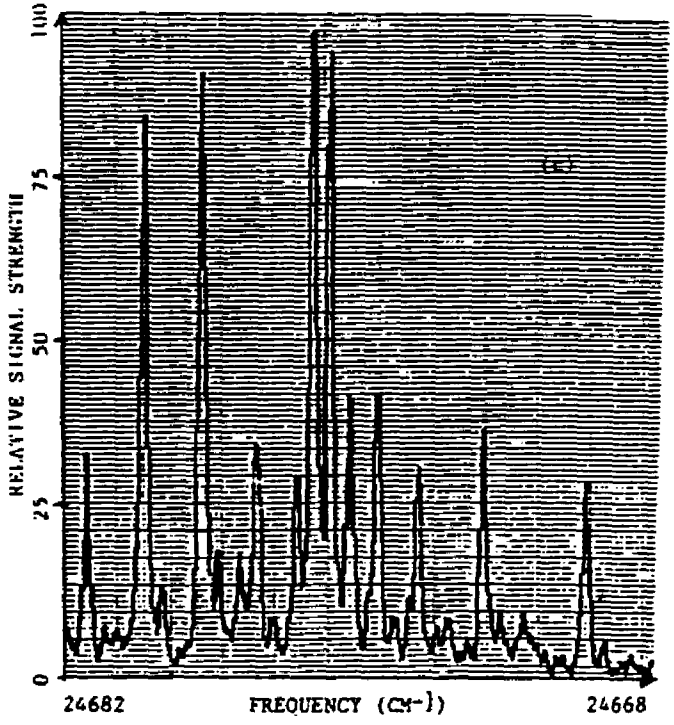

FIGURE 22. LIF ROTATIONAL SPECTRA OF THE ORIGIN OF THE ELECTRONIC TRANSITION AT VARIOUS BACKING PRESSURES
(a) 150 PSI
(b) 100 PSI
(c) 60 PSI

FIGURE 23. COMPUTER SIMULATION OF THE ROTATIONAL SPECTRUM IN FIGURE 22

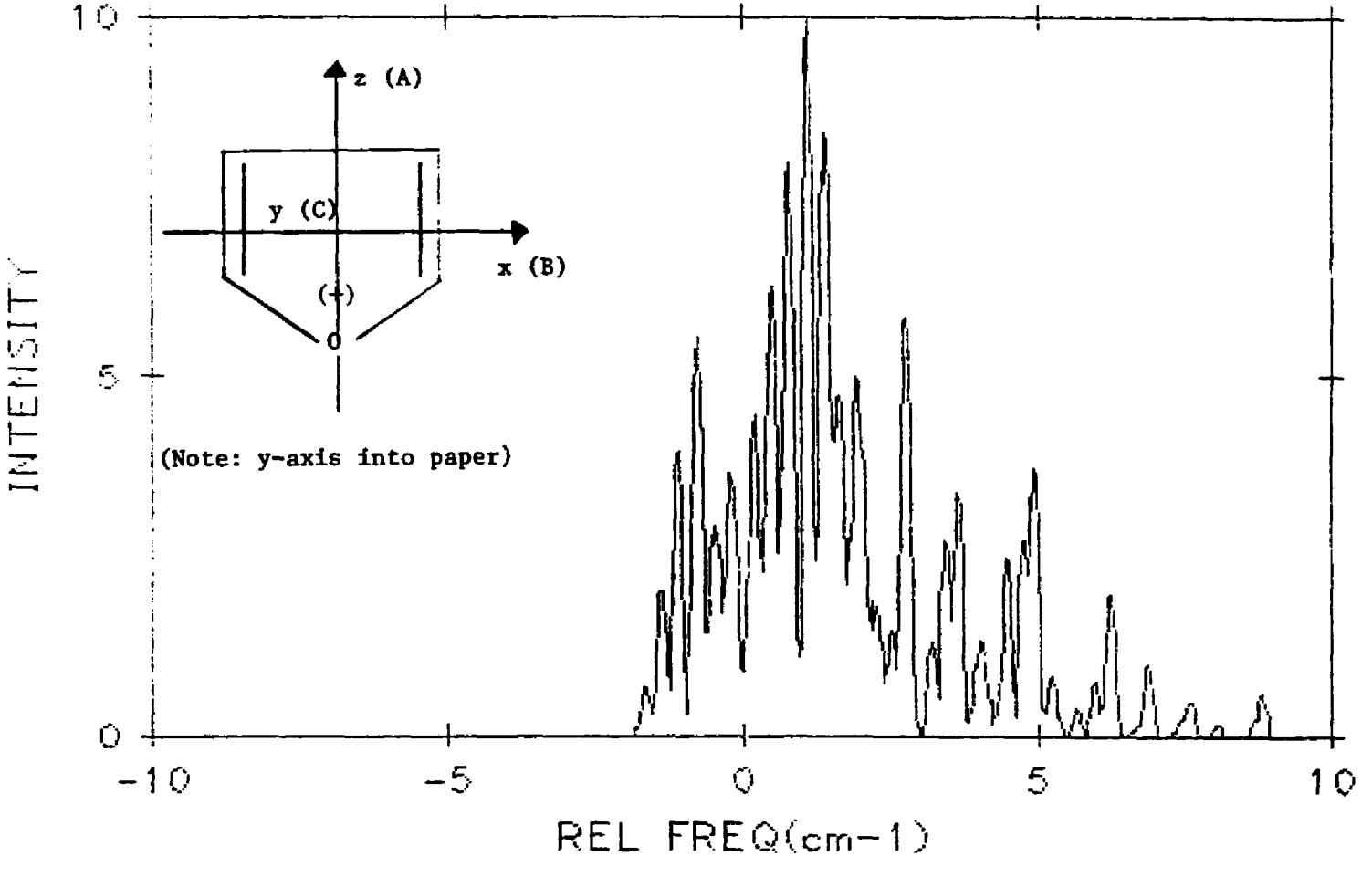

(Note: Frequency scale reversed as compared to Figure 22.)

Table 10. Comparison of the Rotational Constants of the Furan Cation and the Furan Molecule

	Furan Cation		Furan Molecule
Rotational Constants	$\tilde{X}$ State	$\tilde{B}$ State	$\tilde{X}$ State
A_ν (cm^{-1})	0.300	0.310	0.315
B_ν (cm^{-1})	0.290	0.300	0.308
C_ν (cm^{-1})	0.150	0.165	0.156
κ	0.867	0.862	0.912

the spectra presented in Figure 22 is illustrated in Figure 23 for a rotational temperature of 1.5 K. An insert in the figure pictures the rotational axes and coordinate system for the furan cation. Also, Table 10 lists the rotational constants for the furan cation and compares them to those of the furan molecule. A discussion of this data follows below.

The $\tilde{B} \rightarrow \tilde{X}$ electronic transition of the furan cation is a $B_2 \rightarrow A_2$ transition. The direct product of these two species indicates that the transition dipole in this instance belongs to the B_1 representation, i.e. T_x according to Table 1. Therefore, this system is a type B perpendicular band, since the transition dipole lies perpendicular to the top axis and along the B rotational axis. The rotational selection rules appropriate for the oblate top limit are $\Delta K_a = \pm 1$ and $\Delta K_c = \pm 1$, where K_a and K_c refer to the projections of the total angular momentum, $\tilde{J}$, along the C_{2v} axis (A) and oblate top axis (C). $\Delta K = 0$ would correspond to a parallel transition in which the transition dipole has a component along the top axis. Since that component is zero in this instance, transitions of this type are not allowed. As one gets farther from the oblate top limit, the relaxed selection rules $\Delta K_{a,c}$= odd become allowed for an asymmetric rotor. Therefore, one expects to see transitions with $\Delta K_{a,c} = \pm 1, \pm 3, \pm 5, \ldots$, as larger asymmetries are considered.

To determine the asymmetry of a molecule, one can calculate a quantity known as the "asymmetry parameter", given by

$$b = \frac{C_v - B_v}{2(A_v - 1/2(B_v + C_v))} \qquad (60)$$

where B_v and C_v are given by equation (46) and A_v can be inferred from the same equation. Using equation (60), one can construct the following parameter

$$\kappa = \frac{1 + 3b}{1 - b} \qquad (61)$$

which takes the value -1 for a prolate symmetric top and +1 for an oblate symmetric top (while b = 0 and -1, respectively, for these limiting cases). For the furan molecule, one calculates a κ value of 0.912 for the ground electronic state, indicating that it is in fact a near oblate symmetric top. However, the deviation of the κ value from +1 implies the presence of a substantial amount of asymmetry. For the furan cation, one obtains κ values of 0.867 and 0.862 for the $\tilde{X}$ and $\tilde{B}$ electronic states, respectively. Therefore, while this is also a near oblate symmetric top, the ion possesses an even larger amount of asymmetry than the neutral molecule. This asymmetry is illustrated by the presence of transitions in Figure 22 with $\Delta K = \pm 3$. These would not be allowed for a strictly symmetric top rotor.

The frequencies and relative intensities for the rotational transitions were calculated by setting up the matrix of the rotational hamiltonian operator, H_r, in a basis of symmetric top eigenfunctions and diagonalizing it. Neglecting additional perturbations and interactions, the rotational hamiltonian is given by equation (43) for E_k, where P_a, P_b, and P_c are replaced by their quantum mechanical operators. The diagonal elements of this matrix are the rotational energies, and the intensities are calculated from the matrix of the dipole moment operator between the eigenstates. This problem is complicated for the furan cation by two additional effects:
(1) Fine Structure- The unpaired electron spin is coupled to the angular momentum of the nuclear rotation ($\tilde{N}$). This coupling is represented by a spin-rotation term, H_{sr}, in the hamiltonian given by

$$H_{sr} = \varepsilon_{aa} N_a S_a + \varepsilon_{bb} N_b S_b + \varepsilon_{cc} N_c S_c \qquad (60)$$

where N_a, N_b, N_c are the components of the angular momentum of nuclear

rotation along the rotational axes; S_a, S_b, S_c are the components of the spin angular momentum along the rotational axes; and ε_{aa}, ε_{bb}, ε_{cc} are the spin-rotation constants which reflect the magnitude of the perturbation. (2)Spin Statistics- These affect the intensities of the transitions. Furan has four equivalent protons, meaning that they can be transformed into one another by the symmetry operations of the point group of the molecule. Only certain combinations of these spin eigenfunctions will transform according to the various species of the point group. Therefore, the different state symmetries will have different spin statistical weights for its rovibronic transitions in accordance with the particular combination of spin eigenfunctions that it possesses.

The calculation of the rotational structure as a type B perpendicular band was based on the assignment of the symmetry of the $\tilde{B}$ electronic state of the furan cation as B_2. The success of our analysis is further evidence that this is in fact the true species of this state and that the earlier calculations of Derrick et al.[54] and Alti et al.[59] in which the $\tilde{B}$ state was assigned as having A_1 symmetry were not correct.

5.6 IONIC CLUSTER STUDIES

During the course of our investigation into the structure of the furan cation, we attempted to form and study ionic clusters of argon and helium with the furan cation. For such species, one would expect the inert gas atom to be a small perturbation to the system, resulting in a spectrum essentially identical to that of the furan cation but red- or blue-shifted by a small frequency interval. However, in our case, no such spectra were found.

Nonetheless, we did observe evidence that clustering was occuring.

The photolysis for these studies was performed as a function of laser intensity, distance from the nozzle, and carrier gas backing pressure. The first quantity was varied in order to ascertain whether we were fragmenting the ionic clusters as soon as they were being formed. The second quantity was varied in order to investigate the possibility of two different formation mechanisms for the ionic clusters. Formation for photolysis close to the nozzle, where n-body ($n \geq 2$) collisions are occuring, would correspond to the following formation mechanism (illustrated here for an argon carrier gas):

$$(1)\quad C_4H_4O + 2h\nu(193\ nm) \rightarrow C_4H_4O^+$$

$$(2)\quad C_4H_4O^+ + Ar \rightarrow C_4H_4O^+\text{-}Ar$$

On the other hand, formation for photolysis farther from the nozzle, where the density of collisions is much lower and two-body collisions dominate, would correspond to the following process:

$$(1)\quad C_4H_4O + Ar \rightarrow C_4H_4O\text{-}Ar$$

$$(2)\quad C_4H_4O\text{-}Ar + 2h\nu(193\ nm) \rightarrow C_4H_4O^+\text{-}Ar$$

The third quantity was varied in order to see how carrier gas backing pressure affected the formation of ionic clusters. Based on simple intuition, one would expect that larger backing pressures would increase the number of collisions between furan cations and inert carrier gas atoms and thereby increase the number of ionic clusters formed.

For photolysis as a function of laser intensity, no new structures were observed. The intensities of the furan cation signals merely increased or decreased as the photolysis laser intensity was varied.

For photolysis as a function of distance from the nozzle, we did observe new structures growing into the furan cation spectrum as the nozzle-laser distance was increased. However, these were present in both helium and argon

carrier gases. Therefore, we concluded that they must be due to an increase in the number of fragments rather than the formation of ionic clusters. This is consistent with our time-of-flight mass spectroscopic analysis of the ion products of the photolysis, where we observed an increase in the yield of ionic fragments and a decrease in the yield of furan cations as the nozzle-photolysis laser distance was increased.

Finally, for photolysis as a function of carrier gas backing pressure, we again observed no new structures in the spectrum. However, as the pressure was increased, the furan cation signals decreased rapidly. For a 200 μm orifice, strong furan cation signals were observed at a backing pressure of 60 PSI in both helium and argon carrier gases. However, as that was increased, the signal decreased substantially in helium by 500 PSI and disappeared entirely in argon by 400 PSI. This depletion of the ion spectrum is a behavior that one would expect if clustering were occuring. Additionally, a more rapid depletion would be expected in argon since it is more polarizable than helium and, hence, clusters more readily. To extend the many-body collision region in the supersonic free jet expansion and thereby further encourage the formation of ionic clusters, we performed these same studies with a 400 μm orifice also. In helium, a similar behavior was observed but with an increased depletion of the ion signal occuring at lower backing pressures. Likewise, in argon, the ion signals disappeared at a lower backing pressure of 180 PSI with this larger orifice, rather than at 400 PSI as was observed with the smaller orifice. Although no ionic cluster spectra were found, these observations are consistent with the idea that clustering may be occurring in our source.

6. OPTICAL EMISSION STUDIES ON GRAPHITE IN A LASER/VAPORIZATION SUPERSONIC JET CLUSTER SOURCE

6.1 BACKGROUND

Plasmas formed by laser vaporization from a solid target in a supersonic free jet environment have been extensively used to study clustering of neutral and ionic species[9-12]. A large number of these studies have examined the relative abundances of the cluster sizes via mass spectroscopy. The inherent problems in interpreting these distributions have recently been the topic of much interest[10,71,72]. In this section the results of optical emission studies on this source using a graphite target are described in an attempt to elucidate the processes that are occurring in the initial stages of the expansion. Analysis of the spectra demonstrates that localized excitation of the species in the expansion is occurring at energies that exceed the thermal collisions. Observation of the C_2 Swan bands have been made at distances as large as 15 nozzle diameters (nd) from the orifice and at times as long as 6 μs after the laser pulse. This is consistent with the idea that excited C_2 molecules are being formed locally in the free jet by collision processes that can supply approximately 3 eV excitation energy. Evidence that supports low-energy electron collision processes via dissociative recombination and attachment is presented along with other mechanisms and the bearing of these results on the interpretation of cluster stability is discussed.

6.2 WRE SPECTRUM OF THE PLASMA EMISSION

Figure 24 shows a typical wavelength resolved emission spectrum produced by laser irradiation of a graphite target in a helium expansion. The spectrum was recorded with a 200 ns gate delayed 1.8 μs after the firing of the YAG laser pulse which vaporized the surface of the graphite rod. It was viewed at a distance of 3 nd (3 mm) downstream from the nozzle. The 532 nm YAG laser intensity was 350 MW/cm^2 and the helium backing pressure was 60 PSI. The emission spectra were recorded with various time delays, downstream positions, laser intensities, backing pressures, and carrier gases. What is clearly shown in Figure 24 is a well-resolved Swan band[73] ($d\ ^3\Pi_g \rightarrow a\ ^3\Pi_u$) emission spectrum of the C_2 molecule. There is also present a structureless continuous background that extends from 350 to 650 nm and peaks at 400 nm. The discrete band emission consists soley of C_2 Swan bands and, at higher intensities, C atom and ion emission.

6.3 CONTINUOUS LOCALIZED EXCITATION OF C_2 MOLECULES IN THE FREE JET EXPANSION

6.3.1 EVIDENCE FOR EXCITATION

The collision free lifetime of the 0-0 $d\ ^3\Pi_g \rightarrow a\ ^3\Pi_u$ transition was measured by Smith[74] to be 170 ns. However, the spectrum in Figure 24 was recorded 1.8 μs after the YAG laser excitation was finished, which immediately establishes the existence of continuous localized formation of excited C_2 molecules at this point in the free jet. The Swan band emission can originate from two general collision mechanisms: (1) direct excitation of C_2 molecules

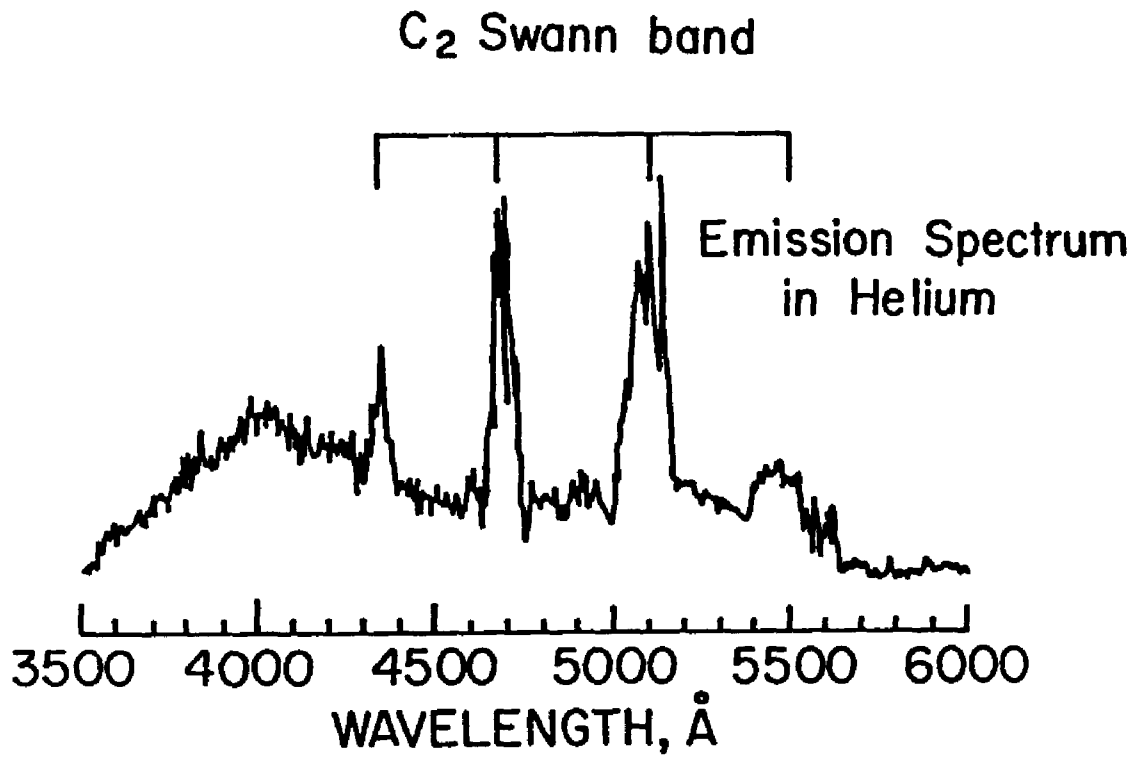

FIGURE 24. WAVELENGTH RESOLVED EMISSION SPECTRUM OF C_2 IN HELIUM

and/or (2) the formation of excited state C_2 molecules via dissociative or recombinative processes. The C_2 emission in the helium expansion was observed at distances of up to 15 nd from the orifice exit, or 20 nd from the graphite rod (i.e., the flow channel is 5 nd long), which corresponds to a time of 5 μs after the YAG laser pulse. The continuous emission persisted beyond the 15 nd region and extended as far as the Mach disk. At 10 nd similar observations were made with an argon carrier gas as shown in Figure 25, although there is an overall drop in the C_2 Swan band emission. In argon, the detection of the Swan band emission at 10 nd translates into a time of approximately 15 μs after the YAG laser pulse. The overall emission is observed to be insensitive to the carrier gas backing pressure over the range of 1 to 10 atmospheres.

6.3.2 EXCITATION MECHANISMS

6.3.2.1 GENERAL CONSIDERATIONS

The 15 nd limit of the Swan band emission can be interpreted as the need for n-body collisions, with $n \geq 3$, as a prerequisite for C_2 emission. For expansion conditions that are typical for a room-temperature source (300K) the n-body collision region is assumed to be finished within the first 5 nd[1]. However, considering the elevated temperatures of the graphite plasma source (the melting point of graphite is 3823 K) and the fact that the number of n-body collisions occurring in the jet is proportional to the square root of the local temperature[75], it is reasonable to assume that the n-body collision region extends to 15 nd. This is also consistent with our observation that

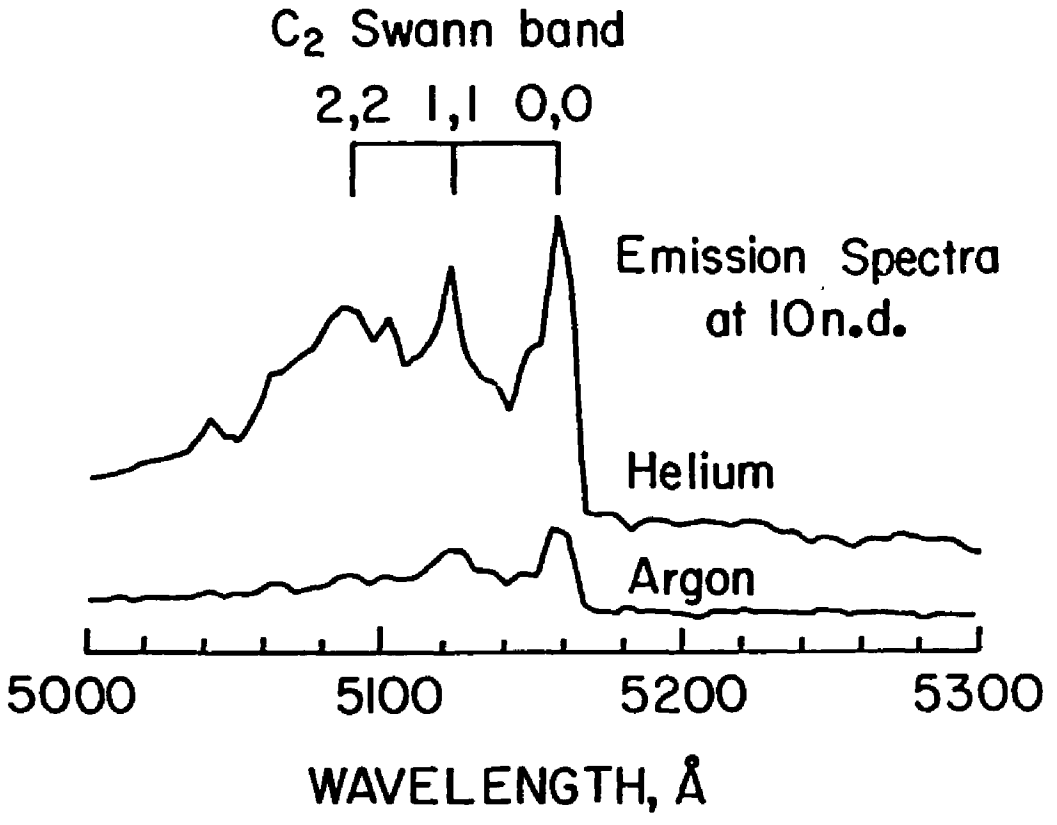

FIGURE 25. EMISSION SPECTRA IN ARGON AND HELIUM AT TEN NOZZLE DIAMETERS

the emission velocity distribution within the first few nozzle diameters is broadened and has arrival times faster than expected by thermalization. However, by 15 nd the emission distribution is significantly narrower (translationally) and approaching the bulk flow velocity.

6.3.2.2 HEAVY-BODY COLLISIONS

After the laser pulse has terminated and sufficient electron cooling has occurred, the molecules, atoms, and ions in excited states can only be created in heavy-body collisions of the second kind or through electron-ion or ion-ion recombination[76]. Certain heavy-body collisions were considered as possible mechanisms for producing excited states of the C_2 molecule at times much later than the YAG laser pulse. One such mechanism is Penning collisions with atomic or molecular metastable states. To determine the presence of helium metastable states we performed an LIF study on the strongly allowed $2\ ^3S \rightarrow 3\ ^3P$ transition of helium[77]. The output from a BBQ dye laser was focussed onto the expansion at a point downstream from the nozzle and the fluorescence was collected as a function of the dye laser wavelength. The LIF was detected through a monochromator which was fixed at the 388.9 nm transition of helium in order to reduce the background emission and thus enhance our sensitivity. No helium metastables were detected, although the experiment was repeated for various values of helium backing pressure, downstream position, and LIF excitation times with respect to the YAG laser pulse. Therefore, Penning collisions with metastable helium atoms can be excluded as a likely excitation mechanism for producing excited state C_2 molecules. Likewise, the exclusion of metastable argon atoms can also be

deduced. We also suspected that there might be large amounts of CO molecules in our source since various groups[12,78,79] have reported the formation of copious amounts of Ni, Fe, and Cu oxides using a similar laser/vaporization source. Consequently, we felt it necessary to determine if the metastable a $^3\Pi$ state of CO could be responsible for the Swan band emission. LIF detection of metastable CO molecules was accomplished by scanning a frequency-doubled Coumarin 540A dye laser over the a $^3\Pi \rightarrow$ b $^3\Sigma^+$ transition. No detectable amount of metastable CO was observed. The negligibility of metastable states produced by any impurities in the graphite rod was verified by using an annealed high-purity sample. This experiment rendered no observable change in the emission spectra. The species responsible for the continuous background emission was also considered as a possible candidate for metastable state excitation. Figure 26 shows a plot of the intensity dependence of both the C_2 and continuous emission. It is clear that the Swan band emission appears at a significantly higher rate than the continuous emission. Likewise, above a laser intensity of 575 MW/cm^2, there is a region where C_2 emission is observed even when no continuous emission is present. Therefore, it is possible to establish the role of Penning-type collisions as negligibly small.

6.3.2.3 ELECTRON COLLISION PROCESSES

By elimination of heavy-body collisions of the second kind, electron collision processes become very plausible mechanisms for the production of C_2 Swan band emission. At first glance, the most direct mechanism would be C_2 collisions with "hot" 3 eV electrons formed by the YAG laser vaporization.

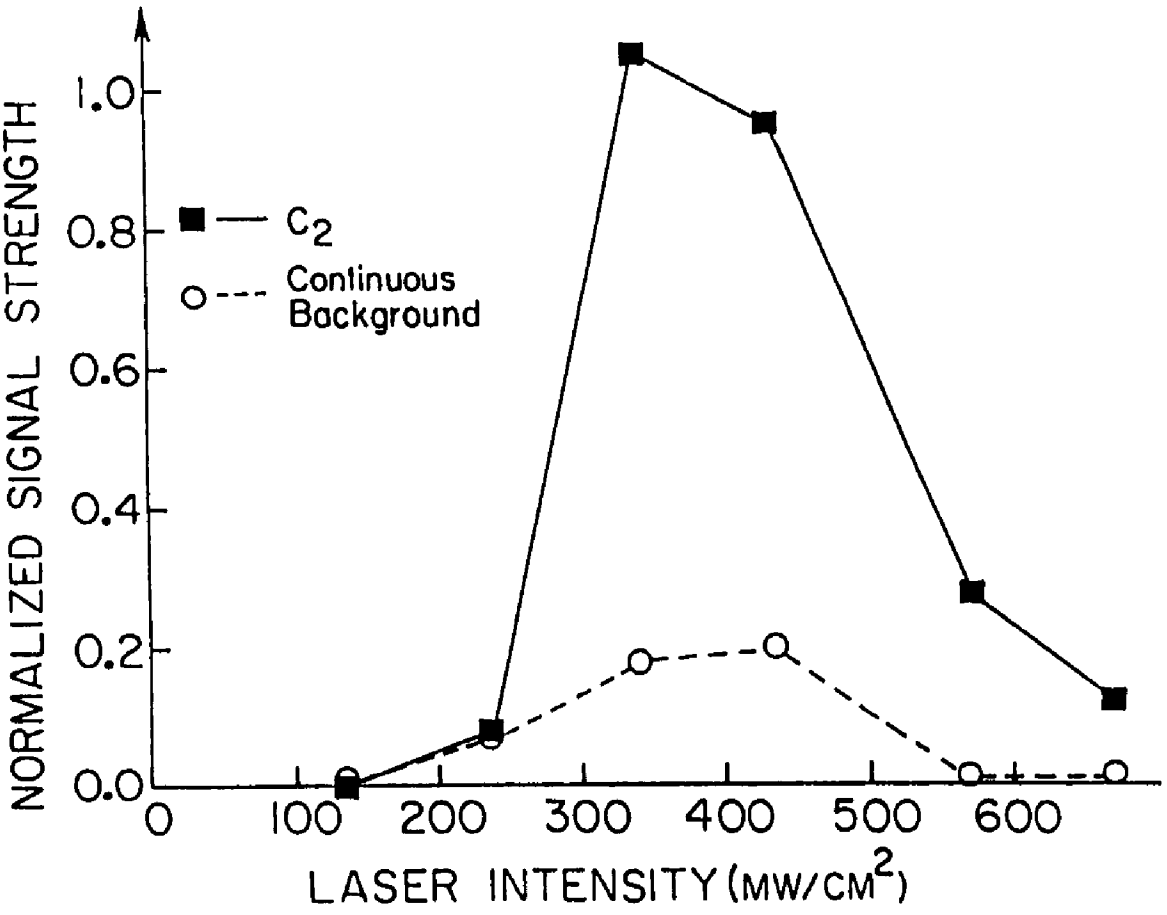

FIGURE 26. C_2 AND CONTINUOUS EMISSION AS A FUNCTION OF VAPORIZING LASER INTENSITY

However, by 0.5 μs after the YAG laser pulse sufficient electron cooling has occurred to reduce the electron energies to less than 0.5 eV[80]. This is quite consistent with the idea that the electron collision frequency is extremely high in both the nozzle throat and the n-body collision region of the expansion and that the absolute velocities of the C_2 molecules and the electrons must be nearly the same. Thus, direct "hot" electron impact appears to be very unlikely.

On the other hand, slow electron processes, principally electron recombination, are still highly probable mechanisms. Such processes as electron-molecule dissociative attachment[82], electron-ion and ion-ion recombination[76] must all be considered as plausible mechanisms. Various groups[10,11] doing mass spectroscopy on similar laser/vaporization graphite sources and under similar conditions have produced considerable evidence establishing the existence of abundant amounts of C_m, $m \geq 1$, cations and anions in our source. This coupled to the observation that Swan band emission occurs primarily in a region characterized by n-body processes would indicate a three-body process involving an electron. The third body, most probably a neutral inert carrier gas atom, would be responsible for removing excess energy into translational degrees of freedom. This hypothesis is supported by the spectra in Figure 25. Due to the larger size of argon as compared to helium, the number density of argon atoms in the jet is lower than for helium for similar backing pressures. This means that the probability of a three-body collision of the type described above is also lower. Consequently, the C_2 Swan band signals observed in argon should be less than those in helium, which is precisely what is observed.

The recombination (attachment) process can be viewed as low-energy electrons approaching along the ground state potential of the cation (neutral)

or, alternatively, as electrons approaching near threshold to the neutral (anion) molecule. Two specific mechanisms can be easily ruled out as unlikely. These are (1) C_2 cation-He neutral charge exchange and (2) atomic carbon cation and anion recombination. Mechanism (1) would require the addition of 15 eV of internal energy via a high-energy impact and therefore leads to an extremely small charge-exchange cross-section[81]. Mechanism (2) is eliminated based on the experimental observation, that as the laser intensity is increased above 1 GW/cm^2, the ions produced are predominantly atomic carbon[80], and therefore C_2 Swan band emission should not only be observable but most probably increased as well if this mechanism were responsible for the C_2 excitation. However, no Swan band emission is observed at these intensities, as is apparent from Figure 26. Finally, in considering various dissociative processes, dissociative attachment is not expected to be as probable a mechanism as dissociative recombination, provided equal numbers of ions and neutrals are present, since the electron affinity of an atom is much less than that of its corresponding ion. In fact, cross sections for the latter process have been known to be as much as three orders of magnitude larger in some cases[81]. However, in our source, neutrals are orders of magnitude more abundant than charged species, thereby making the yields for both processes comparable.

In view of the evidence presented in this section, we propose that the dominant mechanism for the production of C_2 Swan band emission is low-energy electron collisions with C_n cations ($n \geq 2$) and neutrals ($n > 2$) followed by dissociation, where one of the fragments is an excited C_2 molecule. Although the exact nature of the recombination and/or attachment is difficult to elucidate, we are confident that such processes are responsible for the emission in the initial stages of the supersonic expansion. In the particular

case of C_n cation recombination with an electron for n=2, energy conservation requires the removal of approximately 9 eV of translational energy by a third body, therefore making this an unfavorable process. However, as n increases, the probability for C_n dissociative recombinations which lead to the formation of excited state C_2 molecules increases due to the presence of additional fragmentation channels involving other carbon clusters. These fragments possess many internal degrees of freedom and provide a variety of channels by which to couple out excess energy from the system by means other than translational motion. This increases the number of pathways by which a given reaction can take place, hence making it more probable. In addition to electron recombination, dissociative recombination between C_n cations and anions is another plausible mechanism. Assuming that equal densities of C_n anions and electrons are present, the cross section for recombination with a C_n cation is expected to be similar for the two species. However, the density of electrons is expected to be orders of magnitude larger than the density of C_n anions[10,11,76], indicating that C_n recombination with an electron is a much more favorable process.

6.4 IMPLICATIONS OF THIS STUDY

In the preceeding section, we have demonstrated that localized formation of excited C_2 molecules in the n-body region of the free jet expansion is likely occurring via low-energy electron processes involving both C_n cations ($n \geq 2$) and neutrals ($n > 2$). Electron recombination with C_2 cations is considered to be energetically less favorable than with larger C_n cations. In addition, dissociative recombination between C_n cations and

anions is possible but far less probable than electron processes. The evidence supports the idea that the dominant collision mechanisms are dissociative recombination and dissociative attachment. The possible effects of these processes on both the neutral and charged cluster distributions that can be observed downstream from a laser/vaporization cluster source must be considered very carefully. This is especially true if such processes are found to be selective in their fragmentation channels, since this could indicate that certain "magic numbers", which were inferred from cluster distributions obtained with such a source, do not necessarily refect cluster stability but fragmentation preference instead. This idea reinforces the concerns and efforts of others[9-12,71], and further serves to indicate that cluster stability experiments should be performed on isolated mass selected beams in order to eliminate any ambiguity in interpreting the meaning of "magic numbers".

REFERENCES

1. T. A. Miller, Science. 223, 545 (1984).
2. D. H. Levy, Science. 214, 263 (1981).
3. D. H. Levy, Ann. Rev. Phys. Chem. 31, 197 (1980).
4. R. E. Smalley, L. Wharton, and D. H. Levy, Acc. Chem. Res. 10, 139 (1977).
5. D. H. Levy, L. Wharton, and R. E. Smalley, Chemical and Biochemical Applications of Lasers. C. B. Moore, Ed. (Academic Press, New York, 1977), Vol. 2, p. 1.
6. L. Wharton, D. Auerbach, D. H. Levy, and R. E. Smalley, Advances in Laser Chemistry. A. H. Zewail, Ed. (Springer-Verlag, New York, 1978), p. 408.
7. D. H. Levy, Photoselective Chemistry, Part 1. J. Jortner, Ed. (John Wiley and Sons, Inc., New York, 1981), p. 323.
8. D. H. Levy, Quantum Dynamics of Molecules. R. G. Wooley, Ed. (Plenum Publishing Corp., New York, 1980), p. 115.
9. L. A. Bloomfield, R. R. Freeman, and W. L. Brown, Phys. Rev. Lett. 54, 2246 (1985).
10. L. A. Bloomfield, M. E. Geusic, R. R. Freeman, and W. L. Brown, Chem. Phys. Lett. 121, 33 (1985).
11. D. E. Powers, S. G. Hansen, M. E. Geusic, D. L. Michalpoulas, and R. E. Smalley, J. Chem. Phys. 78, 2866 (1983).
12. E. A. Rohlfing, D. M. Cox, and A. Kaldor, J. Phys. Chem. 88, 4497 (1984).
13. A. Kantrowitz and J. Grey, Rev. Sci. Instrum. 22, 328 (1951).
14. G. B. Kistiakowsky and W. P. Slichter, Rev. Sci. Instrum. 22, 333 (1951).
15. E. W. Becker and K. Bier, Z. Naturforsch. Teil A. 9, 975 (1954).
16. H. Ashkenhas and F. S. Sherman, IVth Symposium on Rarefied Gas Dynamics. J. H. deLeeuw, Ed. (Academic Press, New York, 1966), Vol. II.

17. D. M. Lubman, C. T. Rettner, and R. N. Zare, J. Chem. Phys. 86, 1129 (1982).

18. J. B. Anderson and J. B. Fenn, Phys. Fluids. 8, 780 (1965).

19. D. R. Miller, J. P. Toennies, and K. Winkelmann, XIth Symposium on Rarefied Gas Dynamics. M. Becker and M. Friebig, Eds. (DFVLR Press, Yorz-Wahn, 1974).

20. R. Camparque, A. Lebehot, J. C. Lemonnier, D. Marette, and J. Pebay, Abstracts of the Vth Symposium International sur Jets Molecularres. Nice, 1975.

21. J. P. Toennies and K. Winkelmann, J. Chem. Phys. 66, 3965 (1977).

22. W. A. Guillory, Introduction to Molecular Structure and Spectroscopy. (Allyn and Bacon, Inc., Boston, 1977).

23. G. Herzberg, Molecular Spectra and Molecular Structure: Spectra of Diatomic Molecules. (Van Nostrand Reinhold Company, New York, 1966).

24. G. Herzberg, Molecular Spectra and Molecular Structure: Infrared and Raman Spectra of Polyatomic Molecules. (Van Nostrand Reinhold Company,New York, 1966).

25. G. Herzberg, Molecular Spectra and Molecular Structure: Electronic Spectra and Electronic Structure of Polyatomic Molecules. (Van Nostrand Reinhold Company, New York, 1966).

26. M. Born and R. Oppenheimer, Ann. Physik. 84, 457 (1927).

27. E. Fermi, Z. Physik. 71, 250 (1931).

28. H. A. Jahn and E. Teller, Proc. Roy. Soc. 161A, 220 (1937).

29. R. Campargue, Rev. Sci. Instrum. 35, 111 (1964).

30. R. Campargue, Ph.D. Thesis, Univ. Paris, France, 1970.

31. R. Campargue, J. Chem. Phys. 52, 1795 (1970).

32. T. G. Dietz, M. A. Duncan, D. E. Powers, and R. E. Smalley, J. Chem. Phys.

74, 6511 (1981).

33. I. Shoshan, N. N. Danon, and U. P. Oppenheim, J. Appl. Phys.. 48, 4495 (1977).
34. M. G. Littman and H. J. Metcalf, Appl. Opt. 17, 2224 (1978).
35. J. A. Lisboa, S. R. Teixeira, S. L. S. Gunha. and R. E. Francke, Opt. Comm. 44, 393 (1983).
36. A. G. Yodh, Y. Bai, J. E. Golub, and T. W. Mossberg, Appl. Opt. 23, 2040 (1984).
37. H. Kogelnick and T. Li, Appl. Opt. 5, 1550 (1966).
38. M. K. Iles, Appl. Opt. 20, 985 (1981).
39. P. McNicholl, Doctoral Thesis, State University of New York At Stony Brook (1986) (unpublished).
40. J. D. Roberts and M. C. Caserio, Basic Principles of Organic Chemistry. (W. A. Benjamin, Inc., New York, 1964).
41. A. P. Dunlop and F. N. Peters, The Furans. (Reinhold Publishing Corporation, New York, 1953).
42. C. D. Cooper, A. D. Williams, J. C. Miller, and R. N. Compton, J. Phys. Chem. 73, 1527 (1980).
43. K. Watanabe and T. Nakayama, J. Chem. Phys. 29, 48 (1958).
44. L. W. Pickett, J. Chem. Phys. 4, 293 (1940).
45. Ibid., 10, 660 (1942).
46. W. C. Price and A. D. Walsh, Proc. Roy. Soc. A179, 201 (1941).
47. M. Rico, M. Barrachina, and J. M. Orza, J. Mol. Spectry. 24, 133 (1967).
48. H. W. Thompson and R. B. Temple, Trans. Faraday Soc. 41, 27 (1945).
49. B. Bak, S. Brodersen, and L. Hansen, Acta Chem. Scand. 9, 749 (1955).
50. R. Rao and M. C. R. Symons, J. Chem. Soc. Faraday Trans. 2, 135 (1983).
51. M. Shiotani, Y. Nagata, M. Tasaki, J. Sohma, and T. Shida, J. Phys. Chem.

87, 1170 (1983).

52. J. H. D. Eland, J. Mass Spectrom. and Ion Phys. 2, 471 (1969).
53. P. J. Derrick, L. Asbrink, O. Edqvist, B. O. Jonsson, and E. Lindholm, Spectrochimica Acta. 27A, 2525 (1971).
54. Ibid.,J. Mass Spectrom. and Ion Phys. 6, 161 (1971).
55. T. Munakata, K. Kuchitsu, and Y. Harada, J. Electron Spectrosc. and Relat. Phenom. 20, 235 (1980).
56. L. F. DiMauro and T. A. Miller, Chem. Phys. Lett. (in press).
57. W. C. Wiley and I. H. McLaren, Rev. Sci. Instrum. 26, 1151 (1955).
58. E. Harting and F. H. Read, Electrostatic Lenses. (Elsevier Scientific Publishing Company, New York, 1976).
59. G. De Alti, P. Decleva, and A Sgamellotti, Gazz. Chim. Ital. 110, 49 (1980).
60. M. G. White (private communication).
61. L. Asbrink, E. Lindholm, and O. Edqvist, Chem. Phys. Lett. 5, 609 (1970).
62. G. B. Guthrie, Jr., D. W. Scott, W. N. Hubbard, C. Katz, J. P. McCullough, M. E. Gross, K. D. Williamson, and G. Waddington, J. Am. Chem. Soc. 74, 4662 (1952). (Extrapolated experimental data using the Clausius-Clapeyron equation.)
63. W. M. Flicker, O. A. Mosher, A. Kuppermann, J. Chem. Phys. 64, 1315 (1976).
64. N. Solony, F. W. Birss, and J. B. Greenshields, Can. J. Chem. 43, 1569 (1965).
65. R. A. Sallavanti and D. D. Fitts, Int. J. Quantum Chem. 3, 33 (1969).
66. J. Doering, J. Chem. Phys. 51, 2866 (1969).
67. D. T. Clark, Tetrahedron. 24, 3285 (1968).
68. R. Engleman, Jr., and D. A. Ramsay, Can. J. Phys. 48, 964 (1970).

69. H. H. Nelson, L. Pasternack, and J. R. McDonald, Chem. Phys. 74, 227 (1983).

70. T. Sears, T. A. Miller, and V. E. Bondybey, J. Chem. Phys. 72, 6070 (1980).

71. M. L. Alexander, M.A. Johnson, N. E. Levinger, and W. C. Lineberger, Phys. Rev. Lett. 57, 976 (1986).

72. U. Buck and H. Meyer, J. Chem. Phys. 84, 4854 (1986).

73. R. W. B. Pearse and A. G. Gaydon, The Interpretation of Molecular Spectra. (Chapman and Hall, London, 1976).

74. W. Smith, Astrophys. J. 156, 791 (1969).

75. J. B. Anderson, R. P. Andres, J. B. Fenn, and G. Maise, Rarefied Gas Dynamics, Fourth Symposium. J. H. de Leeuw, Ed. (Academic Press, New York, 1966) Vol. 2, p. 122.

76. J. M. Green, W. T. Silvast, and O. R. Wood, J. Appl. Phys. 48, 2753 (1977).

77. G. R. Harrison, Ed., MIT Standard Wavelength Tables. (MIT Press, Boston, 1969).

78. E. A. Rohlfing, D. M. Cox, and A. Kaldor, Chem. Phys. Lett. 99, 161 (1983).

79. D. W. Powers, S. G. Hansen, M. E. Geusic, A. C. Pulu, J. B. Hopkins, T. G. Dietz, P. R. R. Langridge-Smith, and R. E. Smalley, J. Phys. Chem. 86, 2556 (1982).

80. G. Koren and J. T. C. Yeh, J. Appl. Phys. 56, 2120 (1984).

81. H. Massey, Atomic and Molecular Collisions. (Taylor and Francis, London, 1979).

82. J. P. Gauyacq and A. Herzenberg, J. Phys. B17, 1155 (1984).

VITA

R. Seth Smith

Address: P. O. Box EC
Baton Rouge, Louisiana 70893

Telephone: (504) 388-6852 -- office
(504) 344-2597 -- home

Teaching Experience

LOUISIANA STATE UNIVERSITY, Baton Rouge, Louisiana, September 1983 - present; LSU Alumni Federation Fellow. Involved in weekly meetings of LSU experimental atomic and molecular physicists. Responsible for presenting seminars on topics of current research interest at such meetings. Gave guest lectures, at the invitation of my research professor, in advanced courses in laser physics.

LOUISIANA STATE UNIVERSITY, Baton Rouge Louisiana, June 1983 - August 1983; teaching assistant; undergraduate physics laboratory. Conducted three hour labs twice weekly. Presented lectures on basic principles of physics. Directed laboratory experiments in conjunction with these.

FRANCIS MARION COLLEGE, Florence, South Carolina, January 1983 - May 1983; laboratory instructor; undergraduate physics laboratory. Responsible for two sections of physics laboratory students. Taught basic concepts in physics. Conducted laboratory experiments.

SELF-EMPLOYED, Florence, South Carolina, September 1982 - December 1982; private tutor; mathematics, English. Instructed local high school students on an individual basis. Covered a variety of areas, including composition, grammar, algebra, and trigonometry.

SELF-EMPLOYED, Florence, South Carolina, September 1979 - May 1980; private tutor; mathematics. Taught local high school students on a one-to-one basis. Topics included mathematics fundamentals through algebra and trigonometry.

WILSON SENIOR HIGH SCHOOL, Florence, South Carolina, January 1977-May 1977; tutor; German. Tutored two students as part of a course requirement. Conducted informal classes on German grammar, spelling, and speech.

Research Experience

LOUISIANA STATE UNIVERSITY, Baton Rouge, Louisiana, May 1985 - present; LSU Alumni Federation Fellow. Designed and tested a more efficient and narrower bandwidth version of the grazing-incidence dye laser. Built two grazing-incidence dye lasers with amplifier chains. Assembled various laboratory equipment, i.e., iodine cell, uranium lamp, photomultiplier tube housings, photodiodes. Performed optical emission studies on a carbon cluster vaporization source in a supersonic free jet. Developed fortran programs for data collection and analysis. Conducted photolysis/photoionization experiments on furan (C_4H_4O) and obtained the first reported laser induced fluorescence spectra on any electronic state of the furan cation ($C_4H_4O^+$). Vibrational assignments were made for both the ground and second excited electronic states of the cation, and a rotational analysis was performed. Additionally, a comparison study between the furan cation and the cyclopentadienyl radical (C_5H_5) was undertaken, since these two molecular species are isoelectronic with one another and their structures are expected to be correlated.

Publications

"Optical Emission Studies on Graphite in a Laser/Vaporization Supersonic Jet Cluster Source", Chemical Physics Letters, 134, 444 (1987). Written in collaboration with E. Daykin, M. Anselment, and L. F. DiMauro.

"Efficiency and Linewidth Improvements in a Grazing-Incidence Dye Laser Using an Intrcavity Lens and Spherical End Mirror", Applied Optics, 26, 855 (1987). Written in collaboration with L. F. DiMauro.

"Laser Induced Fluoresence Study of the $\tilde{B}\ ^2B_2 \rightarrow \tilde{X}\ ^2A_2$ Transition of the Furan Cation in a Supersonic Free Jet Expansion", submitted to The Journal of Chemical Physics, May, 1987. Written in collaboration with M. Anselment, L. F. DiMauro, Joan M. Frye, and T. J. Sears.

Education

Ph.D. in Physics, Louisiana State University, Baton Rouge, Louisiana, to be awarded in the summer of 1987.

M.S. in Physics, Louisiana State University, Baton Rouge, Louisiana, May 1985.

B.A. in Mathematics (major), Physics (minor), Francis Marion College, Florence, South Carolina, May 1983.

College and Graduate Honors

Louisiana State University Alumni Federation Fellow; Francis Marion Scholar; South Carolina Federal Savings and Loan Association Award for Academic Excellence; Lewis E. Beasely Americanism Scholarship; Francis Marion College Scholastic Achievement Award; Dean's List; Who's Who in American Colleges and Universities; American Biographical Institute's International Youth in Achievement; Collegiate Civitans (President in 1980-1981); Omicron Delta Kappa National Leadership Honor Society (Vice-President in 1980-1981, President in 1981-1982); Phi Kappa Phi National Scholastic Honor Society.

Personal

Born December 3, 1960, Baltimore, Maryland. Married, two children. Height: 5'8"; Weight: 145, excellent health.

References

Dr. Louis F. DiMauro, Professor, Department of Astronomy and Physics, Louisiana State University, Baton Rouge, Louisiana, 70803. Telephone: (504) 388-6852.

Dr. Chris H. Greene, Professor, Department of Astronomy and Physics, Louisiana State University, Baton Rouge, Louisiana, 70803. Telephone: (504) 388-6845.

Dr. William C. Moran, Vice-President for Academic Affairs, Francis Marion College, Florence, South Carolina, 29501. Telephone: (803) 661-1281.

Dr Lynn D. Hendrick, Professor, Department of Chemistry and Physics, Francis Marion College, Florence, South Carolina, 29501. Telephone: (803) 661-1381.

Dr. Trevor Sears, Department of Chemistry, Brookhaven National Laboratory Associated Universities, Inc., Upton, Long Island, New York, 11973. Telephone (516) 282-4374.

DOCTORAL EXAMINATION AND DISSERTATION REPORT

Candidate: Robert Sethfield Smith

Major Field: Physics

Title of Dissertation: Laser Spectroscopy of Transient Species in a Supersonic Free Jet Expansion

Approved:

Major Professor and Chairman

Dean of the Graduate School

EXAMINING COMMITTEE:

Date of Examination:

July 17, 1987